INFLUENCE OF BIOMECHANICAL FORCE AND MASS TRANSFER ON THE PROGRESSION OF ATHEROSCLEROSIS IN HUMAN CAROTID ARTERIES

A Thesis
Presented to
The Academic Faculty

by

Sungho Kim

In Partial Fulfillment
of the Requirements for the Degree
Doctor of Philosophy in the
Wallace H.Coulter Department of Biomedical Engineering

Georgia Institute of Technology
August 2011

INFLUENCE OF BIOMECHANICAL FORCE AND MASS TRANSFER ON THE PROGRESSION OF ATHEROSCLEROSIS IN HUMAN CAROTID ARTERIES

Approved by:

Don P.Giddens, Ph.D, Advisor
Wallace H.Coulter Department of
Biomedical Engineering
Georgia Institute of Technology

W.Robert Taylor, Ph.D, M.D
School of Medicine
Department of Cardiology
Emory University

Raymond P. Vito, Ph.D
School of Mechanical Engineering
Georgia Institute of Technology

John N.Oshinski, Ph.D
Wallace H.Coulter Department of
Biomedical Engineering
Georgia Institute of Technology

Ajit Yoganathan, Ph.D
Wallace H.Coulter Department of
Biomedical Engineering
Georgia Institute of Technology

Date Approved: 25 May 2011

To my family...

ACKNOWLEDGEMENTS

When I crossed the Bay Bridge in San Francisco, I asked to myself, "Can I get through the long way of Ph.D research in USA?". After six years, finally I have accomplished this journey with my Ph.D advisor, Dr. Don Giddens. Without his suggesting the opportunity, I would not have had the chance to do research about cardiovascular disease. I would like to show my sincerest gratitude to him for his constructive and critical guidance through the research. Every time I could not find the best direction, he was always with me and showed me the way to overcome the hindrance. He trusts and believes in me and let me have enough time to accomplish each step to the final goal. Most of all, as a advisor, he is my role model to pursue and I am so proud to be his pupil.

I appreciate Dr. John Oshinski the fact that he freely supplied essential MR data for my research, and also I am thankful for the valuable and insightful comments from my committee members including, Dr. Ray Vito, Dr. Ajit Yoganathan, and Dr. Robert Taylor.

I need to say thank you to our members in the Cardiovascular Lab; Jin Suo, Massimiliano, Yi, Yan, and Binjian. Their advice and comments about the research are very helpful to find the way. I especially need to mention help from Yi Gao and Ian Campbell. Discussion with them and their advice about medical image processing and handling in-vivo geometry saved a lot of research time.

Thanks to Joanne Wheatley and Lisa Cox. You got me through Dr. Gidden's hectic schedule and set up many meetings with him. I will never forget your kindness and friendliness.

Without the support of my family, I would never have accomplished my goals.

My wife, Hongwon Jung, is a wonderful person who postponed her dream to be a professor in order to help me finish my Ph.D degree. I give thanks to God that she is my soul mate in my life. My lovely sons, Ryan and Daniel, you are my precious ones, and you make me grown up as a man and father. I also express my deep appreciation to my parents, Maksu Kim and Youngja Park; you were always there to support me and stand with me. You show me the way to follow as a parent. Although I cannot mention everyone who supported and encouraged me, I hope you know I really cherish my relationship all of you.

TABLE OF CONTENTS

LIST OF TABLES

LIST OF FIGURES

SUMMARY

Atherosclerosis is a vascular degenerative disease leading to progressive thickening in the intima of large and medium sized arteries through the formation of plaque that is very rich with cholesterol. The cholesterol is carried by LDL (low density lipoprotein) particles which pass through the endothelium and accumulate in the intima. The passage of LDL is influenced by wall shear stress which activates physiological responses of the endothelium. However, the causal relationship between the physiological responses and their effect on LDL mass transport is not fully understood. To obtain blood flow patterns in human carotid arteries, a fluid structure interaction (FSI) computational approach is employed, based on the in-vivo arterial geometry constructed from black blood magnetic resonance images (BBMRI) and flow rate boundary conditions obtained from phase contrast images (PC). Wall shear stress (WSS) on the luminal surface is computed, and this variable is related to the formation of leaky junctions, which is a major transendothelial pathway for LDL. A model for the fraction of leaky junction at a surface is incorporated into the overall computational scheme for mass transport, along with pore theory.

The theoretical model is applied to images from three human carotid arteries in which the degree of disease ranges from mild to moderate. Maximum mass flux is predicted to be in the downstream region of stenoses where WSS is low, and this result is consistent with the clinical observation of plaque progression downstream of the stenosis. The hypothesis that the majority of LDL enters into the intima through leaky junctions is supported by observation of similar distributions between the pattern of volume flux via leaky junctions and mass flux. These studies suggest that mass flux of LDL can be a predictor to indicate areas with potential for plaque

formation and progression in human carotid artery disease.

CHAPTER I

INTRODUCTION

1.1 Motivation for the Research

Atherosclerosis is a vascular degenerative disease leading to progressive intimal thickening in large and medium sized arteries through formation of plaques that are rich with cholesterol. Plaque rupture causes thrombosis which can precipitously block blood flow carrying oxygen to critical organs. Due to its high incidence atherosclerosis is responsible for the highest rate of morbidity and mortality in Western Society.

Cholesterol, the major culprit in atherosclerosis, is carried by LDL (low density lipoprotein) particles which pass through the endothelium and accumulate within the intima. The passage of LDL is influenced by wall shear stress (WSS) which stimulates physiological responses of endothelial cells via mechanotransduction mechanisms. However, causal relationships between the physiological responses and LDL mass transport are not fully understood.

This research is based on the hypotheses that atherosclerosis progresses at sites of higher LDL accumulation and that the primary mechanism for LDL transport is related to the formation of leaky junctions between endothelial cells. Leaky junctions, in turn, have been shown to be correlated with low WSS, so that LDL transport is connected with the hemodynamic flow field through both convection-driven mass transfer in the lumen and through biological interactions at the wall itself. Computational models are developed from in-vivo images of the left carotid artery of three human subjects with varying degrees of atherosclerosis. Images were obtained from the subjects under an IRB approved protocol at the Emory University Hospital utilizing black blood magnetic resonance images (BBMRI) to obtain in-vivo geometry

and phase contrast (PC-MRI) images for measuring blood velocity. These provide subject-specific boundary conditions for computational fluid dynamics (CFD) modeling, from which WSS is derived.

Experimental research shows that low wall shear stress increases the occurrence of proliferation (mitosis) and death (apoptosis) of endothelial cells (ECs), and these phenomena induce the formation of leaky junctions of gaps sufficient to allow passage of macromolecules such as LDL. Previous studies have considered three pathways for LDL transport: vesicular transcytosis, entry through normal junctions, and entry through leaky junctions. In this study, we focus on the role of leaky junctions, which have been shown to be the dominant pathway. We also examine the role of arterial wall stresses through incorporating a fluid-solid interaction (FSI) modeling approach and compare results to a rigid wall assumption.

1.2 Background

1.2.1 Atherosclerosis

The American Heart Association reports nearly 2400 Americans die of cardiovascular disease (CVD) each day - an average of 1 death every 37 seconds. In 2008, an American will have a coronary event every 26 seconds, and about every minute someone will die from such an event [72]. Atherosclerosis, the primary etiology of CVD, is a vascular degenerative disease usually occurring in large and medium size arteries by which blood is supplied to the critical organs such as brain or heart. In Fig. 1, the occurrence of atherosclerosis in a left anterior descending coronary artery is demonstrated. The reduction of blood supply by atherosclerosis can cause ischemia, and myocardial infarction, or heart attack.

Epidemiological studies over several decades have revealed numerous risk factors for atherosclerosis. Contributors to the development of atherosclerosis can be categorized as factors with an important genetic component (e.g., family history), factors

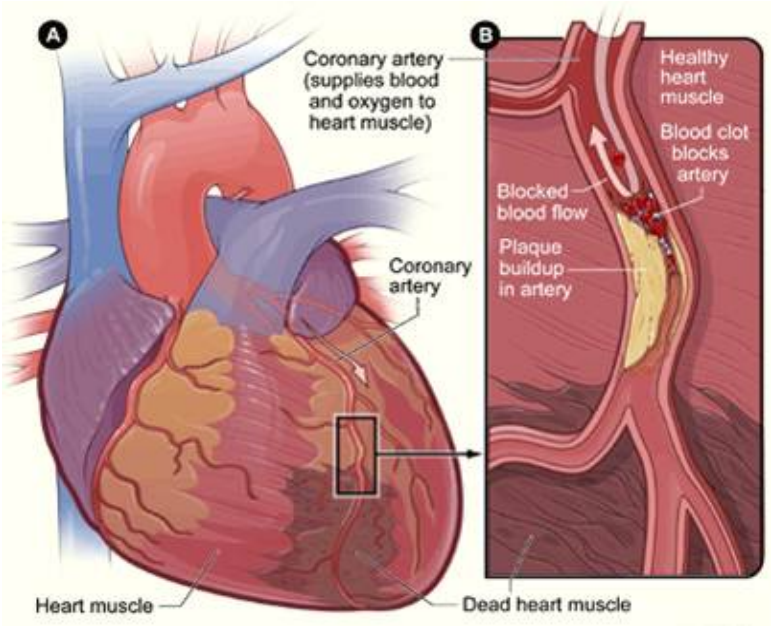

Figure 1: An overview of a heart and coronary artery showing damage (dead heart muscle) caused by a heart attack (A). A cross-section of the coronary artery with plaque buildup and a blood clot (B)

that are largely environmental (e.g., smoking, high-fat diet), biochemical factors (e.g., lipids) and biomechanical factors (e.g., wall shear stress, cyclic mechanical strain, high blood pressure). These causal factors induce endothelial pro-atherogenic dysfunction that leads to inflammation and inflammatory responses. The endothelium, with its intercellular tight junction complexes, has three important functions that are particularly relevant to atherosclerosis: (1) maintenance of a selectively permeable barrier between blood and vessel wall, (2) ability to modify and transport lipoprotein into the wall, and (3) provision of a non-adherent surface for leukocytes. Mechanical forces (e.g., wall shear stress, cyclic mechanical strain) can influence endothelial function in pro and anti-atherogenic ways, depending on their nature.

Mechanical forces are perceived by cellular mechanoreceptors, including G protein coupled receptors (GPCR), integrins, mitogen-activated receptors, etc, at the endothelium surface membrane and mediated through adaptor molecules, a cascade

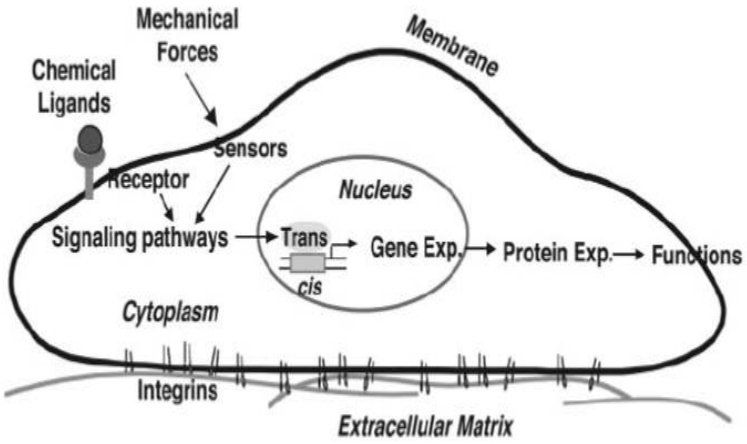

Figure 2: Mechanical forces stimulate endothelial cells through the activation of mechanosensors which activate the signaling pathways [23]

of signaling pathways is triggered, finally activating the expression of genes and proteins. Alteration of genes and proteins in response to mechanical forces regulates the functional behavior of ECs in various ways, including proliferation, growth arrest, inflammation and many others (Fig. 2).

Various mechanisms are related to the development of atherosclerosis and have been summarized in the review by Lusis [55]. The important step of initiation in atherosclerosis is the accumulation of low density lipoprotein (LDL) in the subendothelial matrix. LDL passes through gaps formed by leaky junctions and it can remain in the intima through the interaction between the LDL constituent, apolipoprotein B (ApoB) and proteoglycan in the arterial matrix. In this retention, native LDL is modified by reactive oxygen species (ROS) and transforms to oxidized LDL (ox-LDL). Ox-LDL stimulates endothelial cells to produce a number of pro-inflammatory molecules and inhibits the production of nitric oxide (NO) which controls vasorelaxation. Pro-inflammatory molecules, including adhesion molecules which are expressed on the surface of ECs and chemotactic proteins such as monocyte chemotactic protein-1 (MCP-1), facilitate the attachment of monocytes and movement into the artery. Monocytes transform into macrophages in the subendothelial matrix, and the uptake

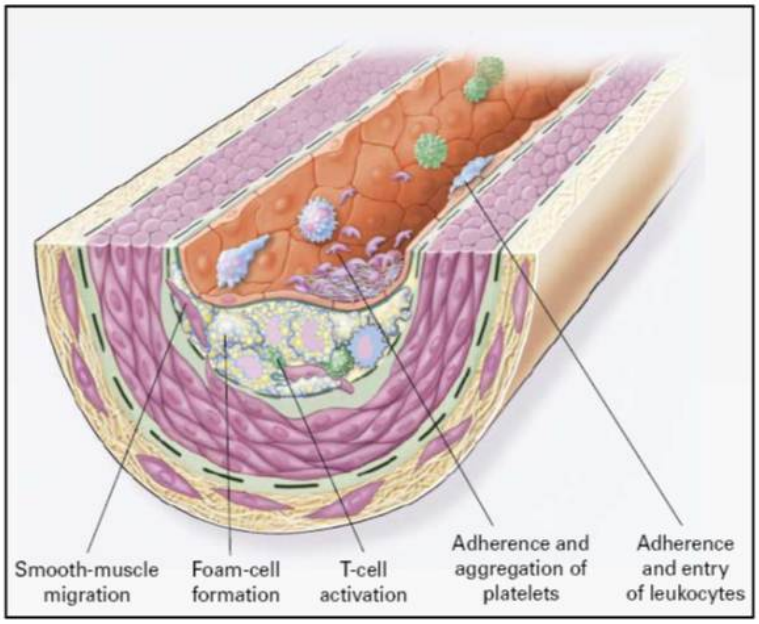

Figure 3: Fatty streaks consists of lipid-laden monocyte and macrophage which is combined with oxidized low density lipoprotein (ox-LDL) and transforms to foam cell [73].

of ox-LDL by macrophages leads these cells to change to foam cells. Foam cells, macrophages, LDL and SMCs which are moved from the media into the intima are sources of the formation of fibrous plaques.

Plaque formation leads to the loss of blood supply and can finally occlude the lumen totally, or a plaque can rupture and cause formation of a thrombus. Although advanced lesions can grow sufficiently large to occlude the blood vessel lumen completely, the most important clinical complication is an acute occlusion due to a thrombus which is associated with rupture or erosion of the lesion. In Fig. 4 A, a specimen from endarterectomy of a carotid artery is presented, showing plaque development in the outer wall of an internal carotid artery. In the cross section of this sample (B and C in Fig. 4), two rupture sites stained red by movat and sirius stains can be observed at this sample tissue.

The importance of genetic and environmental factors has been examined in many family and twin studies. Within a population, the heritability of atherosclerosis has

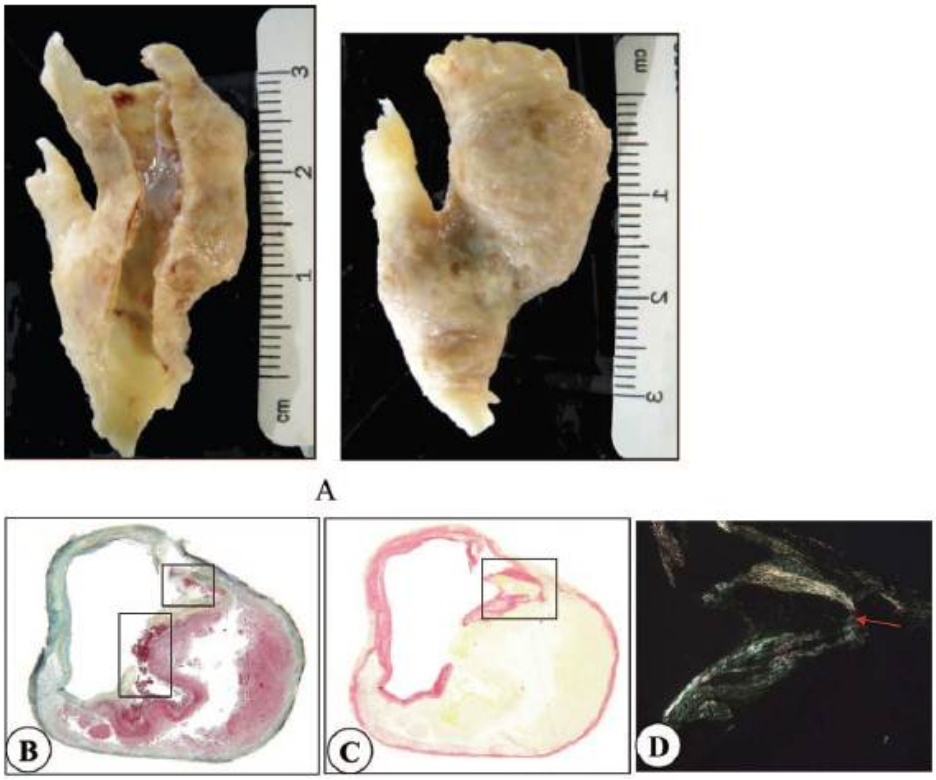

Figure 4: Carotid artery [98]

been high in most study cases, frequently reaching 50%. Population migration studies, on the other hand, demonstrate clearly that environmental factors, including behavior, explain much of the variation of disease incidence between populations [35]. Thus, the common forms of atherosclerosis come from the combination of genetic susceptibility and unhealthy environment. However, genetic and environmental factors provide a systemic type stimulus, while atherosclerosis is a highly localized, heterogeneous disease predominantly occurring in the coronary arteries, carotid bifurcation, and infrarenal abdominal aorta. Although much is known concerning the role of hemodynamics in atherosclerosis, complete understanding of causative links between biomechanical factors and arterial pathogenesis remains incomplete, in part because of the substantial complexity of the highly transient, three-dimensional, biomechanical environment within arteries. Current therapies for cardio vascular disease (CVD) are directed at the revascularization of occluded blood vessels or the reduction of

systematic risk factors related with atherosclerosis (e.g., hypertension, diabetes, dyslipidemia and smoking). These approaches have helped reduce morbidity of CVD, but this trend is leveling off, suggesting that we still lack adequate information about pathogenic mechanisms. The next major innovation in the prevention and treatment of CVD must come from improving our basic understanding of the complex biomechanical environment of the vasculature and the sequential influence upon the pathological responses of the artery.

1.2.2 Wall Shear Stress

Clinical and postmortem anatomical research shows that atherosclerosis lesions tend to be localized in specific sites such as the inner wall of curvature and the outer wall of bifurcation (hip). In these regions the blood flow is disturbed by the occurrence of secondary flow and formation of flow separation and recirculation [46]. This disturbed flow accounts for variation of spatial and temporal wall shear stress, complicated velocity profiles and particle pathlines. Hemodynamics is known to play an important role in the pathogenesis of atherosclerosis, and particular interest has been focused on wall shear stress (WSS), the hemodynamic force acting on the endothelial cell. WSS is the product of the viscosity coefficient of blood and the velocity gradient at the luminal surface.

Endothelial cells in straight tubular arteries, where blood flow is uniform and laminar, are ellipsoid in shape and aligned in the direction of flow. However, cells in regions of arterial branching or curvature, where flow is disturbed, have polygonal shapes and no particular orientation [53]. Adhesion molecules (vascular cell adhesion molecule (VCAM), intercellular adhesion molecule (ICAM), etc.), which help inflammatory cells to be localized on the surface of the endothelium are more overexpressed when endothelial cells are exposed to oscillatory wall shear stress [20]. The expression of VCAM is regulated by interaction with transcription factor, nuclear

factor-kB (NF-kB), whose expression level in endothelial cells changes with disturbed shear stress or laminar shear stress [61]. Bio X et al. [6] applied three different flow profiles to endothelial cells and observed the response of platelet-derived growth factor A (PDGF-A) and monocyte chemoattractant protein-1 (MCP-1) on the different shear stress patterns. In their research different patterns of shear stress, temporal gradient in shear stress or steady shear stress, caused distinct cell responses. Reactive oxygen species (ROS) is produced by NADPH oxidase when endothelial cells are exposed to oscillatory shear stress, but not laminar shear stress, and ROS stimulates an inflammation reaction in atherosclerosis by leading to monocyte adhesion [43].

1.3 Low Density Lipoprotein

Low density lipoprotein (LDL) is an atherogenic material consisting of apoplipoprotein B, which is critical for attachment with LDL receptors on endothelial cells, and the core, which is surrounded by a shell of phospholipid monolayer with unesterified cholesterol. The core contains triacylglycerol and esterified cholesterol. The schematic structure of this particle is illustrated in Fig. 5.

In the plaque formation region, which usually experiences low wall shear stress with complex flow patterns, high LDL accumulation is observed. For this reason, several studies have been conducted to elucidate the role of LDL in atherosclerosis.

Oscillatory low wall shear stress and cyclic mechanical strain cause endothelial cells and smooth muscle cells to produce ROS. In general, increased production of ROS affects several fundamental processes related with atherosclerosis: endothelial dysfunction, vascular SMC growth, LDL oxidization and monocyte migration [9]. Native LDL transforms to oxidized LDL (ox-LDL) with oxidative stress produced by endothelial and smooth muscle cells when they experience biomechanical forces. The various biological effects of ox-LDL are observed through in-vivo animal investigation. Calara F et al. [13] injected human native LDL into rats and observed

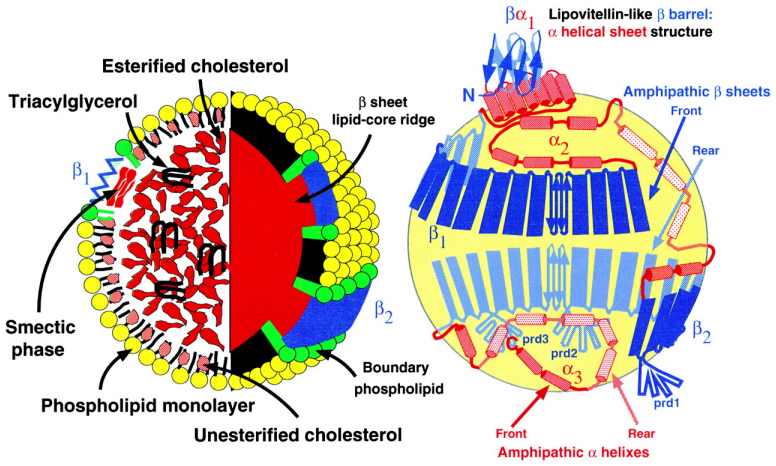

Figure 5: The organization of LDL. The transparent sphere illustrates the organization of apoB [77]

that ox-LDL was detected in arterial endothelium and the blood vessel wall, and this oxidation of LDL occurs locally in the arterial wall, resulting in the activation of NF-kB in the endothelial cells in which the expression of ICAM-1 was also detected. Ox-LDL stimulates the expression of LOX-1, an endothelial receptor for ox-LDL, which stimulates the apoptosis of endothelial cells. This apoptosis is also mediated by activation of NF-kB [54]. The apoptosis of endothelial cells caused by ox-LDL increases the permeability of LDL into the subendothelial matrix by the destruction of endothelial gap junctions. LDL diffuses passively through EC junctions, and its retention in the vessel wall seems to involve interactions between the LDL constituent apolipoprotein B (apoB) and matrix proteoglycans [11]. This retention with proteoglycan is extended by ox-LDL which stimulates the synthesis of proteoglycans with high affinity to LDL [19]. More detailed clinical observations and the role of LDL in initiation and progression of cardio-vascular disease can be found several review papers [22, 62, 76, 82].

1.4 Objectives of the Research

In this research, LDL mass transport is investigated using an FSI-CFD modeling approach that incorporates wall thickness and mass flux through the leaky junctions

which are associated with low wall shear stress. Images from carotid arteries of three human subjects with varying degrees of atherosclerosis are employed for developing the computational models.

In Chapter 2, black blood magnetic resonance images (BBMRI) obtained from three patients are used to create models of the left carotid arteries. Phase contrast (PC) images are taken from common carotid artery (CCA), internal carotid artery (ICA) and external carotid artery (ECA) to acquire volume flow rate, which is utilized as the flow boundary conditions in numerical calculations.

In the lumen, the Navier-Stokes and Convection-Diffusion equations are utilized to compute LDL particle transport in the lumen. At the same time, it is necessary to consider the wall condition to determine LDL mass balance because the filtration flow in the arterial wall caused by the transmural pressure gradient and the permeability of endothelium to LDL have been recognized as key factors in determining LDL distribution. Based on the rigid body assumption, a simplified wall condition, in which the permeability of endothelium and the filtration flow have the same value on the luminal surface, is implemented by a chemical reaction model in Chapter 3.

The results from Chapter 3 show that the permeability and filtration flow are important determinants of LDL concentration and distribution on the luminal surface, however, there is a major limitation in that the influence of mechanical forces on the physiological response of endothelium and its contribution to LDL mass transport is excluded in this model. Therefore, to obtain an improved description of the mechanical environment in the carotid artery, a fluid structure interaction (FSI) method is utilized to extract wall shear stress in Chapter 4. In the in-vivo situation, the carotid artery is already pressurized and expanded by the intraluminal pressure, so that it is not at zero stress state. In contrast, the carotid artery model created by medical imaging processing from an in-vivo configuration has no initial mechanical stress. Thus, an arterial shrinkage procedure or a rescaling of physiological pressure

is essential to prevent the extra dilation due to the mismatch between in-vivo state and zero stress state.

After the appropriate conditions to run the fluid structure interaction model are determined, the flow field is computed and time averaged wall shear stress (TAWSS) is extracted. The TAWSS results are employed in a model for formation of leaky junctions in Chapter 5. Solute and volume flux into the arterial wall due to the formation of leaky junctions and the contribution of each pathway to LDL entry through the endothelium with mass transport parameters, calculated based on the fraction of leaky junction, along with pore theory are demonstrated in this chapter.

In Chapter 6, using poroelasticity, which implements hydro-mechanical coupling between interstitial flow in the porous media and arterial structure, the dynamic response of interstitial flow is illustrated, and it shows the necessity of this approach to obtain LDL concentration in the arterial wall.

CHAPTER II

DEVELOPMENT OF IN VIVO ARTERIAL MODELS AND FLOW BOUNDARY CONDITIONS FROM MAGNETIC RESONANCE IMAGING

2.1 Vascular Diseases and Fluid Dynamics

Among the biomechanical factors implicated in atherosclerosis, wall shear stress (WSS) has been suggested as a hemodynamic indicator related to the initiation and progression of cardiovascular disease (CVD) [57]. As WSS is calculated from the multiplication of blood viscosity and the velocity gradient at the wall, it is necessary to determine this velocity gradient. However, in experimental methods, the accuracy of WSS depends on how close to the wall the velocities can be obtained, how many velocity points can be measured, and how accurately the wall position can be determined. These factors make it challenging to estimate WSS in in-vivo experiments because the blood vessel moves and deforms with the pulsatility of the heart beat. Because of the limitations of experimental methods, computational modeling is an attractive alternative tool which enables us to simulate and quantify biomechanical factors in otherwise inaccessible regions.

The resolution of medical images (e.g., magnetic resonance angiography [MRA], computational tomography [CT] and intravascular ultrasound [IVUS]) can provide critical information for developing Computational Fluid Dynamics (CFD) models. Through sophisticated image processing we can obtain realistic geometries which are used as domains for calculation, and subject specific flow rates (typically measured with phase contrast magnetic resonance imaging (PCMRI) or IVUS) can be used as boundary conditions for transient flow simulation. After establishing a CFD model

and computing the flow field, the imaging data internal to the domain can be employed to verify the computational results. For example, Botner et al. [12] compared blood flow velocity measurements by MRI in an in vitro model to the results of numerical simulations performed for a corresponding computational vessel model and found peak axial velocities vary less than 10% between PCMRI measurements and CFD calculations. Velocity from PCMRI measurement was also used to calculate the wall shear stress (WSS) vectors in the carotid artery [47]. When WSS was compared to the CFD results at sites of well behaved flow, MRI measurements and the WSS from CFD were in good general agreement. Ku JP et al. [50] set up a phantom model which represented an idealized stenotic vessel with a bypass graft. PCMRI data were acquired at five different locations, and the inlet plane measurements were used to prescribe boundary conditions for the CFD calculations. They found good agreement was obtained from comparisons between the velocity profiles in both magnitude and shape. Magnetic resonance phase velocity mapping (PVM), which has been widely used to measure blood flow, was verified to be useful in providing entire cross-sectional blood velocity profiles through the comparison of in-vitro aortic model measurements and in-vivo velocity encoding value (VENC) measurements [21]. However, still in the regions which shows complex flow patterns or in in-vivo PCMRI, velocity profile and sequential WSS is not clear showing enough as shown in CFD results.

Arterial geometry strongly influences local blood flow patterns. Berthier B et al. [10] compared flow patterns calculated in a coronary vessel which was reconstructed by three different methods. In the simplest model, the coronary artery was modeled by a tube with constant diameter, and as a consequence the flow resembled Poiseuille flow in a straight tube, whereas, in a complex model in which the cross section corresponded to a more realistic geometry, velocity and shear rate exhibited sudden local variations and an area experiencing very low wall shear stress was observed. As the

quality and resolution of diagnostic medical imaging has progressed with ongoing improvements in computer aided image analysis, it has been more popular to construct patient specific models of arteries for the CFD analysis, often called, imaged-based CFD [84]. Most of imaged-based CFD simulation has focused on elucidating the relationship between hemodynamic factors and the presence of vascular plaque. Glor FP. et al. [30] investigated reproducibility of the predicted flow field through comparison between hemodynamic factors (wall shear stress gradients [WSSG], oscillating shear index [OSI], and WSS angle deviation [WWSAD]) based on MRI for carotid arteries of eight healthy volunteers. In their research low-time-averaged WSS was dominant around the carotid sinus and high-time-averaged WSS was observed at the divider of bifurcation. The correspondence between low and oscillating WSS and wall thickening at the carotid sinus was demonstrated by Steinman DA et al. [85]. They utilized black blood MRI (BBMRI) to separate the lumen and vessel wall, and they measured velocity at inlet and outlet areas using PCMRI. Imaged based CFD provided the distribution of WSS, and they compared this to the wall thickness to verify the role of low WSS. The research by Suo et al. [88] also supports the concept that low wall shear stress was dominant at the outer wall of bifurcation and epicardial side of heart which was recognized to be atherogenic prone sites in a left coronary artery from CT.

2.2 Construction of patient specific models from MR Images

2.2.1 T2W black blood MR Image processing

Vascular geometry strongly influences the local features of hemodynamics and hence mechanical reactions of the blood vessel by the blood flow. Thus, it is critical to be able to develop a realistic geometry which can be used as the domain for calculation. Different medical imaging methods are used depending on the research purpose because each module has its own advantages compared to other modules. For example, CT provides clearer images compared to MRI due to high resolution, but it

cannot supply flow boundary information needed for CFD. Additionally, the patient is exposed to radiation. It is critical that medical image data are able to supply the lumen and arterial wall with inlet and outlet boundary condition in order to simulate FSI modeling. For these reasons magnetic resonance image modules are chosen as MRA (magnetic resonance angiography) to obtain blood lumen, black blood MRI (magnetic resonance image) to define the blood vessel wall geometry and PC (phase contrast) MRI to gain the velocity profile as boundary conditions for CFD.

In this research, MRI data sets supplied from the EFFERVESCENT grant of Arshed Quyyumi, MD and John Oshinski, Ph.D. are used to construct geometry and supply boundary condition data. These medical images were taken from carotid arteries of 25 patients who were 50-75 years of age (mean=58) and were asymptomatic for carotid artery disease. These patients were in a control group who had not taken stain or valsaltran therapy to reduce the progress of atherosclerosis for 24 months and had undergone successful, artifact-free MR imaging at two time points. All images were acquired on 1.5-3.0 Tesla MRI scanner (Achieva 3T, Philips Medical Systems, Best, The Netherlands) using a 4-channel, bilateral carotid coil. Detailed sequence parameters are summarized in Table 1. The study was approved by the Emory University IRB.

It is necessary to segment the 2D MRI images to get the geometry for the lumen and the blood vessel wall, and we employed T2W TSE black blood MRI. From the bifurcation apex (referred to as the origin) one set of $10 \times 2mm$ contiguous, interleaved, axial slices was taken in the inferior direction covering the common carotid artery (CCA) and the other set was acquired in the superior direction covering the internal carotid artery (ICA) and external carotid artery (ECA). Fig. 6 shows the left CCA in subject 2. Although three subjects in our research had relatively good quality of black blood MRI (BBMRI), it was found to be difficult to segment the arterial wall automatically by the program. Thus, except for some parts of the CCA, most of

Table 1: Pulse sequence parameters for the 3D TOF MRA and PCMR data

	3D TOF	PCMR	T2W TSE
Sequence	3D GRE	2D cine GRE	T2 TSE
Flip Angle	17	10	90
TR	26msec	8.3msec	1700msec
TE	7.1msec	4.9msec	50msec
FOV	120 × 160mm	112 × 160mm	120 × 160mm
Matrix	384 × 512	128 × 256	384 × 512
Pixel Size	0.3 × 0.3mm	0.6 × 0.6mm	0.3 × 0.3mm
Phases	1	16	1
Slices number	60	2	20
Slice thickness	1mm	3mm	2mm
Fat-Sat	no	no	no
NSA(NEX)	2	2	2
VENC	N/A	100cm/sec	N/A
Pre-pulse	N/A	N/A	180-180 NS (Black Blood)

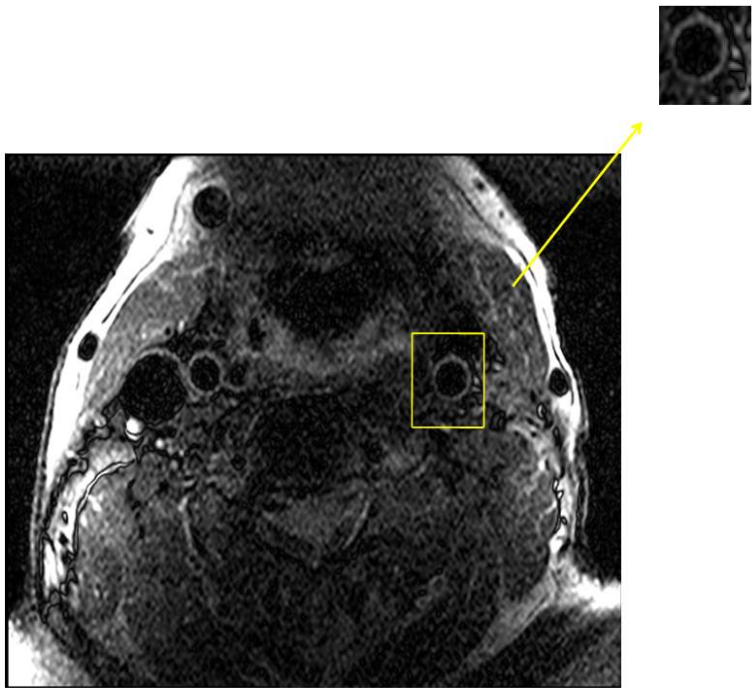

Figure 6: T2W TSE black blood MR in the CCA of subject 2

carotid artery was delineated manually because leakage occurred at the edges when the automatic segmentation process was attempted. From the start of the bifurcation the quality of BBMRI deteriorated due to the complex flow patterns and signal noise. If there is stenosis development at the carotid bulb, the inner wall geometry cannot be separated from the blood flow without employing other image modules. Around and after the bifurcation, especially in the ECA, MRA images (3D TOF) were used to help delineate the lumen and the arterial wall by comparing with T2W TSE black blood MRI. In general, the MRA image is much better to segment the lumen because these images are evident and the gap between each 2D slice is smaller than BBMRI. Thus, when it was not obvious how to separate the inner wall with BBMRI, the outline from MRA was chosen at that position. Segment (Cardiac MR group, at Lund University) in which the edge is detected by a fast algorithm for tracking moving interfaces in a level set-like manner [63] is used to segment images. The points of contour of the lumen and outerwall were imported to the CAD program, Geomagic (Geomagic Inc., NC,USA), in which the NURBS (Non uniform rational B-Spline) algorithm is used to make the 3D volume surface based on 2D outline stacks. To eliminate distortion of the mesh used as the calculation points in the numerical program, it is essential to smooth the contours and the surfaces in a reasonable range in which the geometrical distortion does not influence the numerical results. This program has the ability to control the number of surfaces covering the geometry, and this facilitates creating a good mesh in the geometry. The inner wall and outer wall of the blood vessel in each subject and 3D transparent models are seen in Figs. 7, 8, 9.

Carotid arteries from the three subjects depicted show the general features found in the human carotid artery. In all subjects, geometrical non-planarity is observed between mother and daughter branching arteries. The tortuous curvature of the ICA varies among individuals but, in general, is more severe than the curvature of the ECA. There is a carotid bulb in the ICA and stenosis is observed around the

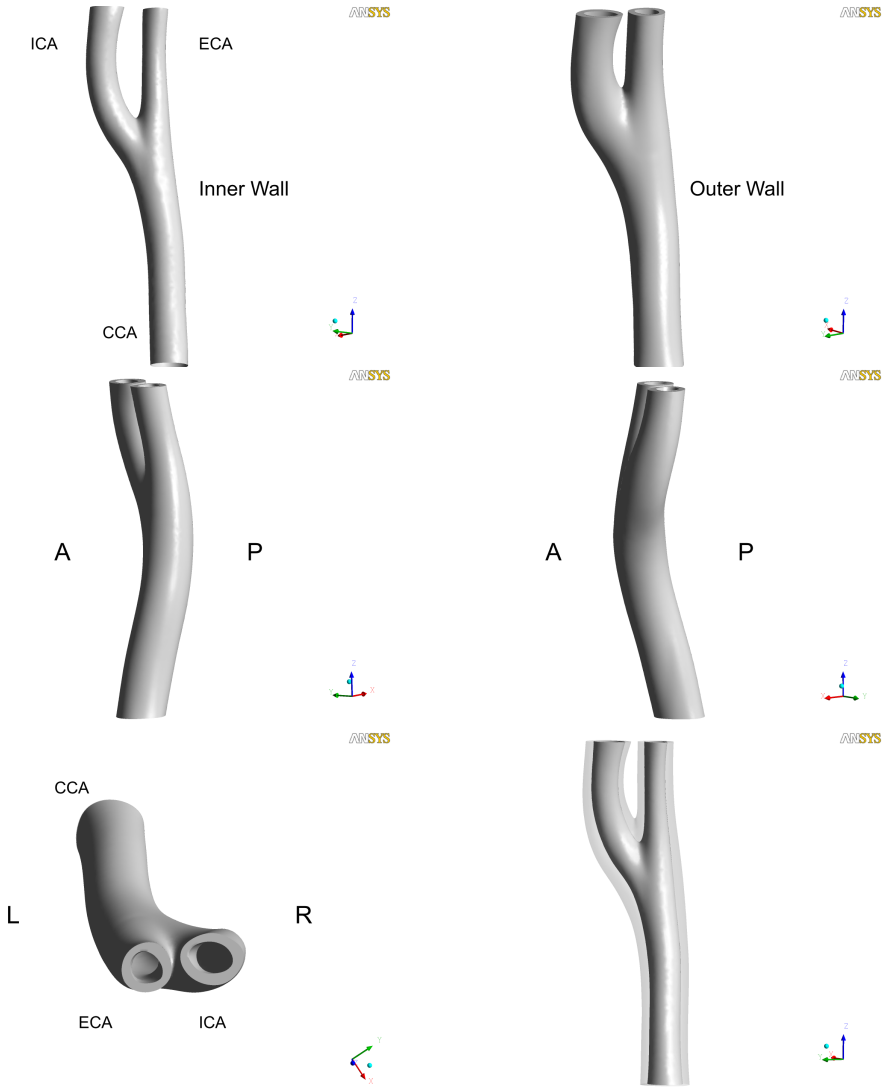

Figure 7: Human carotid artery of subject 1 (A:Anterior, P:Posterior, R:Right, L:Left)

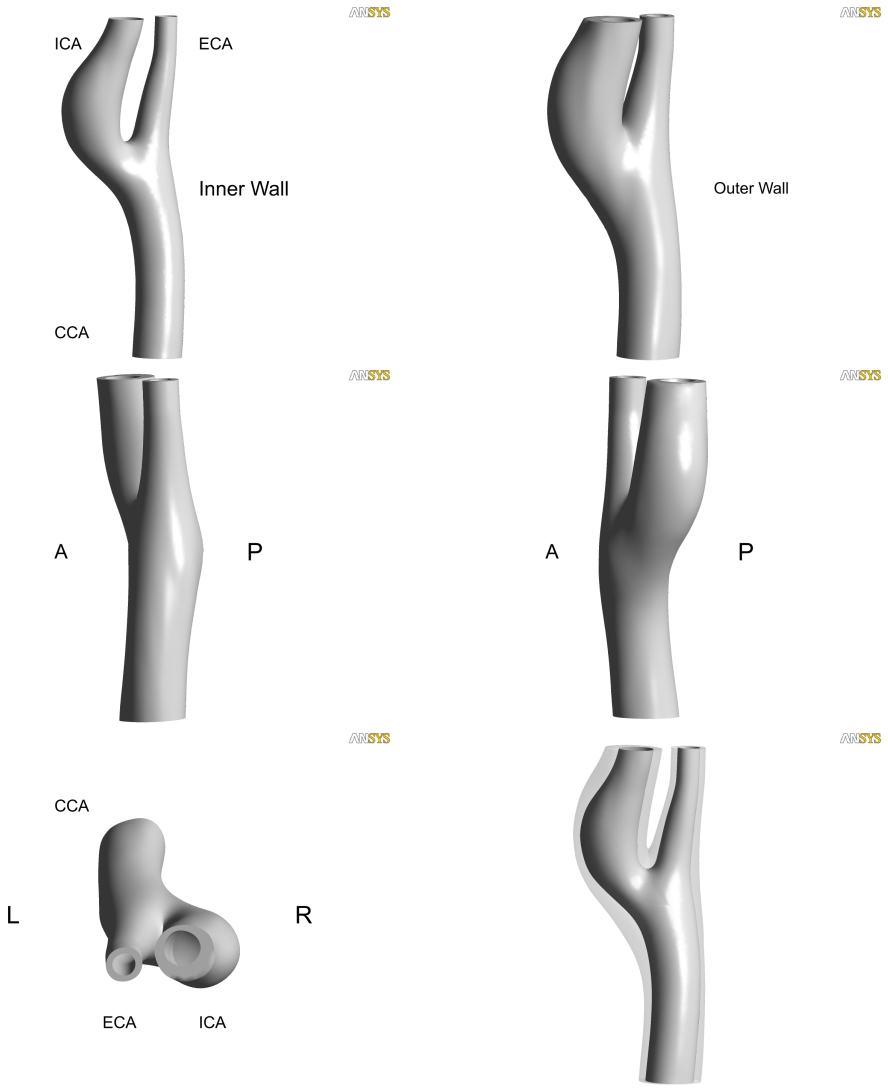

Figure 8: Human carotid artery of subject 2 (A:Anterior, P:Posterior, R:Right, L:Left)

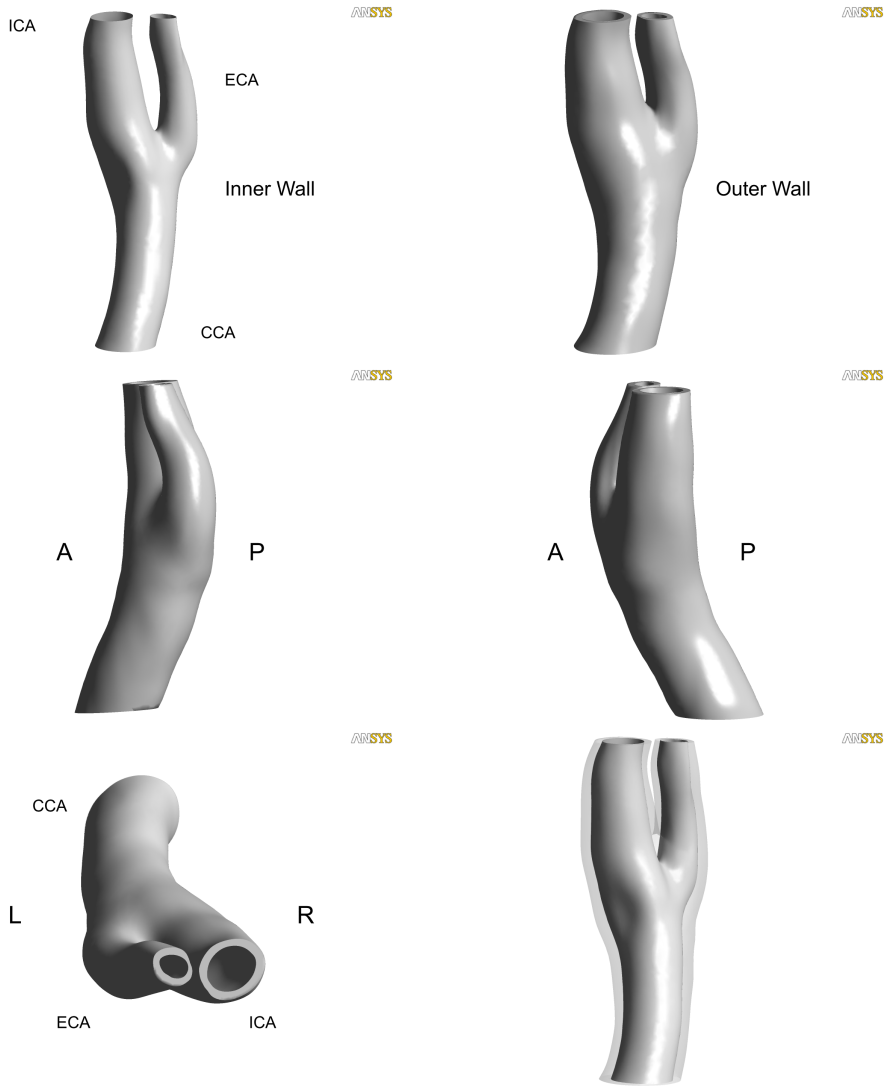

Figure 9: Human carotid artery of subject 3 (A:Anterior, P:Posterior, R:Right, L:Left)

beginning of the bifurcation at the outer wall. The stenosis becomes more severe from subject 1 to 3.

2.2.2 Velocity profile from PC (phase contrast) MR data

PC MR data consists of magnitude (anatomic) and phase (velocity) MR images. Magnitude MR images are used to isolate the region of interest (ROI) and the segmented ROI is used as the mask to isolate the same region of phase images to get velocity information. The PC MRI was measured from slices at $10mm$ below and

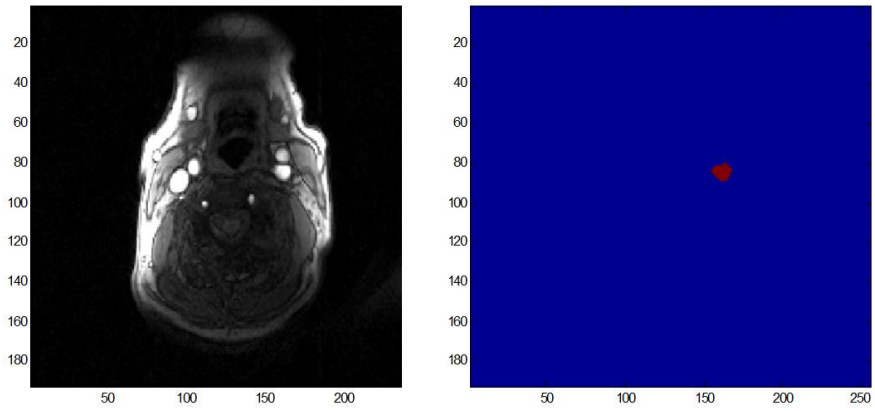

Figure 10: Phase contrast magnitude image at the CCA and the segmented image of left CCA

$10mm$ above the bifurcation apex. PC MRI at a slice $10mm$ inferior from the apex was used to obtain the CCA flow rate and at $10mm$ above to get the ICA/ECA flow rate. However, the site at $10mm$ below the apex overlaps with the beginning of bifurcation in subject 2, in which there is a stenosis, thus, the shape of PC MR shows deviation from the circle (Fig. 11). In each case, a total of 30 time points were measured in a cardiac cycle. To isolate the inlet and outlet area of magnitude PCMR images, a Matlab in-house code which was developed by Fornwalt et al. [32]. using a region growing algorithm was utilized to implement the segmentation. Phase MR data must be rescaled to supply quantitative velocity information. To do this, an encoding velocity, called "$Venc$" in the MR information section, is applied to change the data range, and after this process original phase MR intensities which range from 0 to 4095 are rescaled to from $-Venc$ to $+Venc$.

The detailed velocity pattern at the cross section can be seen in Figs. 11 $\sim$ 15. In each figure, each time point consists of two sets. One is the surface plot of velocity and the other is the contour plot perpendicular to the axial direction. In the acceleration phase the flow pattern becomes more asymmetric as the flow rate rises up to the peak value. At the same time, the extent of the reverse flow pattern

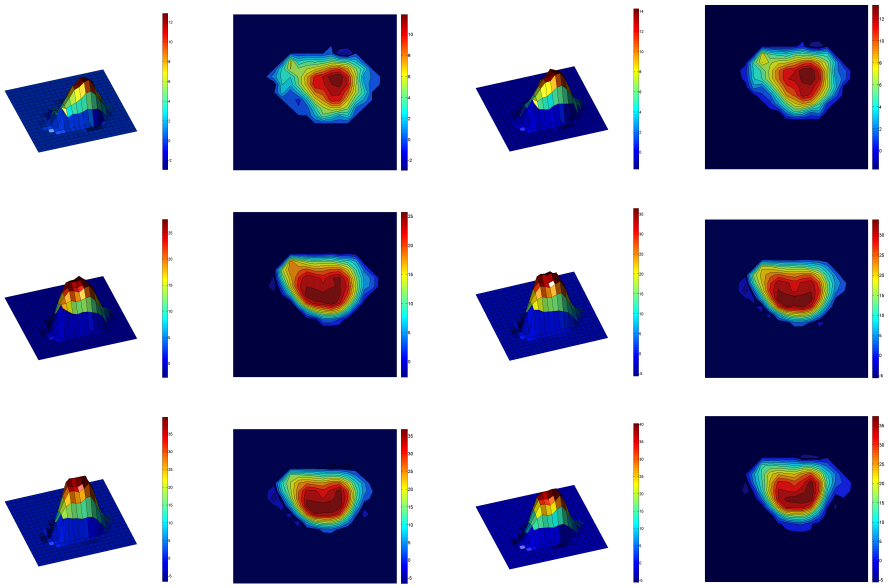

Figure 11: PC MRI at the acceleration phase in the systole of subject 2

is reduced and most of region experiences increases in the magnitude of flow. The maximum velocity at the beginning of acceleration phase is around $12cm/s$, but at the peak value the maximum velocity reached $40cm/s$. After the acceleration phase, the flow pattern becomes less asymmetric with decrease of maximum velocity at each time point. Although less evident, there still exists an asymmetric velocity pattern. The maximum velocity decreased rapidly from $35cm/s$ to $20cm/s$ until a slight rise of flow rate in the middle of diastole. (Refer to Fig. 18 where a slight increase of flow rate in the middle of diastole is observed during $0.4s \sim 0.5s$). In this phase, the velocity pattern showed the most developed reverse flow pattern at the inner wall of bifurcation. In the deceleration phase, the flow lost the inertia force and the velocity decreased. However, the sudden increase of flow rate at this phase gave an inertia force again and caused the most complex flow patterns that ocurred in the cardiac cycle. After this phase ($0.5s \sim 0.6s$ in Fig. 18), the flow rate decreased and the maximum velocity fell off from $18cm/s$ to $14cm/s$. In the end of diastole the range of the velocity is narrow with the maximum velocity of $12cm/s$, corresponding to the minimum flow rate at this phase.

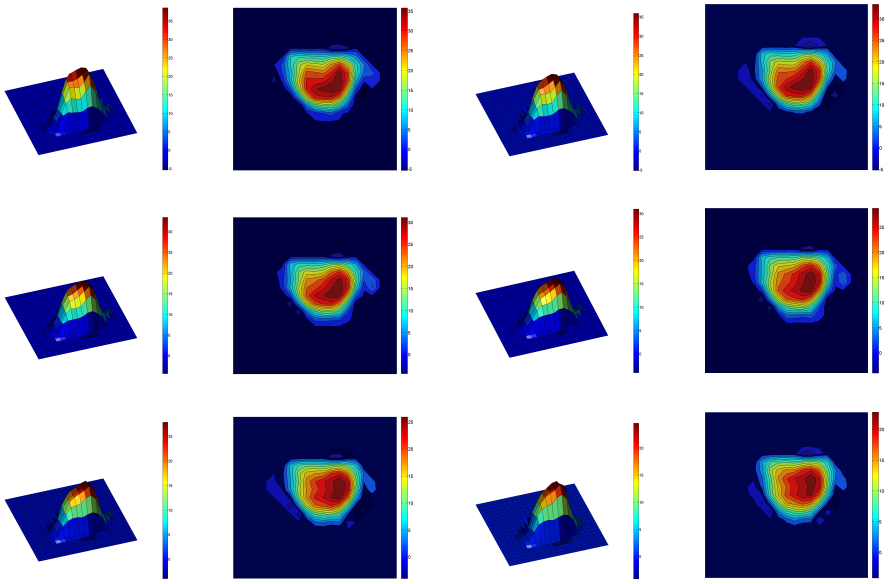

Figure 12: PC MRI at the deacceleration phase of subject 2

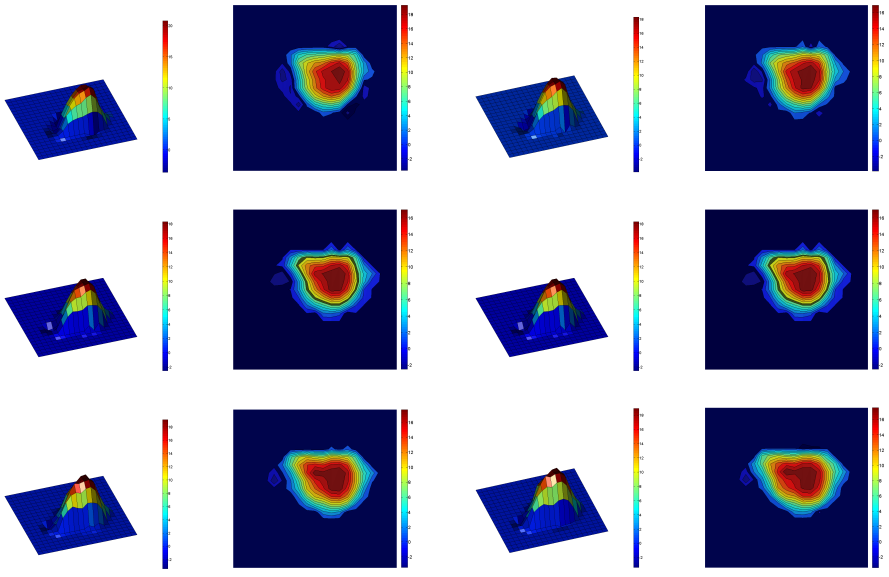

Figure 13: PC MRI at acceleration phase in the middle of diastole of subject 2

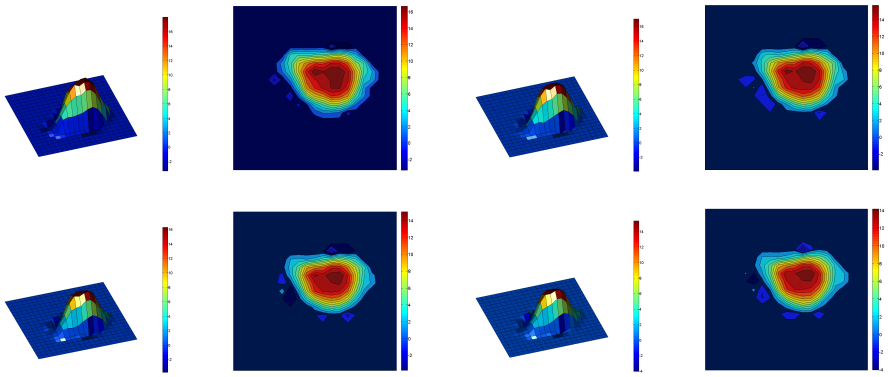

Figure 14: PC MRI at deceleration phase in the middle of diastole of subject 2

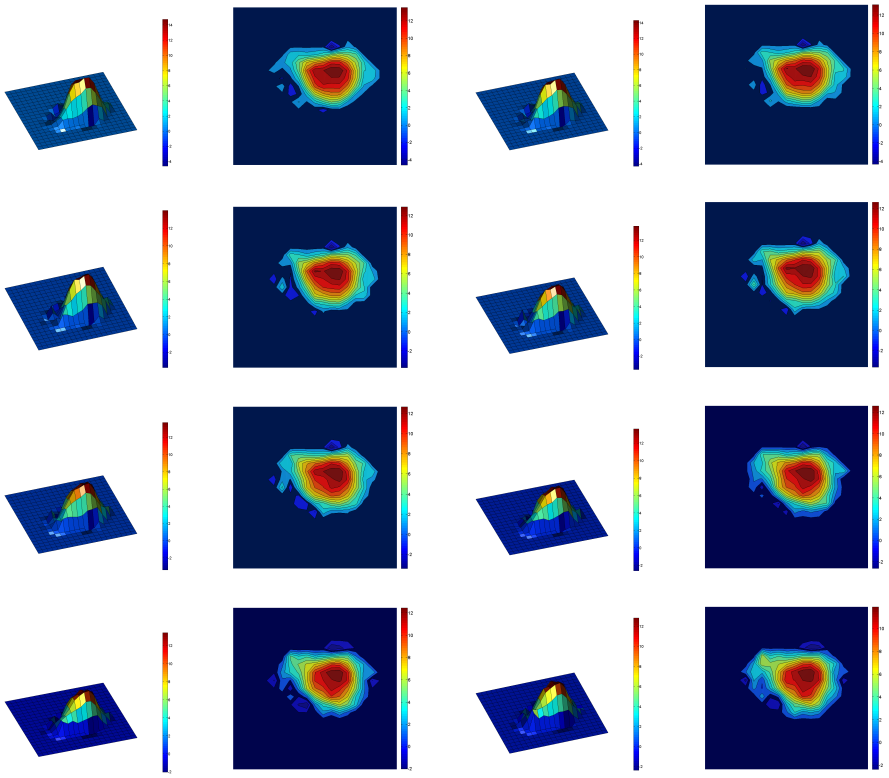

Figure 15: PC MRI in the end of diastole of subject 2

2.2.3 Converting velocity profiles to volume flow rate waveforms

PCMR images were acquired for one cardiac period at thirty time points for the CCA and ICA/ECA in each patient. However, thirty time points are not enough to catch transient flow patterns in hemodynamics, and sometimes it is necessary to change the time step size to stabilize the simulation process. To control the time step size in simulations and give the extra time intervals needed it is necessary to extract the flow waveforms from curve fitting methods based on the image-processed PC-MR data. The average velocity over the cross section was obtained and the flow rate was calculated by the multiplication of mean velocity and the cross sectional area of the ROI at each time point.

The trigonometric Fourier Series, which consists of sine and cosine functions that are used to describe a periodic signal, was employed with 5 to 7 terms (harmonics), depending on the flow waveforms. Figs. 16, 18, 19 illustrate that the trigonometric Fourier Series method successfully captures the flow rate points in one cardiac cycle, and these flow waveforms can be extended for extra time periods. This periodical pattern is important because at the beginning of the calculation the numerical results do not reach the true periodic values in the transient flow and solid simulation during only one cardiac cycle. Thus, it is critical to run the simulation for additional cycles to remove initial effects. In our research, every simulation runs for three cardiac cycles, and the results of the last period are used.

The flow curves are different from each person, but the general patterns are very similar during the cycle. In the beginning of systole the flow rate increases sharply to the peak value, and in the rest of the period the flow rate drops off slowly except for a slight increase of flow rate in this phase [18, 60, 106, 108]. In general, the flow rate of the CCA is much larger than each of the daughter arteries, the ICA and ECA; and in these two daughter arteries, the ECA is less than the ICA flow rate. The flow division ratio between the ICA and the ECA in human carotid artery has been

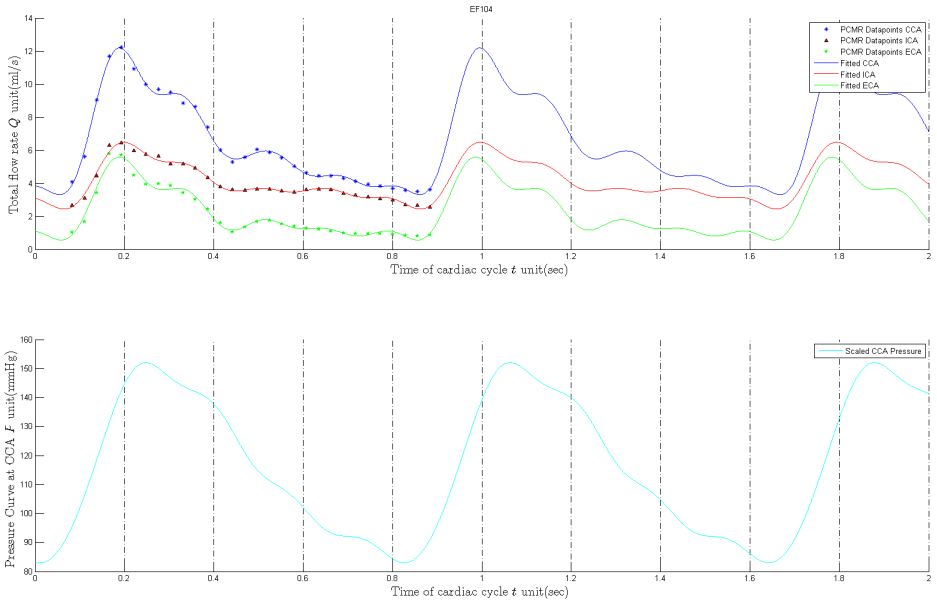

Figure 16: Flow waveforms at CCA, ICA and ECA of subject 1 and pressure curve

reported as 70 : 30 in the study of Zarins et al. [104]. In Fig. 17, the flow division between the ICA/ECA of each subject is presented in a cardiac cycle. Flow division ratio in a cardiac cycle is very different between subjects, however, mean value of flow division ratio in a cardiac period is very similar between subjects with the following ratio: mean value of the ICA flow division is 67.9% and 32.1% in the ECA in subject 1; 60.7% in the ICA and 39.3% in the ECA in subject 2; 65.5% in the ICA and 34.5% in the ECA in subject 3. However, depending on the geometrical features, i.e., the degree of stenosis in the carotid artery, ICA flow can sometimes be less than ECA flow in a cardiac cycle. This pattern is found in subject 2 in our model (Fig. 18) and Tada et al. [89].

In Fig. 19 (subject 3), the flow rate for the CCA is very similar to the ICA. This patient had a significant stenosis that extended into the beginning of the bifurcation and there is a possibility that this large lesion hinders the detection of flow rate of the CCA inasmuch as the flow rate of the CCA was measured at the $10mm$ down from the

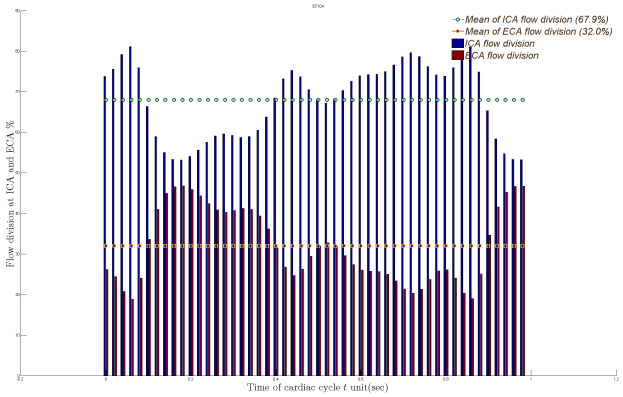

(a) Subject 1

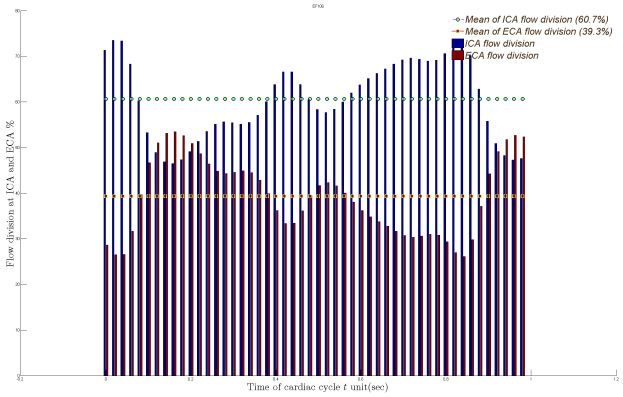

(b) Subject 2

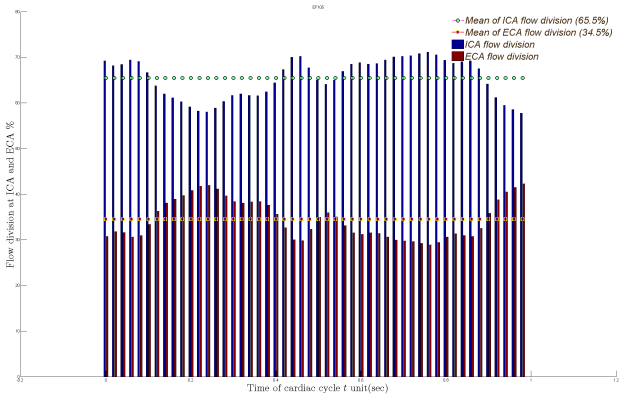

(c) Subject 3

Figure 17: ICA and ECA flow division ratio in each subject

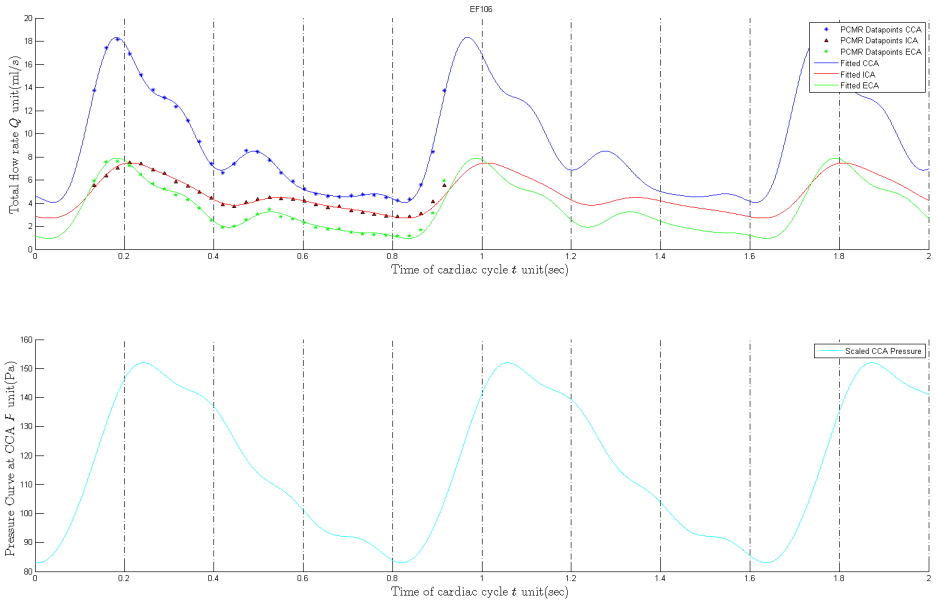

Figure 18: Flow waveforms at CCA, ICA and ECA of subject 2 and pressure curve

apex of bifurcation at each subject. Complex flow patterns at severe stenosis make it difficult to detect the flow pattern accurately at this point. Thus, in the blood flow simulation the flow rates of the ECA and the ICA are imposed at the outlet boundary condition and the inlet at the CCA is treated as traction free.

In the FSI modeling studies, the flow rates of ICA/ECA are applied at the same site as for the flow simulation, and the pressure waveform is applied at the CCA instead of traction free boundary condition in CFD. Along with the flow waveforms, the pressure curve is shown at the bottom of each figure. It is necessary to apply the pressure at the CCA in the FSI simulation due to giving the appropriate pressure at the interface surface to cause a physiologic vessel wall deformation. However, none of our subjects had an intra-arterial pressure measurement, so that the pressure curve for the CCA was referenced from the research done by Zhao et al. [108] who estimated the pressure in the common carotid artery using applanation tonometry. Each person has a different heart beat, and the pressure curve should be rescaled to match the

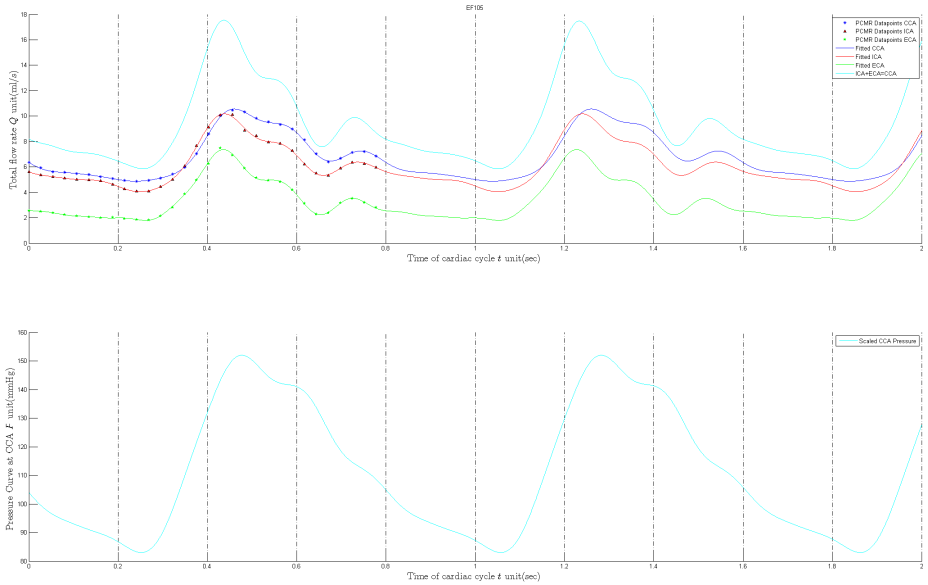

Figure 19: Flow waveforms at CCA, ICA and ECA of subject 3 and pressure curve

flow waveform period of the cardiac cycle of each patient.

The phase shift between CCA pressure and the ICA/ECA flow rates is not easy to ascertain due to the lack of information about pressure at CCA in our subjects. The distance between the sites of measurement of the CCA and ICA/ECA is very short at around $2cm$ in each subject, and thus it is difficult to find any phase shift between flow waveforms. It is also hard to observe phase differences in flow and pressure pulses because the speed of the elastic tube pulse is several meters per second in the normal artery while the axial dimension is around 5 and $6cm$. The same pattern also has been observed in other studies of carotid artery simulations [18, 60, 106, 108].

In the FSI study based on an idealized carotid artery geometry, Perktold et al. [67] applied the flow rate at CCA/ECA and the pressure at ICA. In their research the interesting thing is that the beginning of sharp rise of the pressure at ICA is earlier than the flow rate at CCA/ECA. It would be anticipated that the pressure at ICA began to rise up later. In the research by Huang et al. [41] there is no phase shift between the inlet pressure in the CCA and the outlet pressure in the ICA/ECA. The

time of peak value of each pressure is the same. Zhao et al. [106] applied the flow waveforms and the pressure in the CCA/ICA and ECA, respectively, based on the measurement of five healthy persons. The flow waveforms at CCA/ICA also showed no observable phase shift. The ECA pressure curve began the sharp rise earlier than the sharp increase of the flow rates. This earlier pressure rise is the same pattern as the pressure at the ICA described by Perktold et.al. However, the flow waveform reached the peak value faster than the pressure curve. In general, the CCA wall distension is in the same phase with the CCA pressure curve, and thus the CCA wall distension is used to set up the pressure curve of CCA. Tada et al. [89] measured the flow rate in the CCA, ICA/ECA, and the CCA wall distension and applied the above approach to get the pressure curve of CCA. In their research there is no phase shift between the pressure curve and the flow rate of CCA/ICA. But the time of the peak value of the flow rate at the ECA is slightly delayed. Based on the referenced literature it can be concluded that the pressure at CCA starts its rapid rise earlier than the flow rate, but the flow rate at ICA/ECA reaches the peak value faster than the pressure at CCA.

The pressure waveform of CCA is relatively not changed from person to person. Ramnarine et al. [70] measured the pressure and the dilation of 224 normal and diseased carotid arteries from 126 patients. The CCA wall distension is similar with or without the light or severe stenosis at the bifurcation. For this reason in our research the pressure curve of CCA is chosen as inlet boundary condition and the flow rates of ICA/ECA which come from image processing are applied as the outlet boundary conditions. The pressure curve from Zhao et al. [108] is rescaled to the pressure range ($83mmHg \sim 152mmHg$), which comes from the measurement of Ramnarine et al. [70]. In Fig. 16, 18, 19, the CCA pressure curve and the flow waveform at ICA/ECA show that they follow the above trend and have a periodicity over several cardiac cycles.

CHAPTER III

FLOW FIELDS AND LDL CONCENTRATION BASED ON RIGID BODY ASSUMPTION

3.1 Mass Transfer of Low Density Lipoprotein in Arteries

Species which are transported from the lumen into the arterial wall encounter various forms of resistance based on the nature of species. Oxygen, ATP and other gases are consumed on the entire surface of the endothelium by enzyme catalyzed chemical reaction. In contrast, many hydrophilic solutes which cannot pass through the cell membrane are transported through the cell junctions which size is typically between 10 - 20nm so that these cell junctions act as the major barrier to the migration of species larger than this gap. For example, soluble proteins in the blood such as albumin and LDL are not able to get into the arterial wall through tight junctions and adherens junctions due to their large size in the range 30 - 1000nm [91].

There are two mechanisms of transport pathways to carry the LDL particle through the endothelium. LDL is taken up by receptors on endothelial cells and transported via vesicular bodies across the cells. This process is called transcytosis [80]. LDL also can pass through the endothelium without regulation by the receptor. It is called paracellular pathways. The inter-endothelial cell junction can be broken, and a so-called "leaky" junction is formed by apoptosis and mitosis of these cells [14, 15, 99]. An interesting fact about LDL transport through transcytosis is that LDL transport into the intima is independent of LDL-receptors on the endothelial cells. The LDL permeability of the arterial wall in rabbits was not affected by methylation of the apolipoprotein B (apoB) in LDL (Fig. 5), which abolishes its

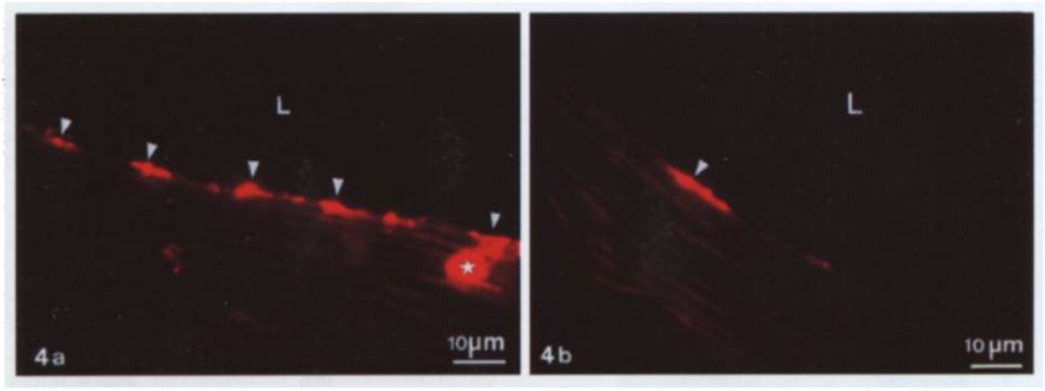

Figure 20: Fluorescence micrographs of aortic arch and the unbranched regions of the thoracic aorta from a rat. (a) More LDL (arrow head) deposition is detected at the intima of the branched regions of aortic arch than unbranched regions (b) [45]. L is the lumen.

recognition by the LDL receptor [62]. As a result, in most of LDL transport simulation, the transcytosis pathway drops out from consideration, and its effect is included in the overall permeability of LDL. The limited contribution of transcytosis to LDL mass transfer through the endothelium invites consideration of the role of leaky junctions in LDL mass transfer. The contribution of each pathway to LDL mass transport was examined by Cancel et al. [14, 15] based on in vitro experiments using bovine aortic endothelial cells (BAEC). BAEC monolayers were exposed to transmural pressure leading to a filtration flow passing through the endothelium. It was found that the entry of 90% of LDL particles were carried out with convective filtration flow via leaky junctions, but only 10% of LDL by the transcytosis pathway. The role of broken inter-endothelial cell junctions has been observed by many investigators. The experiment done by Kao et al. [45] demonstrated that open junctions in endothelial cells at the branched region had a gap widths of $30 - 450nm$, but no open junctions were detected in un-branched region of the thoracic aorta. Moreover, the LDL-gold conjugate, which enables visualization of the LDL distribution in-vivo, was observed around open gap junctions between endothelial cells, but no gold LDL conjugate was found in the normal intercellular channels ($25nm$ and less)(Fig. 20). In in-vivo ex-

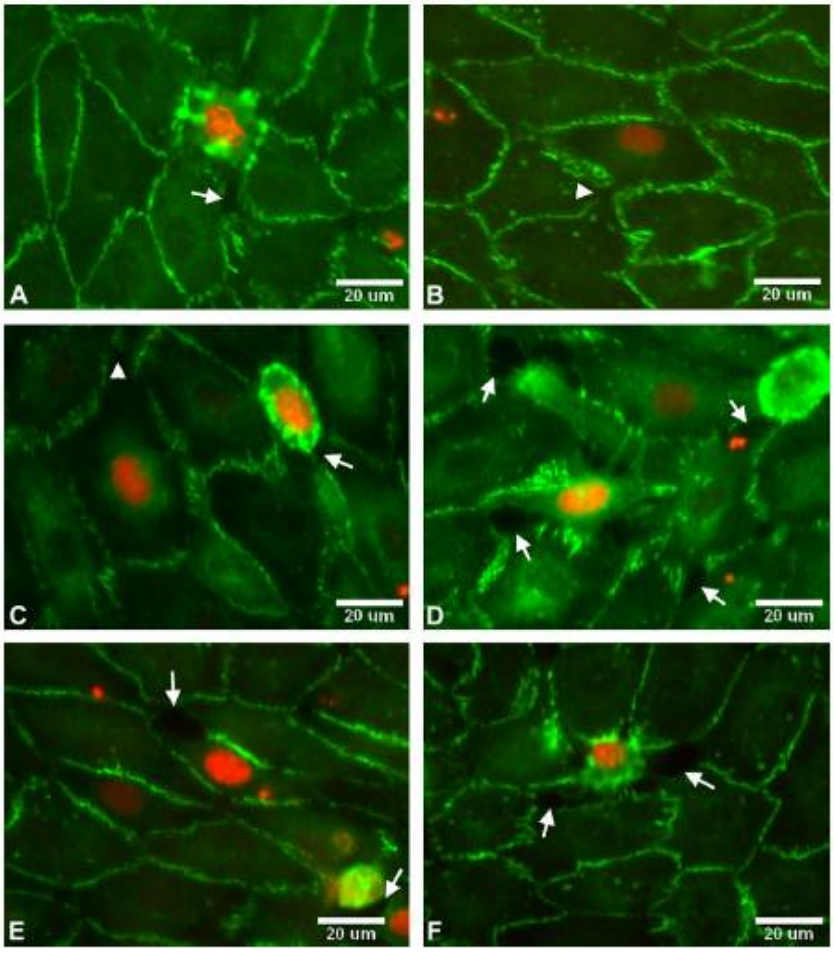

Figure 21: The endothelial cell detachment and gap formation by the apoptosis [15]. A and B shows the control case; C and D is treated with TNFα/CHX. The arrows show the gap formation and detachment from BAEC monolayer.

periments using rabbit intercostals, celiac, and iliac branches of the aorta, which are recognized as regions highly susceptible to atherosclerosis, the permeability of LDL was higher than in neighboring regions. The similarity between the distribution and occurrence of the elevated $I^{125}-LDL$ and HRP (Horseradish Peroxidase) permeability to LDL shows that the transcytosis pathway cannot explain the different distributions of LDL permeability, and strengthens the argument that broken inter-endothelial cell junctions, i.e., leaky junctions, may account for such higher permeability at different sites [37].

The role of leaky junctions in LDL transport is shown clearly in the research

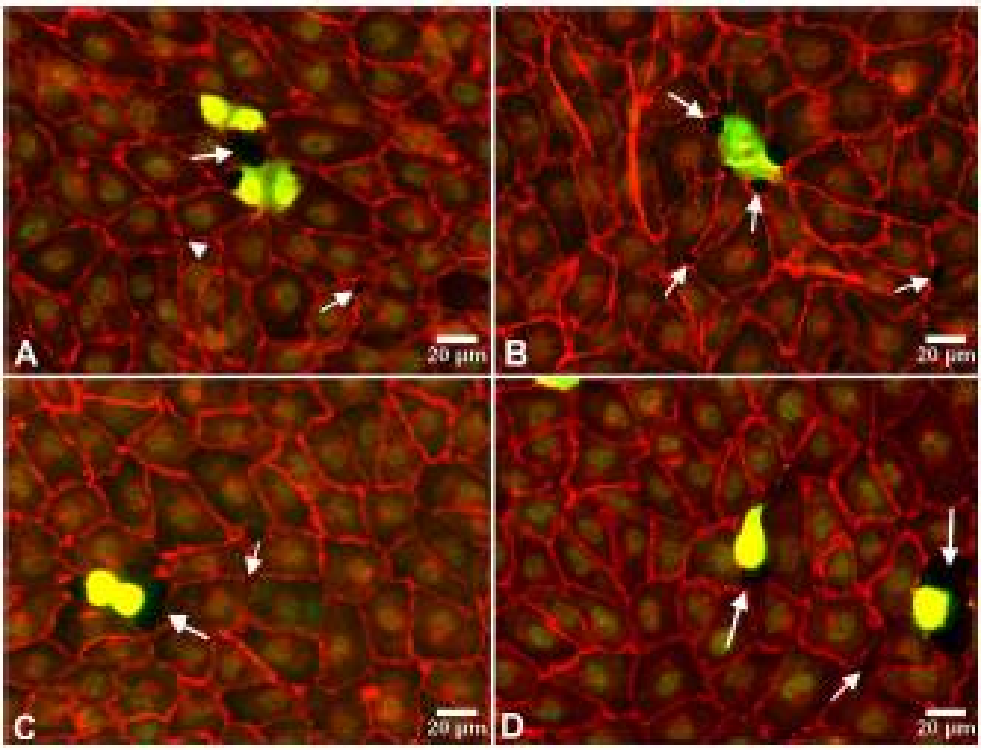

Figure 22: The endothelial cell detachment and gap formation by the mitosis [16]. A and B is the control case; C and D is treated with paclitaxel for 3h. The arrows in each diagram denote gap formation

done by Cancel et al. [15, 16]. The apoptosis rate in BAEC monolayers which were plated on porous polyester filters was elevated by TNFα and cycloheximide(CHX). The apoptotic cells were immunostained by the Tunel method and were visualized by red color in Fig. 21. The comparison between the control case and the increase of apoptosis rate in the endothelium shows that more gaps seen as black spots build up around the apoptotic cells and the inter-endothelial cell junctions which are observed as green line by $ZO-1$ immmunostaining. They measured the change of LDL permeability and volume flux of water and found that gap formation caused by apoptosis enhanced more LDL particles passing through the endothelium with more convective flux. It was shown that there is a linear correlation between apoptosis and LDL permeability. The mitosis effect on LDL permeability was also demonstrated with the same method. BAEC monolayers were treated with paclitaxel, which induced mitosis.

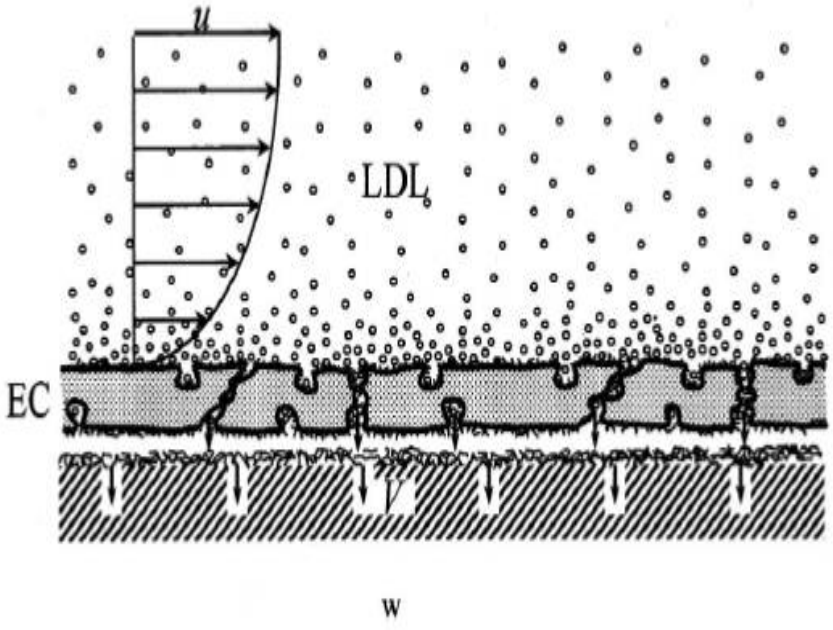

Figure 23: A schematic drawing of diffusive and convective transport of low density lipoproteins (LDL) in blood flow in an artery with a semipermeable wall. Transmural fluid filtration produces a concentration polarization layer at the surface of the endothelial cells [95]

Mitotic cells, which were immunostained by MPM-2 and visualized with green color, caused the cell turnover and creates more gap formation in the BAEC monolayer. In Fig. 22 gaps seen as black spots were formed around the mitotic cells and the inter-cellular junctions which were immunostained with VE(vascular endothelial)-cadherin. They also found that there is a linear correlation between the mitosis rate and LDL permeability.

The endothelium provides the major resistance to LDL transport between blood and blood vessel wall because of the semi-permeable nature of the endothelium to macromolecules [81]. If there are no leaky junctions, the filtration flow caused by the pressure gradient between luminal surface and the wall brings LDL particles into the cell junction, carried by the plasma flow which can pass through inter-cellular junction freely. However, LDL particles brought by filtration flow are stuck around

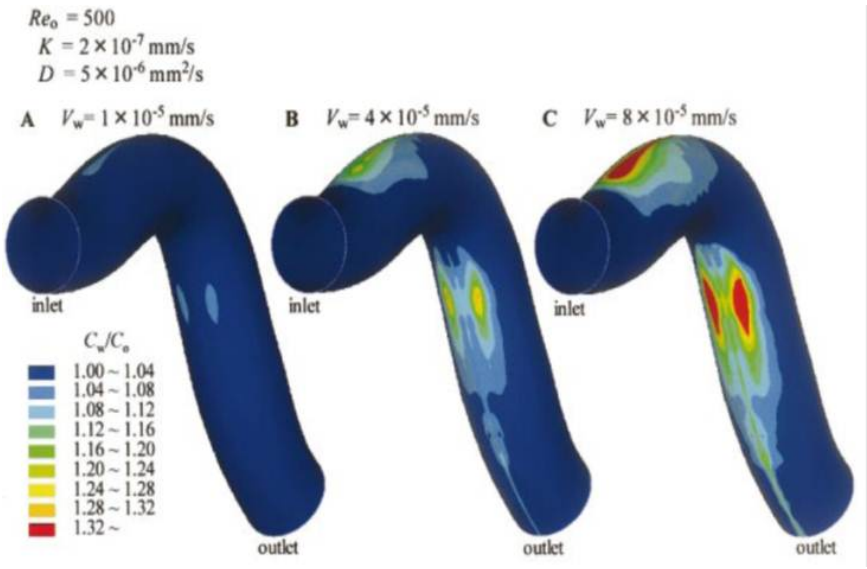

Figure 24: The effect of filtration flow on LDL accumulation at the blood vessel surface [96]

the inter-cellular junction, making a high concentration on the endothelial surface. A schematic diagram is presented in Fig. 23, and the occurrence of this phenomenon has been demonstrated with numerical methods in a straight cylindrical tube [95] and an artery with multiple bends [96]. Deng X et al. [27] investigated the filtration flow effect on LDL mass transfer in canine carotid arteries using computational models and in-vitro experiments. As the filtration velocity increased, the concentration of LDL on the endothelium surface was higher, even though the faster main flow decreased the accumulation of LDL. This was verified with the experiment in which different pressures were applied to the artery and the LDL concentration change was measured. Higher concentration of particles was observed when the filtration flow was increased due to the higher pressure gradient in the artery.

For LDL particles passing through the endothelium and stuck in the intima, it is necessary that both the filtration flow and the leaky junction formation work together. In other words, if the region experiences high filtration flow but there are no leaky junctions, LDL cannot move into the intima; and, in contrast, even if leaky junctions form at the site but there is no convective flow, this region has little chance to

develop atheroma. The research by Meyer et al. [58] supports this concept. In their investigation no increase of LDL infiltration in the arterial wall was observed when the arterial wall was wrapped with external rigid polyester sleeves to prevent the wall stretch with pressure change from $120mmHg$ to $160mmHg$. In contrast, when the arterial wall was stretched freely without any hindrance, a increase of LDL concentration in the intima was observed. This can be explained by the fact that the arterial stretch is reported to contribute to a high rate of apoptosis and mitosis of endothelial cells, which leads to leaky formation and then enhances LDL particle entry into the intima.

LDL mass transfer has been described by three models depending on how the arterial wall is treated; a wall-free model, a single-layer model, and a multilayer model. In the wall free model, LDL concentration on the luminal surface is determined simply by blood flow and convection-diffusion model [29, 95, 96]. In the single-layered model, the wall is treated as single porous media with homogeneous parameters for mass transport on the assumption that the arterial wall is a fiber matrix sturcture [81, 49, 65], and in some cases the permeability to LDL changes with WSS and the filtration flow is calculated using Brinkmanns or Darcy′s model [86]. In a multi-layer model, instead of a single porous media the wall is treated as a complex structure consisting of the intima, IEL (internal elastic lamina) and the media [87, 68]. Multi-layer models can give more detailed distribution of LDL in the wall, but multi-layer models need more transport parameters which are hard to obtain under current experimental methods because each region needs its own parameters, i.e, the permeabilty, LDL consumption rate and resistance to plasma flow.

With current medical imaging methods it seems impossible to separate detailed structures in an in-vivo geometry. For this reason, if the main purpose of the research is not a LDL distribution in the arterial wall, then single layer model may be adequate to describe the LDL mass transport in an in-vivo artery. In our investigation, the

nature of LDL mass flux over the arterial surface is considered to be a major factor in assessing plaque progression, and thus it is more critical to set up a proper model on the endothelial surface than within the vessel wall.

In Chapter 3, based on an in-vivo carotid artery geometry (subject 2), blood flow is calculated to extract WSS and gives the convective force driving LDL particles in the lumen. Coupled with this, at the interface between the lumen and arterial wall, constant permeability and filtration flow are assumed to model their effects on the concentration of LDL.

3.2 CFD of Blood Flow in Large Arteries

Blood is a concentrated suspension containing red blood cells (erythrocytes), white blood cells (leukocytes), and platelets. In blood, the hematocrit (the volume fraction of blood constituents) of red blood cells is 40% to 50% and under physiological conditions WBCs occupy 1/600 and platelets occupy 1/800 of total cell volume. This means the RBC is responsible for the dominant characteristics of blood. Blood shows non-Newtonian characteristics, in which the viscosity is higher at low shear rate and approaches an asymptotic value, with increasing shear rate. The RBCs aggregate with each other through a shear dependent protein interaction (fibrinogen and immunoglobulins) on the surface of RBCs, and this aggregation leads to rouleaux formation (long chain aggregates of RBCs) at low shear. In turn, larger rouleaux increase the effective viscosity coefficient through increased energy dissipation.

However, for several reasons a Newtonian model is used in our research. First, various non-Newtonian models which are used in hemodynamic simulations are obtained from parameters fitted to experimental data at various shear rates under steady-state conditions. These models do not reflect accurately the formation of rouleaux in the transient case of pulsatile flow. Second, the shear rate in the large arteries is sufficiently large to break up the protein interaction causing rouleaux [8]. Only if a region

experiences very low shear for prolonged periods is there adequate time for rouleaux to form [5, 44].

Blood flow in arteries is assumed to be laminar because the Reynolds numbers (Re) are usually much lower than those required for turbulent flow to develop. For example, the time-averaged Reynolds number in human coronary artery is reported to be around 240 by He X et al. [36]. While there are clearly exceptions, e.g., post stenotic flow in significantly diseased arteries and transient turbulence in the aorta with high cardiac output, for many studies of physiologic relevance, a laminar flow assumption is accurate.

In general, the flow can be treated as a continuum in which flow parameters and variables are continuous in space and time without abrupt changes or discontinuities. Further, temperature of blood is well regulated at a constant value ($37°C$), and temperature effects on blood viscosity can usually be neglected. Thus, blood flow in large arteries under most situations can be described by the Navier-Stokes Equations (N-S), in which the hemodynamic variables are calculated based on mass conservation and momentum balance in the finite volume. In our study blood is assumed to be incompressible Newtonian fluid with a viscosity of $\mu_{blood} = 0.00345(P \cdot s)$ and a constant density of $\rho_{blood} = 1050(kg/m^3)$.

The Navier-Stokes equations in this category are as follows;

$$\overbrace{\rho_{blood}(\underbrace{\frac{\partial v}{\partial t}}_{Local\ acceleration} + \underbrace{v \cdot \nabla v}_{Convective\ acceleartion})}^{Inertia} = \underbrace{-\nabla p}_{Pressure\ gradient} + \mu_{blood}\underbrace{\nabla^2 v}_{Viscosity} + F \quad (1)$$

$$\nabla \cdot v = 0 \quad (2)$$

where v is the fluid velocity, F represents body forces (such as gravity), and p is the pressure. The numerical results are obtained using the commercial FVM (Finite Volume Method) code, Fluent (v3.2.26 Fluent Inc., Lebanon, NH, USA), in which the fluid domain is divided into finite volumes. The Navier-Stokes equations are

integrated over these finite volumes, and the resulting nonlinear partial equations are solved simultaneously, using an iterative procedure with appropriate boundary and initial conditions. In the finite volume, the velocity change in the left side of N-S is balanced with the pressure gradient due to the difference between the inlet and the outlet pressure and the viscosity of the blood which acts as the frictional force against the blood flow at surface interfaces. Depending on the physical environment, force fields such as gravity can be counted in the force balance, but in the case of blood simulation in a large artery the gravitational force is ignored.

For the pulsatile simulations, a phasic volume flow rate waveform for the left carotid artery of subject 2, obtained from PC MRI, is employed. In Fig. 18, inflow Q_{CCA} and outflow Q_{ICA} / Q_{ECA} were reconstructed by curve fitting based on the PC MR data. Owing to the presence of image noise and small outflow through minor branches that are not modeled, we do not expect the measured inflow rate (Q_{CCA}) and the outflow rate ($Q_{ICA} + Q_{ECA}$) to be same. Also, it is not possible to prescribe PC MR data at all these boundary sites in the CFD calculation due to numerical procedures that cannot account for small numerical errors in satisfying conservation of mass. Thus, the outflow at ICA/ECA is imposed and the traction free (static pressure, $p = 0$) boundary condition is prescribed at the CCA. This has the advantage of capturing both the total flow exiting the domain of interest, as well as the flow division into ICA and ECA, a critical determinant of flow patterns. In pulsatile simulations, calculations are performed for three cardiac cycles in which the results from the previous cycle are used as initial conditions for the subsequent one. This approach ensures dynamic equilibrium and improves the accuracy of the computations because of eliminating start-up effects of transient simulation of the flow.

A fine numerical mesh in the boundary layer is necessary to detect accurately the gradient of velocity near the wall, wall shear stress and concentration of solute in the

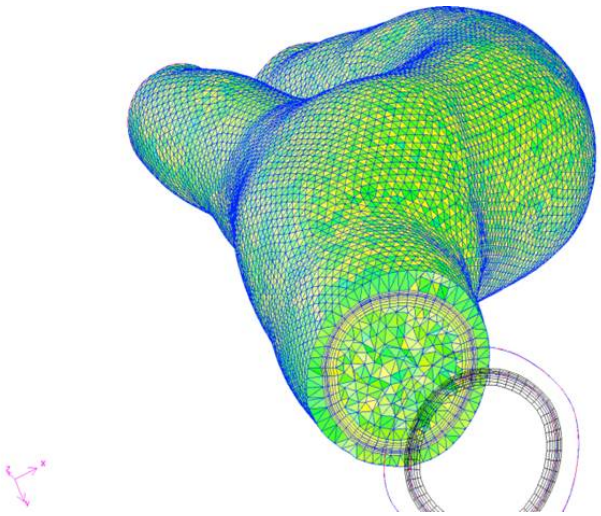

Figure 25: Volume meshing and the boundary layer of subject 2

CFD calculation. In the pulsatile simulations the oscillatory boundary layer thickness is defined as:

$$\delta = \sqrt{\frac{2\mu_{blood}}{\rho_{blood}\omega}} \tag{3}$$

where δ is oscillatory boundary layer thickness and ω is the frequency of the cardiac cycle. The in-vivo arterial geometry handled by Geomagic is exported as a CAD file format into the CFD preprocessing program Gambit (v2.3.16 Fluent Inc., Lebanon, NH, USA) which makes the surface and volume meshes, and the mesh, in turn, is exported to Fluent (CFD code). Near the interface, four mesh layers were constructed in the thickness of the oscillatory boundary layer (Fig. 25). In remaining parts, tetrahedral meshes were used due to the complicated geometry of the artery. All volume meshing is controlled to have a reasonable range of skewness under 0.8.

3.3 LDL Concentration with Constant Filtration and Endothelial Permeability to LDL Particles

3.3.1 Convection Diffusion Equation for mass transfer of bioparticles

To describe mass transfer of atherogenic material in arteries, convection diffusion equations (C-D) are utilized as governing equations to implement the computational

calculation. In general, the solute concentration is determined from the balance between convective forces and the diffusion of the particle. The C-D equation is expressed as:

$$\frac{\partial C}{\partial t} + v \cdot \nabla C = D\nabla^2 C + R \tag{4}$$

where C is the concentration of solute dissolved in the lumen and v is the velocity vector of blood which couples mass transport to the Navier-Stokes equation (N-S). D is the diffusivity of the bioparticle, and R is the chemical reaction which represents the generation or destruction of the particles. In the C-D equation the time rate of change of the concentration is determined from the balance between the convective mass brought by the blood flow, expressed by the multiplication of velocity and the gradient of concentration, and the dispersion, which is expressed by the multiplication of diffusivity and the Laplacian of the concentration. In some cases, an extra term, expressed as R, is included and contributes to determine the concentration balance. In this study, the interface boundary condition at luminal surface is implemented as R, a surface chemical reaction model. Depending on the solute features, the diffusivity of solute is usually a function of concentration or velocity of the flow, but this parameter is treated as a constant value due to the low diffusivity of LDL. In mass transport with high diffusivity, the fluid flow and mass transport should be calculated at the same time at each time point. However, the low diffusivity of LDL makes it possible to separate the blood flow calculation using the N-S equation (Eqn. (1)) and LDL mass transport with C-D equation (Eqn. (4)). Thus, to save computational resources the N-S solution is run first and the C-D is calculated next based on the velocity at each mesh point.

Through the normalization of Eqn. (4) using the diffusivity of LDL, inlet reference concentration and reference values, i.e., the inlet velocity and the domain dimension, the physically important parameters related with mass transport become apparent and demonstrate the contribution of each factor to LDL movement. The normalized

C-D equation then takes the following form;

$$4\alpha^2 \frac{\partial \bar{C}}{\partial t} + R_e \bar{v} \cdot \nabla \bar{C} = \frac{1}{S_c} \nabla^2 \bar{v} + \bar{R} \tag{5}$$

where $\bar{C}$ is the normalized concentration ($\bar{C} = C/C_{inlet}$), where C_{inlet} is the inlet reference concentration and $\bar{R}$ is a dimensionless reaction rate term [29]. In the above equation, α is the Womersley number which expresses pulsatile flow frequency in relation to viscous effects and defined as $\alpha = \frac{D_{inlet}}{2}\sqrt{\frac{\omega}{\nu}}$ (ν is a kinematic viscosity). R_e ($= \frac{VD_{inlet}}{\nu}$, D_{inlet} is the diameter of the inlet of the artery and V is the averaged velocity at the inlet) is the Reynolds number which gives the ratio of the viscous force and the inertial force. S_c is the Schmidt number ($S_c = \frac{\nu}{D}$) which represents the ratio of the viscous force and the diffusion rate. Among these parameters the most meaningful parameter related to LDL mass transport is the Peclet number ($R_e \times S_c = \frac{VD_{inlet}}{D}$) which characterizes mass transport by representing the relative importance of convection by fluid flow versus the diffusive effect of bioparticles. In our research the S_c of LDL is about 66 and the corresponding Peclet number is much higher than 1000. This means that in mass transfer in large and medium sized arteries convection dominates diffusion of solute in the blood flow. For this reason the blood flow patterns in the lumen and the filtration flow in the wall are critical in determining the distribution of LDL along the arterial surface.

In most of cases of mass transport simulation, uniform concentration is applied as the inlet boundary condition (Dirichlet condition), and we use C_{inlet} =1.2 mg/ml of blood [81]. At the outlet a homogeneous Neumann condition (a zero value for species gradient) is typically imposed, especially for the high Peclet number case. Second and first order upwinding schemes are used for the mass-momentum and species solvers, respectively. The QUICK scheme [52] is employed to solve the flow and species transport equations. The time discretization and pressure-velocity coupling are achieved through second order time implicit and PISO schemes (the pressure-implicit with splitting of operators), respectively. To detect LDL concentration more

accurately, the mass transport boundary layer is applied on the surface and this layer is determined by the following relationship;

$$\delta_{S_c} \cong \frac{\delta}{S_c{}^{\frac{1}{3}}} \tag{6}$$

where δ is the oscillatory boundary layer in Eqn. (3).

3.3.2 Wall boundary condition

Based on the mechanism explained in a previous section, the equilibrium concentration of particles at the interface between blood and endothelium is established based on a mass conservation law which states that the amount of LDL passing through the endothelium is determined by a difference between the amount of LDL carried into the wall by a filtration flow and the amount which diffuses back to the blood mainstream. Mathematically, this takes the following form:

$$C_s v_w - D\frac{\partial C}{\partial n}\bigg|_{wall} = K(C_s - C_w) \tag{7}$$

where C_s is the luminal species concentration at the endothelial surface and C_w is the wall concentration beneath the endothelium. v_w is the plasma filtration velocity normal to the wall ($= 4 \times 10^{-6} cm/s$) [81], n is the direction vector normal to the wall, and D is the physiological LDL diffusivity. Using the Stokes-Einsten equation, the diffusivity of LDL was estimated to be $5 \times 10^{-8} cm^2/s$ in blood at body temperature [96]. $K(= 2 \times 10^{-8} cm/s)$ is a net uptake mass transfer coefficient of LDL which is considered equivalent to the physiological endothelial permeability to LDL [81]. If the resistance to transport offered by the endothelium is dominant ($C_s \gg C_w$), then it is natural to assume Eqn. (7) transforms to the following:

$$C_s v_w - D\frac{\partial C}{\partial n}\bigg|_{wall} = K(C_s) \tag{8}$$

To implement the wall condition in the Fluent program, the Arrhenius rate for the surface reaction model is set on the interface. The mass rate of creation/destruction

of species $i^{'}$ in the reaction k is given by

$$R_{i',k} = \sum_{k=1}^{N_R} (k_{f,k}[C_{i'}]) \tag{9}$$

Where N_R is the number of the reaction, $k_{f,k}$ is the forward rate constant for reaction k and $C_{i'}$ is the mass concentration of species $i^{'}$. In a similar way, the surface reaction boundary condition is expressed with the balance in which the convection and diffusion of the species to or from the surface and the rate at which it is consumed or produced at the surface. This mass flux balance for the species $i^{'}$ is represented as

$$J_{i'} \cdot n = R_{i',k}$$

$$J_{i'} \cdot n = R_{i',k} = k_{f,k}[C_{i'}] = k_{f,k} C_s \tag{10}$$

$$D \frac{\partial C}{\partial n}\bigg|_{wall} = (v_w - K) C_s \tag{11}$$

where $J_{i'}$ is the diffusion flux of species and $R_{i',k}$ is interpreted as the mass rate of surface deposition of species. Thus, the final form in Fluent to calculate the chemical reaction on the surface is given in Eqn. (10). Through the comparison between the final form for Fluent and the rearranged form in Eqn. (11), $J_{i'} \cdot n$ is defined as $D \frac{\partial C}{\partial n}\Big|_{wall}$ and the $k_{f,k}$ is assigned by the difference between the filtration flow (v_w) and the permeability (K).

3.4 Results and Discussion

3.4.1 Flow patterns in the carotid artery

Streamlines and cross sectional velocity profiles were acquired throughout the pulsatile cycle, and the streamlines at a time during the deceleration phase for subject 2 are shown in Fig. 26 and 27. In subject 2 the pronounced curvature of the ICA and geometrical non planarity between the CCA and ICA/ECA combined with the slight stenosis around the outer wall of the carotid bulb induce complicated flow patterns in the carotid bifurcation. To track the particle movement in the artery the streamlines

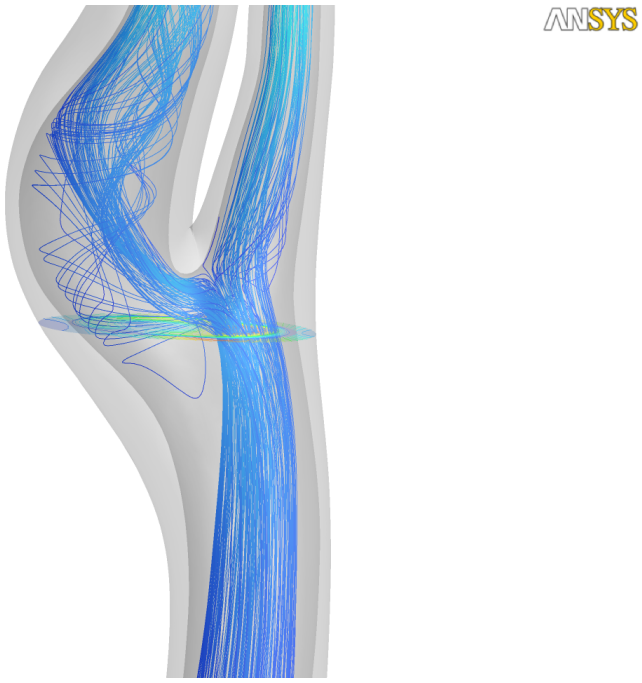

(a) Streamlines from CCA inlet

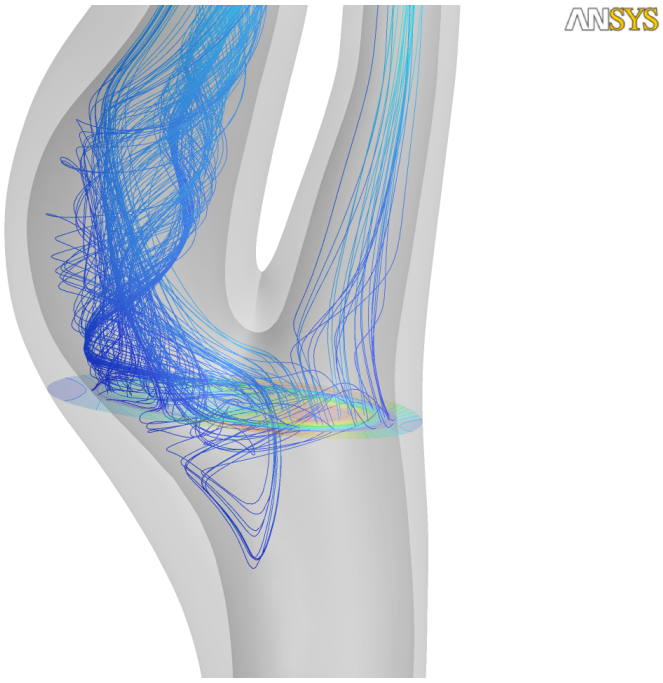

(b) Streamlines from the cross section of beginning of the bifurcation

Figure 26: Streamlines calculated at the beginning of acceleration in diastole (BAD) in carotid artery in subject 2

were calculated from the CCA inlet to ICA/ECA outlet (Fig. 26 (a)), and they were also obtained from the cross section at the beginning of the bifurcation at the same time to visualize more specific streamline patterns in the carotid bulb and downstream of the stenosis (Fig. 26 (b)). Particles which travel around the periphery of the inner wall in the CCA near the proximal ICA enter a transient separation zone at the carotid bulb and are twisted up via complex, helical flow patterns.

A more detailed velocity field is presented at four typical cross sections in Fig. 27. At the proximal section of the stenosis small areas of reverse flow can be noted around the stenosis even though there is little asymmetric flow patterns in the carotid artery (Fig. 27 (c)). After the stenosis the flow patterns show the intense reverse flow and a strong vortex flow at the same time in the carotid bulb because the expansion of the cross sectional area makes the main flow lose the inertial force, and the beginning of the tortuous curvature of the ICA induces faster flow movement in the anterior side of carotid bulb, which strengthens the recirculation pattern at this site (Fig. 27 (d)). In contrast to the ideal bifurcation model in which the planar bifurcation and lack of tortuous curvature in the ICA [50] create a symmetrical secondary flow in the cartotid bulb, an asymmetrical, strong vortex pattern is present near the proximal ICA. At the region which experiences the reverse flow caused by the strong vortex, the development of intimal-medial thickness (IMT) is also observed. The complicated helical flow extends after the bifurcation apex, and this triggers a vortex and reverse flow at the inner wall of the ICA, a flow pattern that is not seen to a remarkable degree in the ECA (Fig. 27 (e)). In contrast, flow in the ECA is relatively uniform and no vortex or circulation region is present due to its simpler geometrical feature. There is no tortuous curvature in the ECA, and the connecting angle between the ECA and CCA is small. The ECA flow patterns can be seen in the streamlines (Fig. 26), and a more or less fully developed velocity distribution over the cross section is found in the distal ECA (Fig. 27 (f)).

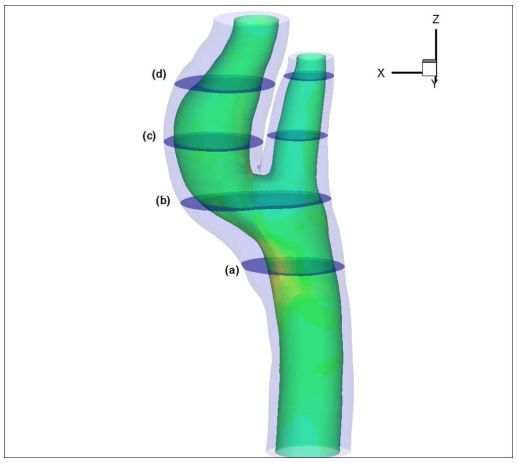

(a) Cross section in carotid artery

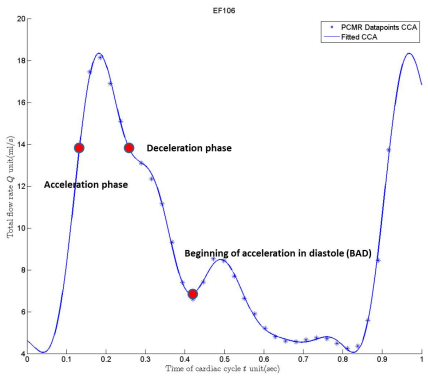

(b) Time points at acceleration, deceleration and BAD

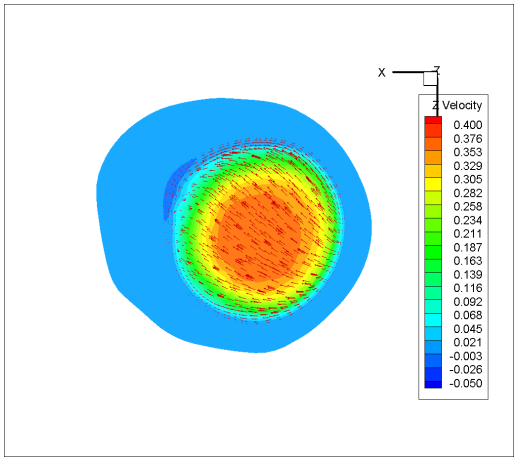

(c) Common carotid artery

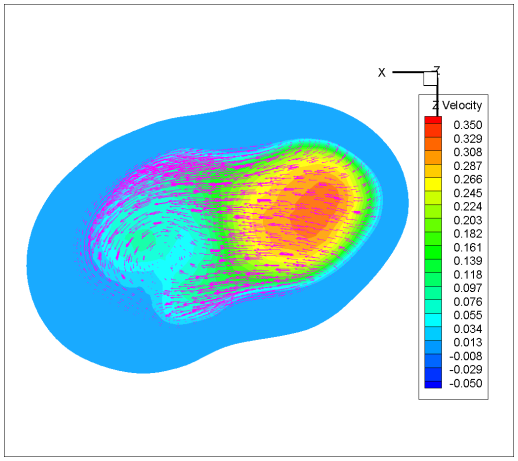

(d) Beginning of the bifurcation

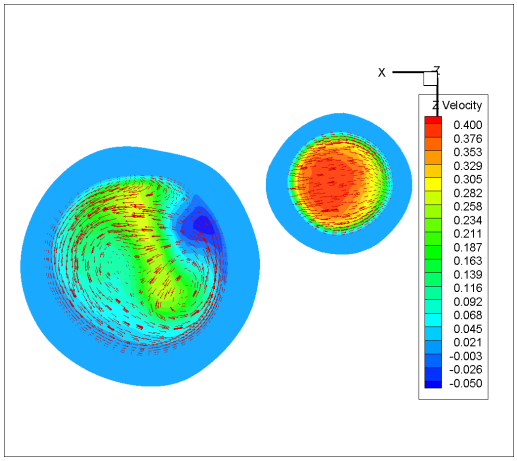

(e) Right after the apex

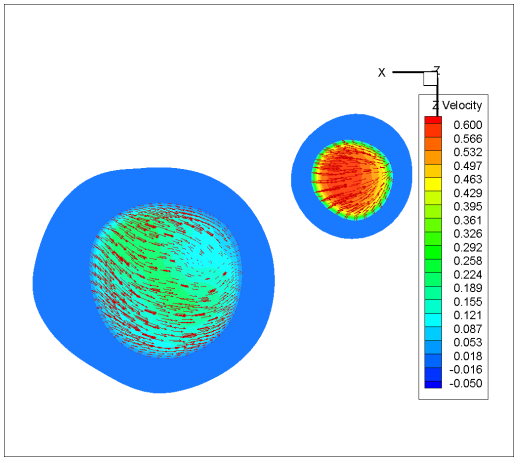

(f) Far away from bifurcation

Figure 27: Velocity cross-section patterns at the deceleration phase in the subject 2

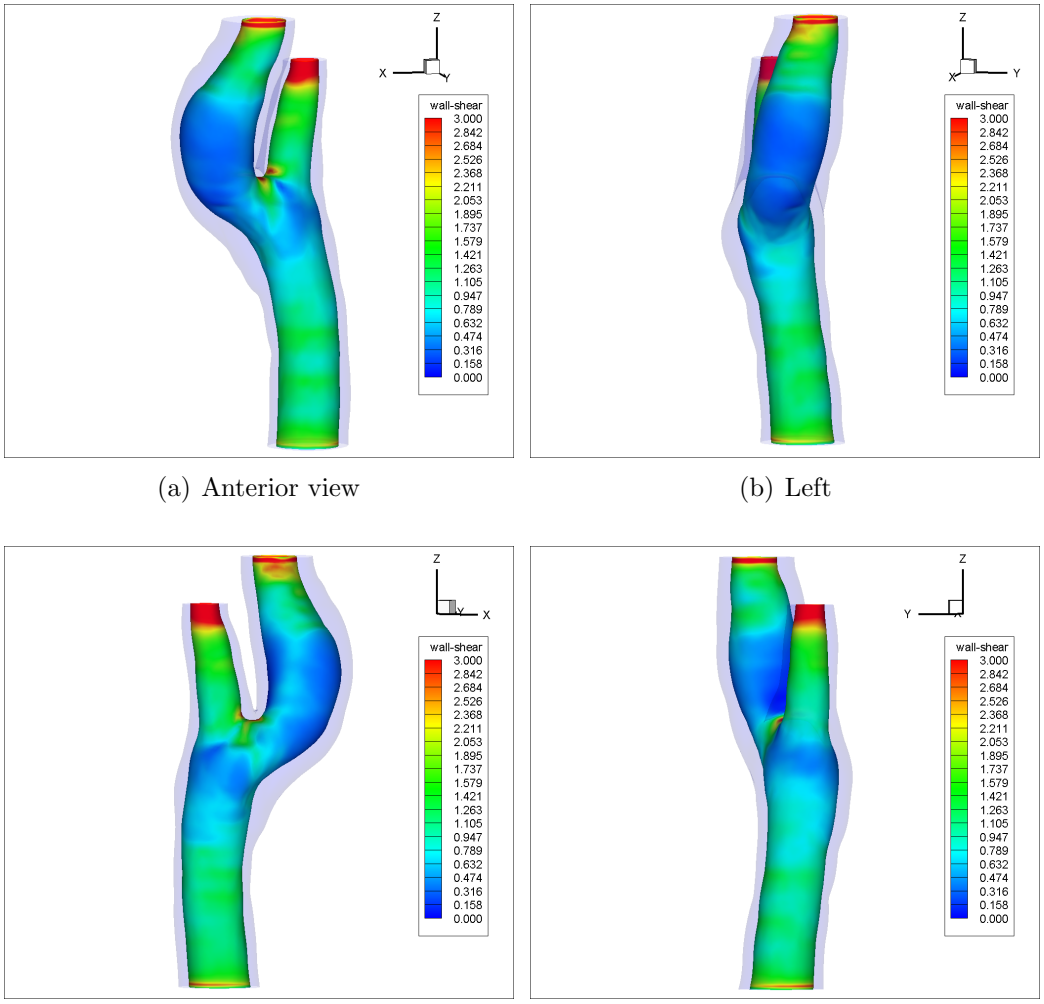

(a) Anterior view

(b) Left

(c) Posterior view

(d) Right

Figure 28: Wall shear stress distribution at human carotid artery at acceleration phase $Pa(N/m^2)$

3.4.2 Wall shear stress distribution

Wall shear stress (WSS) is defined as the product of the velocity gradient at the surface and the viscosity of the fluid. Thus, WSS distribution is associated closely with the flow patterns in the domain. For this reason WSS is extracted at two time points (Fig. 27 (b)) in the cardiac cycle and compared to determine how much the flow patterns influences its distribution. For a detailed view, the WSS distribution is provided via four aspects (Figs. 28, 29) due to asymmetric geometrical non-planarity. In this study low wall shear stress (LWSS) is defined to be when its value is under

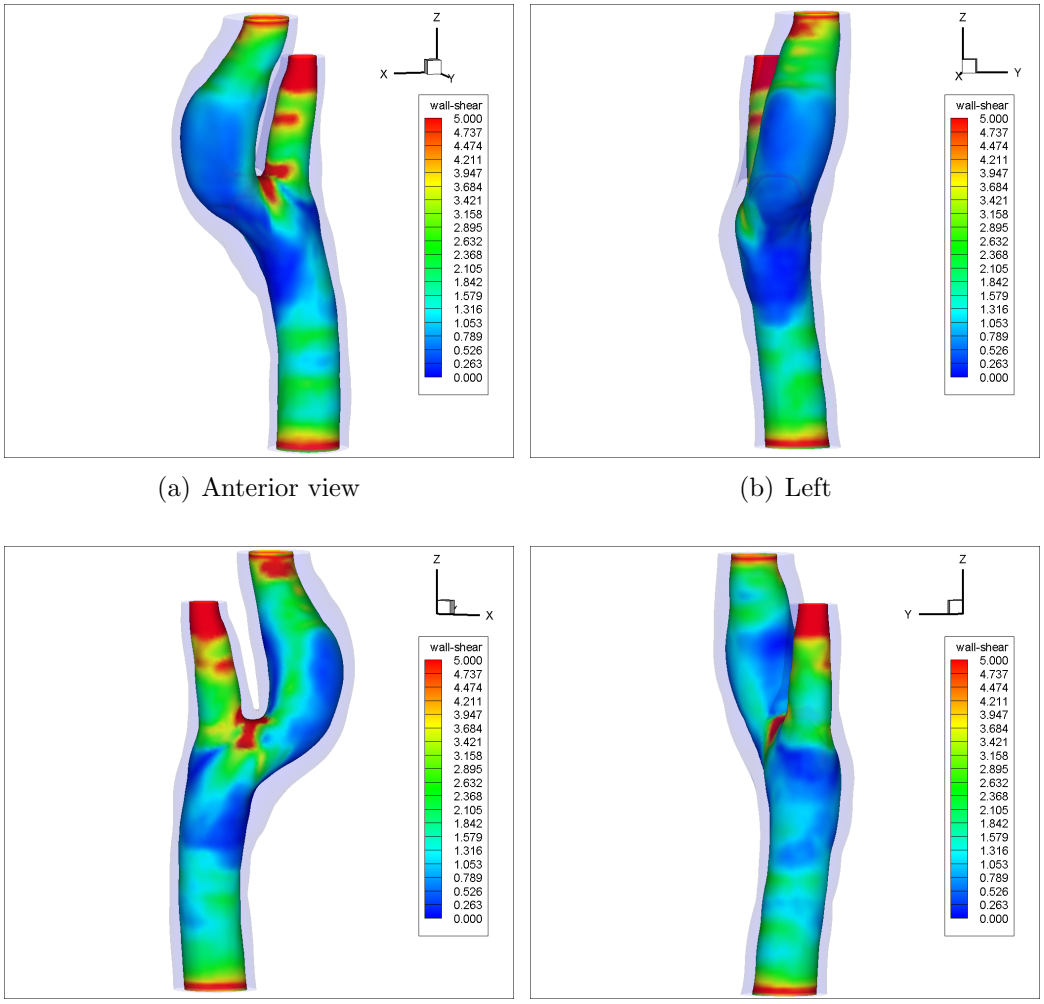

(a) Anterior view (b) Left

(c) Posterior view (d) Right

Figure 29: Wall shear stress distribution at human carotid artery at deceleration phase $Pa(N/m^2)$

$0.5Pa$. In the acceleration phase, the LWSS region begins along the outer wall of the conjunction between the ICA and CCA and covers most of the carotid bulb in the ICA. An interesting aspect of LWSS distribution at this time is that LWSS is present on the inner wall of ICA immediately after the bifurcation apex. In a previous study with ideal bifurcation geometry and no tortuous curvature of the ICA [50], the inner wall of the ICA experiences similar magnitudes of WSS as can be seen in the inner wall of ECA in Fig. 28 (a). In the deceleration phase, the LWSS region is much more extensive than in the acceleration phase, particularly around the stenosis and

including the CCA. The distribution of LWSS is overlapped in most parts at two time points but the lowest WSS is present both upstream and downstream of the stenosis in the deceleration phase. However, in the carotid bulb itself, the LWSS region is rather smaller than in the acceleration phase. This can be found through a comparison between the posterior views in Fig. 28 (c) and Fig. 29 (c). In both phases, high wall shear stress (HWSS) is dominant around bifurcation apex and extends through the ECA. HWSS presents in most of the area of ECA except the outer wall of the conjunction between the ECA and CCA (Fig. 29 (d)).

3.4.3 LDL transport in a 2D sudden expansion model

A sudden expansion model is a highly studied geometry with a well developed recirculation region. Thus, this geometry is suitable for simulating the convection dominant mass transfer of small biological molecules in blood flow. To evaluate the mass transport simulation accuracy using Fluent, the already published data by Lutostansky et al. [56] were used for the expansion geometry setup and comparison of the simulation results. The wall is assumed rigid and not permeable to solute, and the zero diffusive flux is applied as the boundary condition in the entire wall. This excludes other factors which influence mass transfer and focuses on convective effects on LDL transport. The inlet concentration is fixed as a unique value to give the incoming blood a constant LDL concentration. Material parameters in blood flow are the same used to simulate the blood flow in our in-vivo geometry. To simulate mass transfer in the same environment as the study of Lutostansky, the diffusivity of molecules and inlet velocity are changed based on the R_e and S_c which was described in section **3.3.1**, e.g., we use the same R_e and a range of S_c (10, 172, 430) to implement dynamic similarities in the blood flow and a similar characteristic behavior of molecules in the recirculation region. Under conditions of laminar flow and the axisymmetric

Table 2: Comparison cases based on R_e and S_c

Dr.Lutostansky	R_e	S_c	D
Case −1−	250	10	$1.17 \times 10^{-7}(m^2/s)$
Case −2−	250	172	$6.81 \times 10^{-9}(m^2/s)$
Case −3−	500	430	$2.73 \times 10^{-9}(m^2/s)$

Our research	R_e	S_c	D
Case −1−	250	10	$3.285 \times 10^{-7}(m^2/s)$
Case −2−	250	172	$1.910 \times 10^{-8}(m^2/s)$
Case −3−	500	430	$7.64 \times 10^{-9}(m^2/s)$

geometry, it is possible to use an axisymmetric simulation in order to save computational time. Recirculation occurs between the central flow and the expansion region. The axial-directional velocity is plotted in the sudden expansion region at the cross-sections corresponding to five different axial locations beginning from the sudden expansion. These velocity profiles are shown in the lower left diagrams in each Fig. $30 \sim 32$. It is observed that negative axial-directional velocities are present and that the negative axial-directional velocity exists further away from the origin of expansion as the value of R_e increase. This means that the recirculation region is larger as blood flow rate increases for a given expansion configuration.

The concentration of molecular species is plotted at the same sites as for the axial-directional velocity. In the lower right diagrams (Figs. $30 \sim 32$) the normalized concentration of solute at five axial locations is plotted as a function of the radius of expansion in which 0 is the centerline of the expansion model and 14 is the surface of wall. In each case, the concentration profile is similar between the results by Lutostansky and our research. The concentration around the central flow is similar to the inlet concentration, but approaching the wall the concentration decreases. Sharp gradients are observed between the main central flow and the recirculation region, although this trend is reduced and finally diminishes with increasing axial distances.

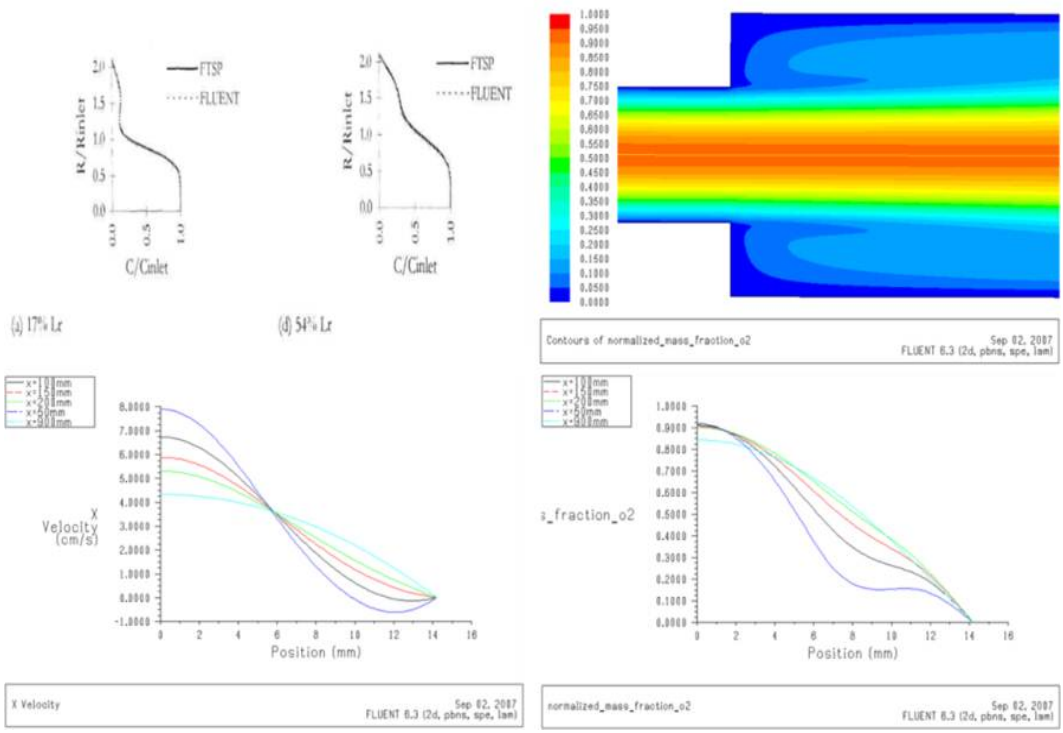

Figure 30: R_e250 and S_c 10

This trend is more definitive as S_c increases because the increase of S_c means that molecules have lower diffusivity and the convective force is more dominant as the diffusion effect is diminished. Thus, the mass transport of biological molecules with low diffusivity can be characterized by convective forces being dominant to diffusion. A greater concentration gradient is observed between central flow and the recirculation flow near the beginning of the expansion in Fig. 31 and 32 with the increase of S_c.

The large concentration difference across the streamline which separates the main flow and the recirculation flow induces diffusion of molecules and this causes the high concentration in the recirculation with high S_c. Nonetheless, the molecules have low diffusivity and this makes diffusion limited in the recirculation region so that the molecules principally follow the blood flow movement. For this reason in the recirculation region a second maximum concentration is detected near the surface and this peak value increases with higher S_c.

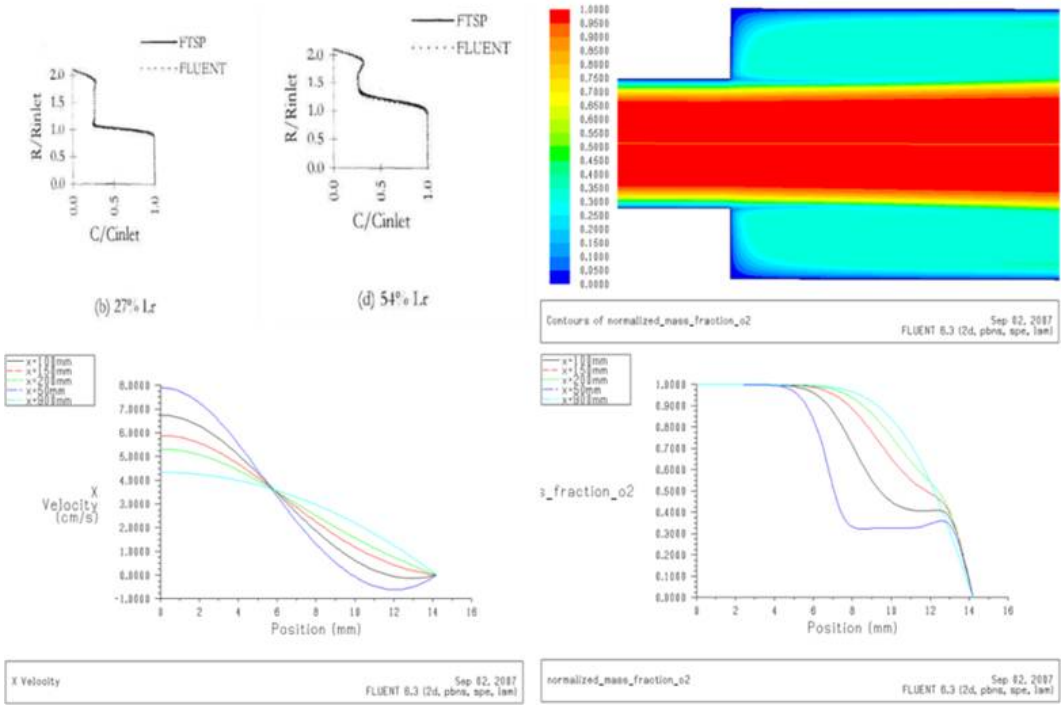

Figure 31: R_e250 and S_c 172

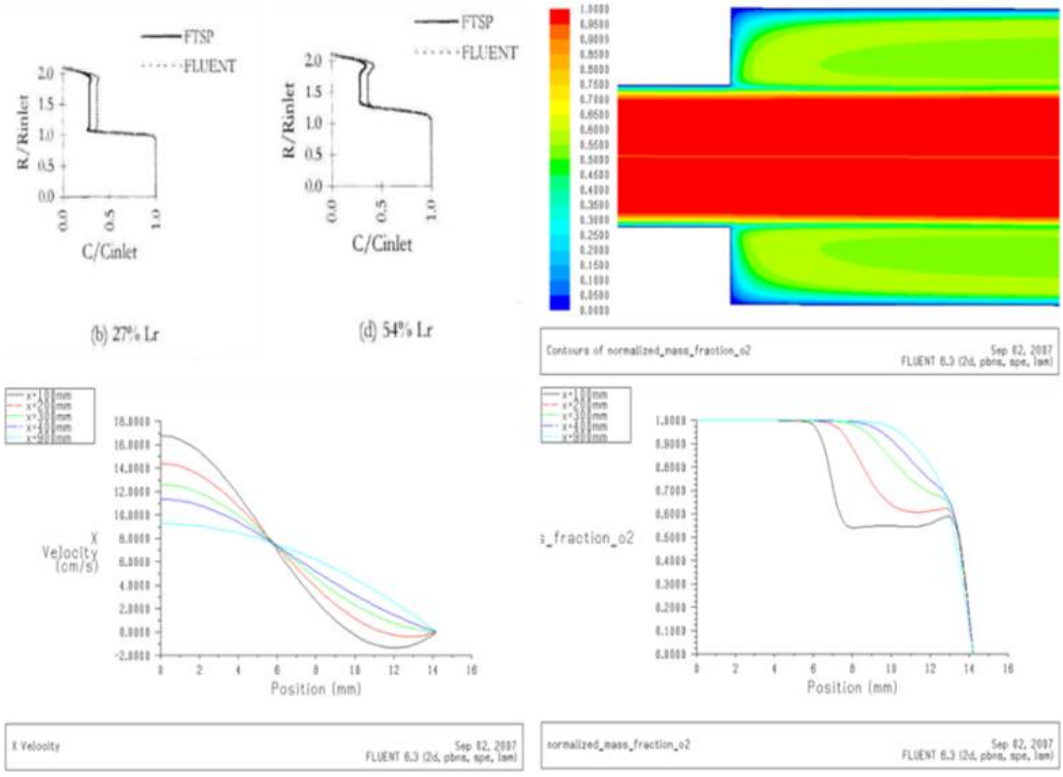

Figure 32: R_e250 and S_c 430

3.4.4 LDL distribution in a human carotid artery

LDL particles enter the CCA inlet with initial concentration and are moved by the blood flow which is calculated with the N-S equation and the C-D equation. At sites which experience low velocity they have long resistance times near the surface, and the final concentration of LDL is determined by the balance between filtration flow and endothelial permeability to LDL. The wall condition represented by Eqn. (11) is implemented on the surface of subject 2 with the Fluent chemical surface reaction model.

Figures 33 and 34 present results for the computed LDL concentration at lumen surfaces extracted at two time points during the cycle, one during the acceleration phase and one during deceleration, and normalized by inlet concentration. The filtration flow effect is applied at all surfaces so that the concentration is higher than unity, over the luminal surfaces. In the acceleration phase, a relatively high concentration is present around the proximal region of the stenosis, from upstream in the CCA and spreading into the stenotic region (Fig. 33). However, high concentration is not dominant after the stenosis in the carotid bulb. Even though there is a somewhat higher concentration present after the stenosis, it is much smaller than at the upstream of site. In the wall shear stress distribution results (Fig. 28) LWSS is dominant after the stenosis in the carotid bulb at the acceleration phase. However, the LDL concentration does not follow this trend. In the deceleration phase LWSS is prominant around the stenosis region and LDL distribution shows a similar pattern at this site in that the concentration is relatively elevated (Fig. 34). But still there is no remarkably high concentration after the stenosis in the carotid bulb even though the concentration itself is higher than in the acceleration phase.

The increase of concentration level of LDL is less than 3% of the inlet concentration which represents the average concentration in the blood. This value is very similar to the results of Prosi et al. [68]. In their research they used a low filtration flow

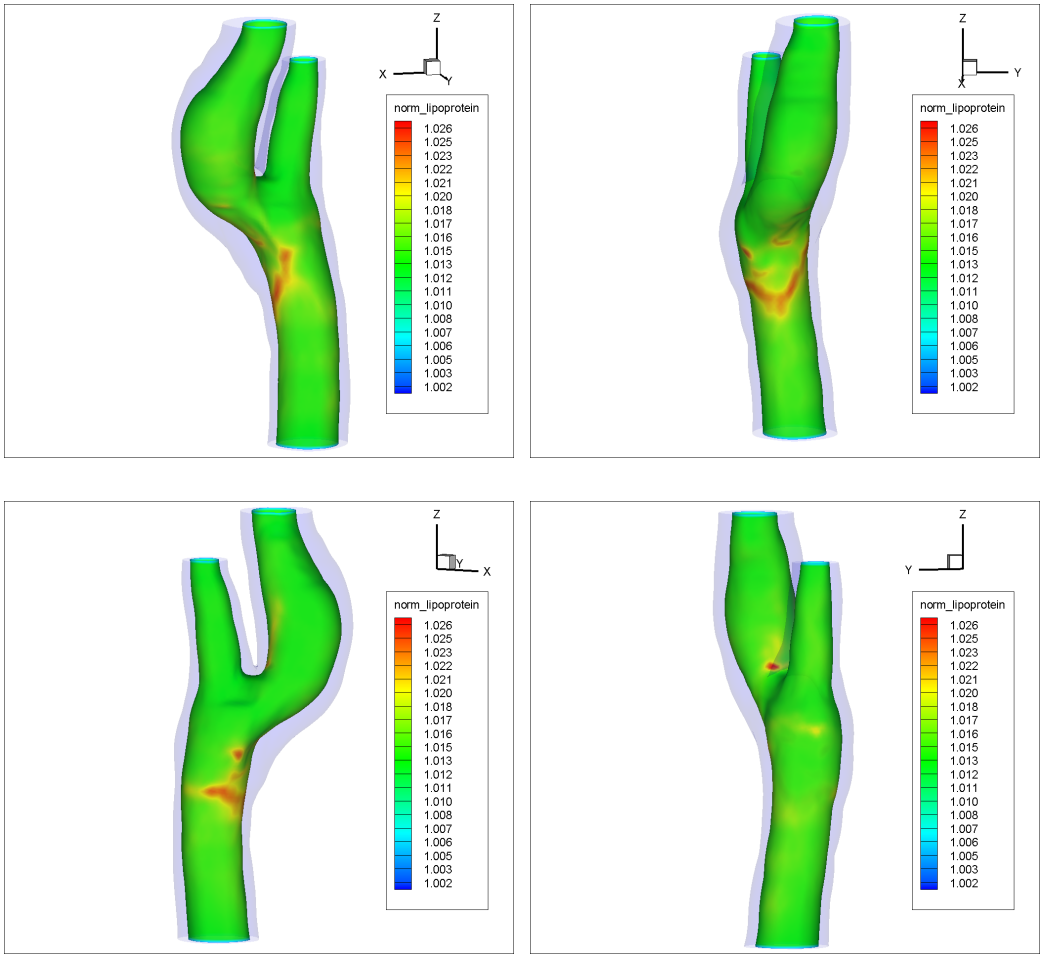

Figure 33: LDL concentration at the lumen surface at acceleration phase in subject 2

compared to our case, but they also used low diffusivity, resulting in a similar mass concentration on the surface. In both phases in the cardiac cycle, there is no apparent change in the concentration of LDL in the ECA.

The LDL distribution calculated with constant permeability and filtration flow applied on all surfaces shows that this boundary condition is not enough to catch the expected LDL concentration level and distribution on the surface. For example, from clinical evidence, plaque progression is often seen at the downstream regions of the stenosis, but the above results suggest that the upstream should be more susceptible to progression. And the polarization level is negligible to give a significant effect the

plaque formation, at least in the human carotid arteries in this study.

This difference may arise from the simplification of the boundary conditions. To overcome this limitation, several improvements should be investigated. First is the implementation of the physiological response of the endothelium to the dynamic mechanical environment. The rate of apoptosis and mitosis of endothelial cells responds to wall shear stress, implying that a mathematical model to couple apoptosis and mitosis with WSS should be included in the calculation [65]. Second is that more an accurate WSS distribution may result if the blood flow is computed not based on the rigid body but based on elastic arterial wall. To implement this, fluid structural interaction (FSI) should be utilized. Finally, the transmural filtration flow in an in-vivo artery is not a one-way pattern from the lumen to the arterial wall. There is a dynamic pattern to the arterial deformation caused by the pulsatility of the heart [49]. To get dynamic filtration flow it is necessary to consider poroelasticity in which the carotid artery is treated as a porous media and the filtration flow arises from hydro-mechanical coupling between pore fluid pressure and the geometrical deformation of porous media. With the above suggested approaches it may be available to obtain more accurate LDL mass transport results in the in-vivo carotid artery.

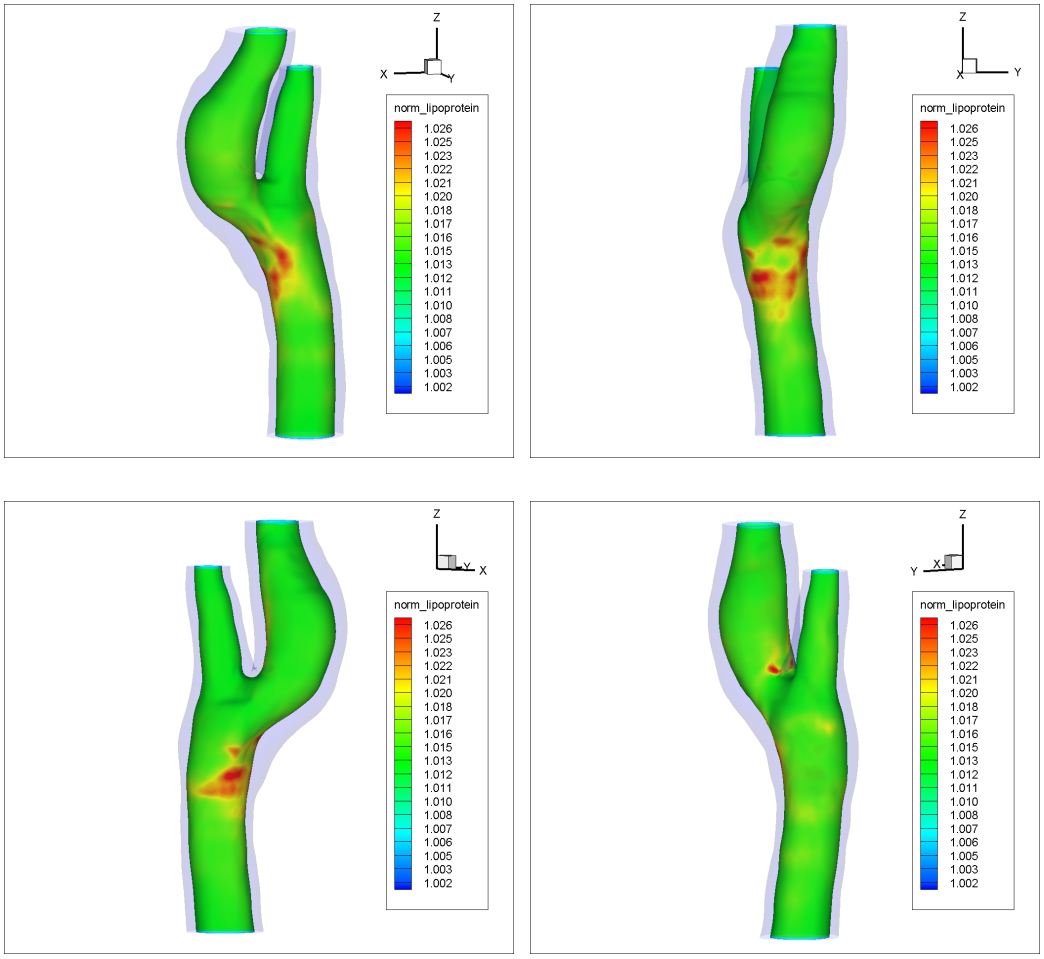

Figure 34: LDL concentration at the lumen surface at deceleration phase in subject 2

CHAPTER IV

FLUID STRUCTURE INTERACTION (FSI)

4.1 Background and Introduction

The arterial wall is a viscoelastic distensible soft tissue, and arteries experience dyanmic tension, compression and torsional forces which come from the pulsatility of blood flow related to the heart beat. Mechanical forces cause deformation of blood vessel geometry and the geometrical deformation also affects blood flow characteristic. This interactive coupling is called Fluid Structure Interaction (FSI). While there is a noticeably large amount of research and publications on blood flow done, fewer publications can be found investigating both blood flow and arterial wall mechanics using FSI algorithms.

In the study by Perktold et al. [67], blood flow in a distensible elastic wall model was simulated and compared to a rigid wall model of the bifurcation of the carotid artery. The pulse pressure waveform was applied to give the pulsatility to this artery. Even in the simplified ideal geometry with small changes in diameter, they found that the distensible wall affected the flow patterns of blood, causing changes in velocity and wall shear stress in the carotid sinus. The fully coupled simulation of pulsatile blood flow with a compliant stenotic artery was analyzed by Bathe et al. [7]. Three grades of stenosis corresponding to 51%, 89%, 96% nominal area reductions were used for the geometry, and they utilized the hyperelastic model to set up the structural features of the artery, which implemented a nonlinearity between stress and strain with the Ogden constitutive model [64]. Most of all, they found that significant cyclical compressive stresses developed downstream of the shoulder of the stenosis in the higher constriction models due to the strong pressure drop caused by the severe

stenosis, resulting in the pressure falling well below normal artery pressure. This compressive stress phenomenon was supported by similar research conducted by Tang et al. [90]. They set up a thick-wall stenosis model made of PVA (Polyvinyl Alcohol) hydrogel to mimic the artery and observed artery wall collapse due to compressive stress when the pressure difference between inlet and outlet was high (Fig. 35). Wall collapse was more prominent when the stenosis became more severe. In the severe plaque development case, the change of flow pattern caused by the deformation of the artery makes the throat of stenosis experience extremely high shear stress which can be as high as 3000 $dynes/cm^2$, values capable of damaging normal enthothelium. It is also reported that this high shear stress activates platelets and therefore contributes to thrombus formation [38].

The alteration of flow patterns causes LDL distribution changes in the lumen because LDL mass transfer is characterized by convective dominant mass transfer. Blood flow patterns and their effect on LDL mass transport were investigated based on symmetric and asymmetric compliant vessel walls by Valencia et al. [94]. In their research they compared the velocity and wall shear stress in the case of rigid body and compliant elastic models. They found that in the FSI simulation the mean velocity at the throat of the stenosis was much lower than in the case of the rigid body. Even though they applied very simplified boundary conditions for LDL mass transfer, LDL distribution alteration was observed downstream of the stenosis, where the flow recirculation magnitude changed with the response to the geometrical variation. Kolandavel et al. [48] showed that the dynamical curvature of the coronary artery wall influenced the LDL and oxygen mass transfer in the lumen through the alteration of flow depending on the wall curvature. While the wall deformation was prescribed a priori, their studies supported the effects of geometrical and dynamical environment on mass transfer in the lumen. Due to the above outcomes of the previous studies of FSI and its effect on the flow pattern and mass transfer in arteries, our research

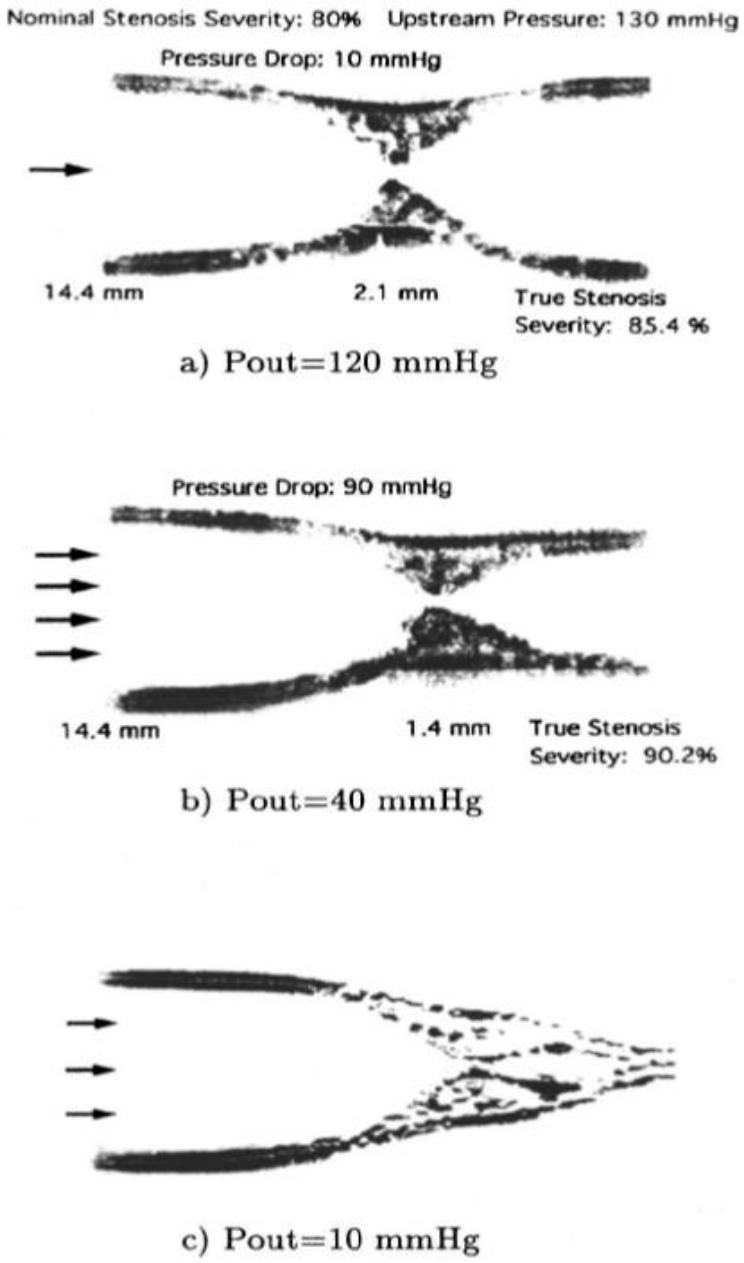

Figure 35: Experimental results showing collapse under physiological different pressure conditions [90]

examines employing FSI methods to obtain the complete data set including velocity, pressure and wall shear stress, wall displacement and mechanical stress.

It is a challenge to describe the interaction between incompressible blood flow and an elastic arterial vessel with computational methods. The Arbitrary Lagrangian Eulerian (ALE) approach is a well known method to describe FSI, and it is an algorithm supported by most commercial numerical codes for implementing Fluid Structure Interaction. The concept of ALE is discussed in the next section.

4.1.1 Arbitrary Lagrangian Eulerian (ALE) method

Elements of continuum can be described by mainly two algorithms. One is Lagrangian algorithm in which the computational grid and the material points coincide in the continuum and this coincidence is not broken even if the configuration of the domain changes by internal or external forces. This approach to describe the deformation of the domain has the advantage of easily tracking the movement of the material particles. Thus, the Lagrangian algorithm is mainly used to explain the structural mechanical response. However, the coincidence of mesh and associated material particle prevents the ability to describe the material particle movement when it experiences large deformation because the associated computational grid is distorted, causing computational errors. In contrast, in the other algorithm for describing material properties, called the "Eulerian algorithm", the computational mesh is fixed and the material points move freely with respect to this mesh. For this reason it is capable of handling large distortions in the continuum. This algorithm is mainly used in fluid mechanics in which the recirculation or vortex of fluid particles can be observed, and these flow patterns cannot be described with a Lagrangian approach. Because fluid particles can be described with respect to the fixed computational grid in Eulerian algorithms, it is usually necessary to define precise boundaries and a high resolution mesh to capture flow pattern details. In the purely Eulerian approach, numerical

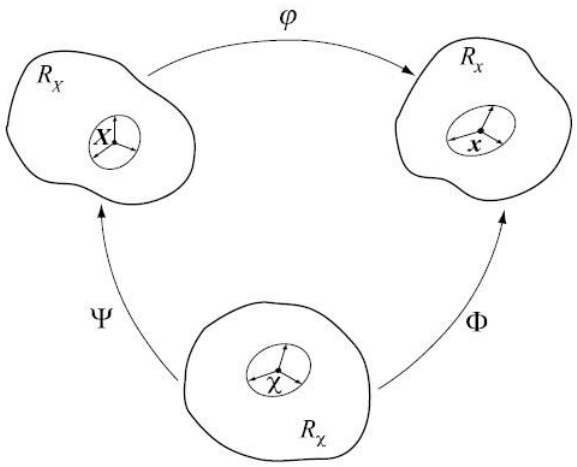

Figure 36: A third domain for ALE motion description (R_χ) [28]. R_X is a reference configuration and R_x is a spatial coordinates.

problems occur when the boundary of the fluid domain moves or deforms with time because the fluid particle properties are calculated with respect to the computational grid; however, these meshes are moving so that the fluid properties should include the effects of a moving mesh. However, the purely Eulerian algorithm cannot handle the moving mesh effect. The limitations of pure Lagrangian or Eulerian algorithms argue for a hybrid formulation in which the best features of each algorithm are combined and enhanced to overcome each algorithm's drawbacks. This hybrid formulation is called, the Arbitrary Lagrangian Eulerian (ALE) method.

In Fig. 36, X represents the material coordinates and helps us identify the reference configuration, R_X. Through the one-to-one mapping (φ) from material coordinates to spatial coordinates (R_x) the velocity of material points v is defined in two ways as explained above. In the case of material points coinciding with associated computational grids during the deformation, there are no convective effects due to the separation between the material points and the mesh nodes. Thus, in the Lagrangian algorithm, the inverse mapping allows it to track the previous configuration of material points defined as; $v(X,t) = \frac{\partial x}{\partial t}\Big|_X$ with $\frac{\partial}{\partial t}\Big|_X$ meaning the time derivative in

Lagrangian coordinates. On the other hand, in the Eulerian algorithm, the variables and material properties at the computational mesh node at the considered time t are related with material particles passing through the fixed mesh region of space. Thus, it is relatively easy to describe fluid particles in spatial coordinates x and time t, and the velocity v can be defined as; $v = v(x, t)$.

It is necessary to set up a third domain for ALE motion description because neither purely Lagrangian nor Eulerian coordinate can handle large deformations of the continuum with moving boundaries. The ALE domain is referred to as the referential configuration R_χ, where χ represents the computational grid points (Fig. 36). Using the mapping (Φ) from reference coordinates to spatial coordinates the mesh velocity $\hat{v}$ can be defined as; $\hat{v} = \frac{\partial x}{\partial t}\Big|_\chi$ representing the computational grid motion in the spatial domain. With the ALE domain and the mapping correlations between each domain the convective velocity c between the material velocity v and grid points velocity $\hat{v}$ can be defined as: $c = v - \hat{v}$. Finally, based on the kinematic concept in the ALE domain the mass conservation and the momentum governing equation are expressed as follows [28, 105]:

$$\frac{\partial \rho_{blood}}{\partial t}\Big|_\chi + c \cdot \nabla \rho_{blood} + \rho_{blood} \nabla \cdot v = 0 \tag{12}$$

$$\rho_{blood}\left(\frac{\partial v}{\partial t}\Big|_\chi + (c \cdot \nabla)v\right) = \nabla \cdot \sigma + \rho_{blood} g \tag{13}$$

Where, $\frac{\partial v}{\partial t}\Big|_\chi$ is a time derivative in the ALE domain and g is a gravitational acceleration. In general, the fluid density in the blood flow simulation is treated as constant so that Eqn. (12) can be simplified to Eqn. (2), which is the well known incompressible equation. Eqn. (13) represents Navier-Stokes Equation in the ALE domain and through comparison with the Navier-Stokes Equation in the purely Eulerian domain, Eqn. (1), the ALE form of Navier-Stokes Equation can handle the grid point velocity, giving a good advantage and making it able to handle the

fluid flow calculation in Fluid Structure Interaction. More detailed procedure and explanations about ALE method can be referred to Donea J et al. [28].

To get the mesh velocity it is necessary for the fluid domain mesh to be updated to assign computational node displacement and velocity at each time step of simulation. For this reason it is essential to apply a numerically robust remesh algorithm. In the fluid structure interaction, the mesh nodes in the solid domain are in general moved based on the Lagrangian algorithm, however, the mesh topology in fluid domain must be updated or remeshed to get the mesh point velocity with the deformation of the interaction between blood and arterial wall. Several remesh algorithms have been suggested, but in the ALE approach mesh smoothing methods are well known to improve the element shape when the domain topology is set up. With smoothing methods the connection between nodes is treated as a spring with pseudo-stiffness, and the severe distortion of the mesh at local areas due to deformation of the interaction is reduced by distributing the amount of distortion through the whole mesh connection. This procedure usually prevents severe mesh distortion that causes the numerical errors. In fact, mesh smoothing approaches do not consume as much computational resources compared with other remesh methods, and this can be applied to any kind of mesh shape in 2D and 3D. For this reason a smoothing method is adapted by most commercial CFD codes, i.e, Fluent, CFX and Comsol.

4.1.2 Interface condition

To ensure the fluid mesh grid will not detach or overlap into the solid domain during the motion it is necessary to set up an extra compatibility condition on interface surface. It is obvious that the node on the surfaces should have a equal displacement value. This geometrical compatibility condition can be expressed in numerical computation as shown by Eqn. (14), where n_s and n_f are the normal unit vector to the interface in fluid and solid domain respectively, and d_f is the surface node

displacement which belongs to the fluid domain, and d_s is the surface node displacement which belongs to the solid domain. With the updated mesh topology in the fluid domain the total stress in the fluid should be equal to the solid domain due to the geometrical compatibility condition. This can be assigned by an equilibrium condition which is defined as follows:

$$n_f \cdot d_f = n_f \cdot d_s$$
$$\sigma^f_{total} \cdot n_f = -\sigma^s_{total} \cdot n_s \tag{14}$$

where σ^s_{total} is the total stress acting on the structure.

Because of the physical features of fluid and structure and the related numerical method, the resolution and element type of meshes differ in each domain, thus the mesh topology and spatial distribution of mesh points are not the same in many cases of FSI simulation. This means that it is not necessary for mesh grid points to coincide on the interface surface between the lumen and arterial wall. However, to transfer solution variable data, i.e., the mesh displacement and the force across such an interface surface, an interpolation procedure is essential. The surface interpolation is done by a mapping procedure in which variable data on each fluid node are mapped to nearby solid mesh nodes when the force is transferred to the solid domain as a boundary condition. Also, data on each solid node are mapped to nearby fluid mesh nodes when the interaction geometry is deformed, and it needs to be updated to serve the fluid domain [31]. If the arterial wall deformation is relatively small and the initial surface mesh topology is to be maintained during the calculation, the surface mapping procedure needs to be carried out once at the beginning of the simulation, and this saves computational resources and calculation time.

4.1.3 Artificial added mass instability

In computational research on FSI, several coupling methods have been established to accomplish fully two-way interaction between fluid motion and solid structure. The

first suggested method is a direct coupling approach which can solve the fluid and structure governing equations simultaneously at each iteration of the calculation [7]. In this method, equilibrium on the interaction surface is enforced through the finite element integration process. This approach is convenient, accurate and robust numerically among the coupling methods if it is set up with proper initial and boundaries at the start of calculation. However, as expected, since the whole mesh in the fluid and solid domains is processed at the same time, it demands more computer hardware resources and it takes more time to finish the calculation if not all discretized meshes are loaded on the memory. Another approach is the iterative coupling method which decouples the calculation of the fluid flow and structure mechanics [51, 108]. At each time step the fluid properties are calculated based on the current blood vessel shape and the pressure of fluid is applied across the interface surface of arterial wall as a loading to the structure. The response of the blood vessel wall to the pressure force is calculated with elastostatic structure theory, and then the final structure configuration is updated as the next fluid domain moves through the interface condition. The major advantage of iterative coupling is that we can use the most advanced developed CFD and CSM (computational structure method) codes in each fluid and solid domain because the numerical calculation at each domain can be separated.

In FSI simulation with the ALE algorithm it is critical that CFD needs to be able to handle the remesh associated with the boundary motion. Fluent or CFX is a highly specialized CFD code and has all needed functions coupling the structural mechanics. The structure mechanical code also must be able to handle the elastic compliant structure with various external boundary conditions. Ansys or Abaqus has been verified to be able to do the structural calculation in various areas. However, to accomplish fully two-way FSI simulation, a coupling program between CFD and CSM is needed to interpolate data across the interaction surface. A coupling program, i.e., MpCCI (Mesh based parallel code coupling interface) which has been developed

by the Fraunhofer Institute for Algorithms and Scientific Computing (SCAI) [75] has been released in order to provide an application-independent interpolation for coupling different simulation codes. But the default coupling between CFD and CSM by MpCCI can handle FSI modeling without numerical instability and errors only in the case that there is a huge difference between the fluid and solid density. For example, the FSI simulation of airplane wing vibration by the wind could be solved by above default coupling; however, the interaction between blood flow and the elastic arterial wall in which their densities are very similar cannot be accomplished with this coupling method. Due to the intrinsic deficiency of the iterative coupling method, it is hard to improve numerical stability even with decreasing the coupling time step between two codes. This problem is called artificial added mass instability [17, 33]. During the calculation it looks like there is a oscillation of the fluid domain if the overall geometry is updated from the solid domain deformation at each coupling step. This oscillation often does not converge, and finally the FSI calculation stops with numerical errors. The oscillation pattern gives the above name to this numerical instability because it seems that extra mass is acting on the fluid domain and prevents convergence to the desired domain position.

Several schemes have been developed to solve this phenomenon. But in most codes for solving multidisciplinary simulation, i.e., ADINA, MSC.Dytran, ANSYS multi-physics, and CFD-RC, an under-relaxation algorithm is introduced to give a relaxation factor to prevent the oscillation and aid in convergence to desired shape. The actual computed displacements x_i^{act} are linearly weighted with the value, α_{under}, from the proceeding iteration (x_i^{old}) to give the new displacement x_i^{NEW} ;

$$x_i^{NEW} = \alpha_{under} x_i^{act} + (1 - \alpha_{under}) x_i^{old} \tag{15}$$

Where α_{under} is the relaxation parameter which is determined from the numerical situation considering the physical environment. At the initial trial, this value starts from 1 and gradually is reduced to find the proper value which solves the displacement

oscillation. In our research, this value is in the range from $0.5 \sim 0.7$ in Ansys multiphysics using a staggering iterative method. The under-relaxation does not change the final converged result, it only influences the stability of the coupling process numerically.

Two commercial codes are used to accomplish FSI numerical modeling of all subjects in this research. The direct method, in which the coupling procedure is not necessary and there is no need to be concerned about artificial added mass instability, is implemented with Comsol (Boston, USA), and staggering iterative method is accomplished with Ansys multiphysics, which consists of CFX (Fluid solver), Ansys mechanical (Structural solver) and its own coupling program.

In both approaches the basic setting is common. Blood is treated as a Newtonian and incompressible fluid. The free traction boundary condition at CCA inlet is replaced by the pressure value which was set up in Section **2.2.3** (Fourier Series to curve fitting) to give the pressure force and cause arterial wall deformation. Mass flow rates are assigned at ICA/ECA. In previous studies of the carotid artery, it was found that the blood vessel is not homogeneous and the mechanical response to the external force is not linear at high strain. However, with rescaled pressure (RP), which is explained in detail in Section **4.2.2**, the geometrical nonlinearity effect is not significant in this physiological stress range. Also, there is a lack of information about subject specific structural properties, and we simplify the numerical calculation by assuming the arterial wall is a homogeneous, isotropic and linear elastic material with Poisson′s ratio of 0.48. In general, the Young′s modulus of human carotid arteries is between $0.3MPa$ to $0.5MPa$ depending on the age and state of arteriosclerosis [106]. All subjects in our research had a different age and degree of arteriosclerosis, so we took the approach of using a representative value of Young's modulus for each subject. The direct measurement of the dilation in carotid arteries from 126 patients by Ramnarine et al. [70] was used to determine the Young′s modulus. The dilation

of the arterial wall reaches up to $0.8mm$ at the bifurcation of the normal arteries. Thus, if the peak value of structural deformation of the subject is at this value, the Young's modulus at this time is assigned to the subject. For this method, the Young$'$ modulus of subject 1 is assigned to $0.4MPa$, $0.3MPa$ to subject 2 and $0.5MPa$ to subject 3. The ends of the CCA and ICA/ECA are fully constrained, i.e., the x,y and z coordinates of the mesh points on the cross section are fixed. The time step in the pulsatile calculation is set as $0.01s$ in both approaches.

In Comsol, the N-S equations, structural mechanics and ALE moving mesh are solved simultaneously with a fully coupled nonlinear solver to get the final results at each time. In constrast, in Ansys multiphysics, CFX is first calculated with the initial boundary domain, the coupling step is done with the under relaxation method and the structure is computed with structural governing equations. If all solvers satisfy the convergence condition at each time step, computation progresses to the next time point.

4.2 Matching the boundary conditions in vivo

The in-vivo geometry represents a carotid artery under physiological pressure loadings, so that the artery is not in a zero mechanical stress and strain state. However, when the geometry is developed from MR images, it does not have any stress. Thus, it is necessary to compensate so that the artery after image processing has a representative in-vivo mechanical stress and strain. One approach is to shrink the geometry to a state such that when loaded with physiologic pressure, it returns to coincide with the in-vivo MRI image.

4.2.1 Shrinkage of the artery

4.2.1.1 Shrinkage ratio

An in-vivo artery shrinks if it dissected from the surrounding tissue and removed from the body. Comparison between in-vivo MR images and ex vivo MR images

makes it possible to determine the shrinkage ratio in the radial direction and inner circumferential direction. Such a study was done by Huang et al. [41]. They set up two geometries from in-vivo MR images and ex vivo MR images from 10 patients and compared these. They found that the average shrinkage ratios were 25% in axial and 7.9% in inner circumferential direction, respectively.

To accomplish the shrinkage in the axial direction, z coordinates of each point on the inner wall and outer wall were reduced by the reported axial shrinkage ratio, referenced to the inlet of the common carotid artery. The x and y coordinates of each point on the inner wall were shrunk by the reported inner circumferential ratio. Although the artery is shrunk, the total arterial volume needs to be maintained from the initial geometry. Thus, the outer wall circumferential shrinkage ratio was calculated based on mass conservation. The volume calculation and the shrinkage process was done using Matlab. It should be considered that the wall thickness ratio between inner wall and outer wall is maintained even though the artery is shrunk. However, it was found that the relative position of inner wall and outer wall was distorted due to one-way movement of the shrunk inner wall when the inner circumferential shrinkage ratio was applied to reduce the inner wall without reference points (at the outlet of ICA of subject 1 in Fig. 83 (a)). As a consequence, the wall thickness between moved shrunk inner wall and the outer wall was reduced and the other side of arterial wall was increased. To overcome the artery distortion due to the movement of the inner wall by the shrinkage process, reference points must be set to shrink the artery and keep the wall thickness ratio. The centerline of the inner wall surface can be used as the reference points and the detailed procedure to obtain the centerline of each subject with VMTK program which has been developed by Lucas et al. [1] is explained in an Appendix. When the shrinkage happened in inner wall and expansion in the outer wall based on the centerline of the artery, the relative distance between inner wall and outer wall is maintained after the shrinkage

process was applied (Fig. 83 (b)). The final arterial model is presented in Figs. 37 $\sim$ 39. In each figure the upper diagram shows that centerline of the carotid artery and the in-vivo geometry, and in the lower two diagrams the in-vivo geometry and the shrunk model are overlapped and compared to demonstrate how the shrinkage process influences the geometrical deformation.

4.2.1.2 Limitation of the arterial shrinkage approach

The main reason to shrink the in-vivo artery is so that when the shrunk geometry is stretched, the stretched geometry matches the in-vivo artery and has a reasonable initial stress and strain. However, when all subjects in our research were stretched to recover in-vivo geometry, it was found that severe geometrical distortion happened at the fixed boundary condition in the radial direction at CCA and ICA/ECA. Most of all, the geometrical non-planarity between CCA and ICA/ECA and the tortuous curvature of ICA, both of which give more complex flow patterns in the ICA and the carotid bulb, are almost gone in Fig. 40. When the ICA/ECA outlet wall was stretched in the axial direction by 25%, the x and y coordinates on the boundary condition were set to keep the original coordinates, and this prevents deformation in the radial direction on the ICA/ECA outlet wall. This boundary setting results in the shrunk geometry being deformed only in the axial direction. However, when they were stretched axially with these settings, the geometrical distortion happened at the end of the ICA/ECA which was not seen in the shrunk process. This distortion occurs due to mass conservation and the Poisson′ ratio of the structure (Fig. 40). In this calculation the fully fixed constraint was applied at the CCA inlet because this gave the numerical stability and also prevented arbitrary motion of the artery. But this fully constrained condition leads to the geometrical distortion at the end of CCA, similarly to the end of ICA/ECA. To eliminate geometrical distortion at the ends of ICA/ECA, the x and y coordinates of this region were allowed to move freely

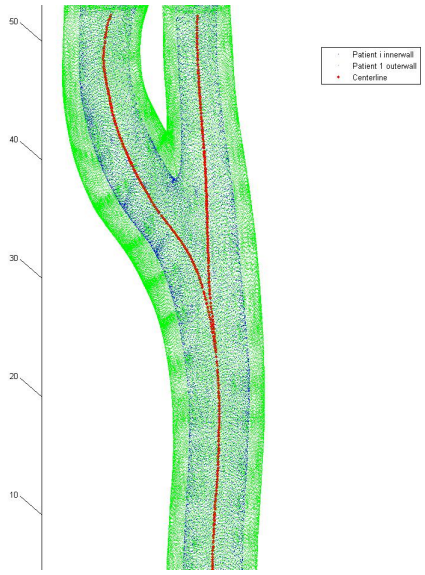

(a) The Centerline and In Vivo Geometry of subject 1 in the Posterior View

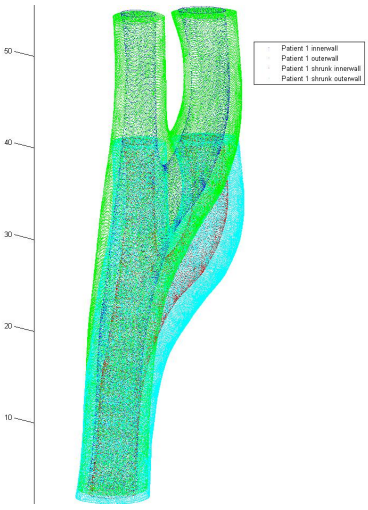

(b) In Vivo and Shrunk Artery of subject 1 in the Anterior View

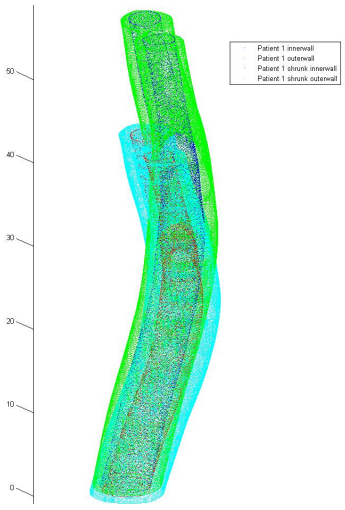

(c) In Vivo and Shrunk Artery of subject 1 in the Lateral View

Figure 37: Subject 1

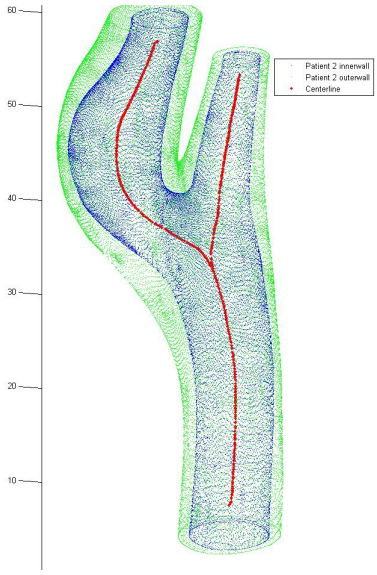

(a) The Centerline and In Vivo Geometry of subject 2 in the Posterior View

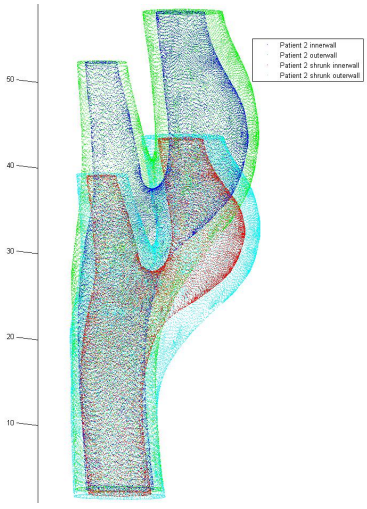

(b) In Vivo and Shrunk Artery of subject 2 in the Anterior View

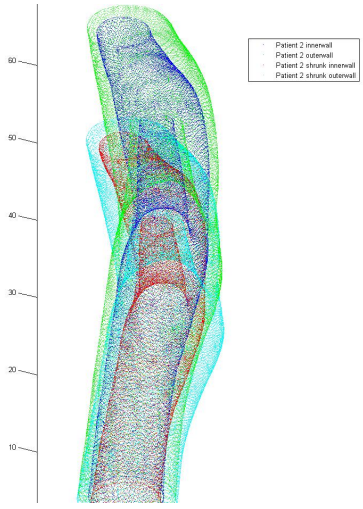

(c) In Vivo and Shrunk Artery of subject 2 in the Lateral View

Figure 38: Subject 2

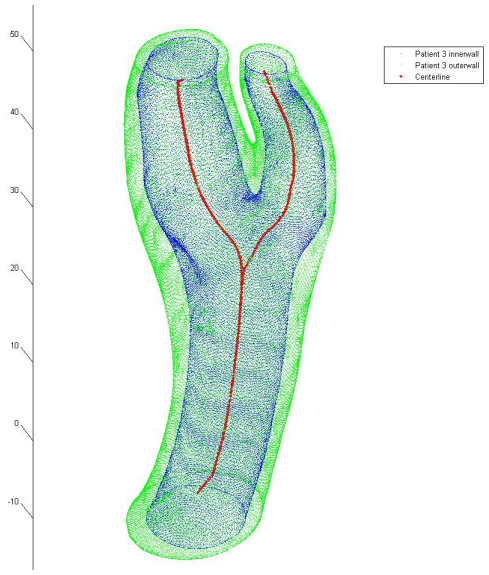

(a) The Centerline and In Vivo Geometry of subject 3 in the Posterior View

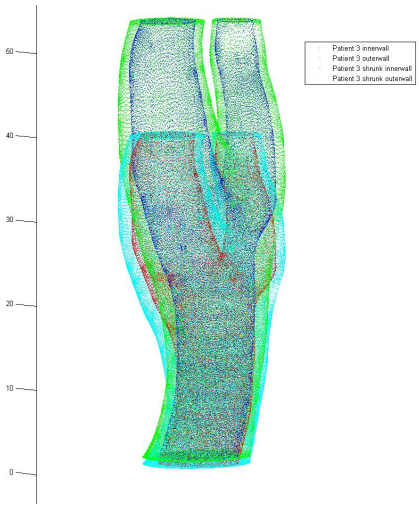

(b) In Vivo and Shrunk Artery of subject 3 in the Anterior View

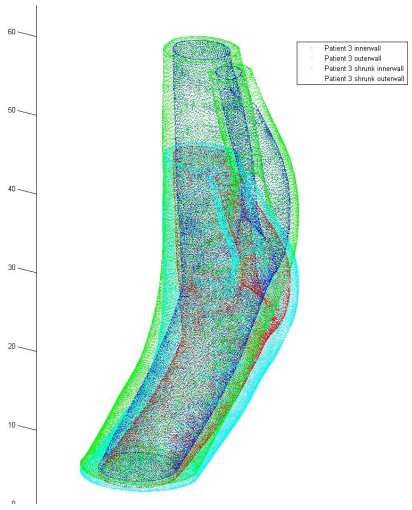

(c) In Vivo and Shrunk Artery of subject 3 in the Lateral View

Figure 39: Subject 3

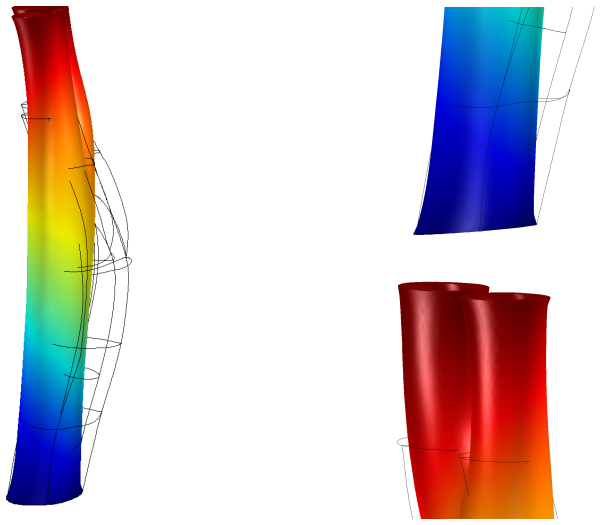

Figure 40: The distortion of stretched artery in subject 1

in the radial direction based on the structure calculation. In this case the geometrical distortion was gone at the end of outlet but the geometrical non-planarity in the in-vivo artery totally disappeared (Fig. 41). Without the constraint of x and y coordinates at the end of ICA/ECA, the structure tends to change to minimize the stress caused by the deformation of the artery. This makes the artery deform to be more nearly straight than the previous case.

In the research by Huang et al. [41], the final geometry in the FSI simulation had a small length of around $2cm$, with the bifurcation apex as the middle of geometrical model. This small geometry did not have geometrical non-planarity between the CCA and ICA/ECA. Thus, they could apply 25% axial elongation without much geometrical distortion. In another study by Gao et al. [34] a small axial stretch ratio (10%) was applied to give an initial stress and strain. This small stretch ratio also helped to reduce the in-vivo geometrical distortion, but still there is a difference between the in-vivo artery and stretched artery with initial diastole pressure. A common theme in the above studies was that they looked for the mechanical stress itself on and around the plaque in the carotid bulb. The shrinkage process is critical in their research despite the sacrifice of the in-vivo geometry at the diastole. In our

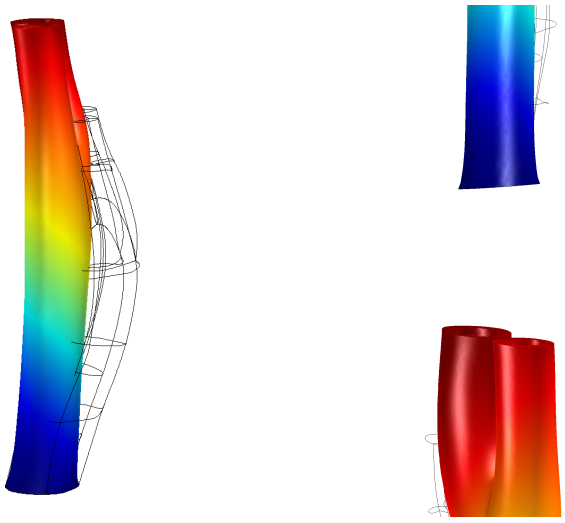

Figure 41: The distortion of stretched artery in subject 1 with xy free movement

research, determining the structural stress of the arterial wall is not a concerning factor. Rather, the strain of the arterial wall and the blood flow field based on in-vivo geometry are the main factors to extract from FSI modeling. For this reason, if the dilation of the artery matches with the average deformation of carotid artery, it is not necessary to apply the shrinkage process to give a physiological initial structural stress. However, if it is critical to get the mechanical stress itself of the artery, a more developed approach based on the shrinkage process is needed in future research.

4.2.2 Rescaling pressure range

Without the shrinkage process it is still necessary to match the beginning of the FSI simulation between the physiological pressure and the in-vivo geometry. In our research the arterial wall is treated as an elastic homogeneous material, thus the displacement of the blood vessel wall changes linearly with intraluminal pressure which comes from blood flow. Thus, if FSI simulation with an image processed in-vivo artery at diastole starts with the physiological diastole pressure ($83mmHg$) the arterial wall is dilated from $0mmHg$ to $83mmHg$ first and based on this initial expansion the arterial wall alternates periodically with the pulsatility of the heart beat. To overcome this drawback it is necessary to reduce the physiological pressure

range from $83mmHg \sim 152mmHg$ to $5mmHg \sim 74mmHg$. The difference between the minimum and the maximum physiological pressure (PP) is retained but the range is reduced to match the initial pressure to the image processed in-vivo artery at diastole. The main reason to set $5mmHg$ as the beginning of CCA pressure in the rescaled pressure range is to stabilize the numerical calculation because in the flow calculation, if $0mmHg$ is applied at the CCA inlet and the volume flow rate at the ICA/ECA, the outlet pressure must be below $0mmHg$ by Navier-Stokes equation and this negative pressure can cause numerical divergence during FSI calculation. To avoid negative pressure at the outlets and at the same time not to cause the geometrical deformation, $5mmHg$ is chosen as the initial pressure in the rescaled pressure range.

The increase of domain volume to hold the fluid reduces the velocity in the artery, due to mass conservation. This also can strengthen the justification of the rescaled pressure (RP) application. As can be expected, the volume of the artery which is dilated by physiological pressure has a larger capacity than the volume dilated by rescaled pressure due to the extra dilation by the initial physiological diastole pressure. The results of this comparison are shown in Figs. $42 \sim 46$. In each figure, the time point when the velocity pattern was extracted in the cardiac cycle is seen in the upper left diagram; and in the upper right, the PC MR contour represents the flow distribution at the cross section below $10mm$ proximal to the apex. The results of FSI with physiological pressure are shown in the lower left, and in the lower right the results from rescaled pressure are presented. Both are extracted from the cross section $10mm$ proximal to the bifurcation apex to match PC MR data. In the physiological pressure case the in-vivo artery is already dilated by the initial diastolic pressure, thus the total volume of the lumen is larger than the rescaled case. For this reason the maximum velocity in each time point is lower than the velocity from the rescaled pressure. At the beginning of systole (BS) the maximum velocity of PP is $10.84cm/s$

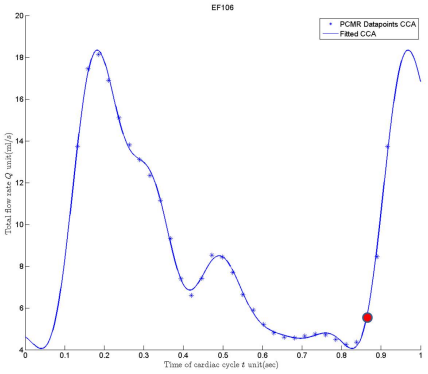

(a) Time points (BS, the Beginning of the Systole)

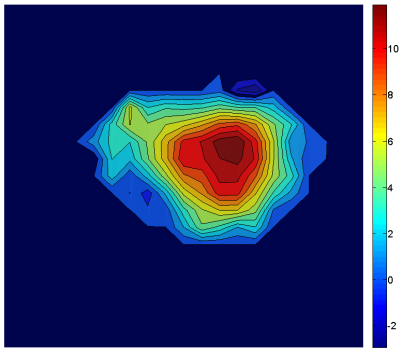

(b) PC MRI

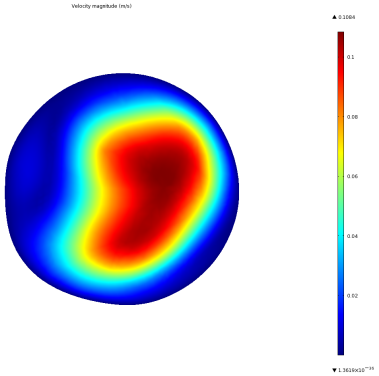

(c) Physiological Pressure (PP)

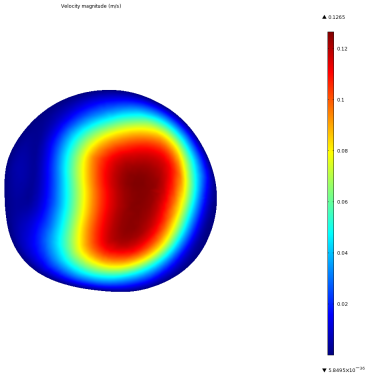

(d) Rescaled Pressure (RP)

Figure 42: Comparison between Physiological Pressure (PP) FSI and Rescaled Pressure (RP) FSI at the Beginning of Systole (BS) in subject 2

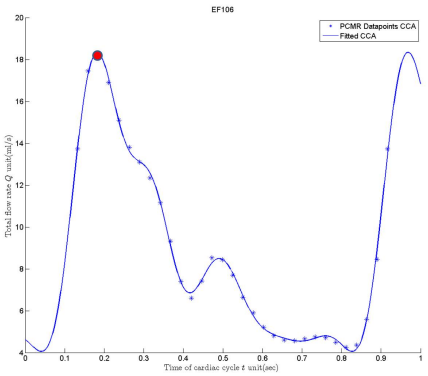

(a) Time points (PS, the Peak of the Systole)

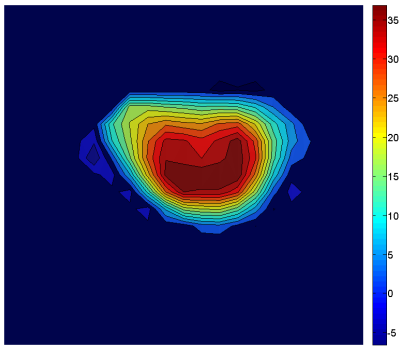

(b) PC MRI

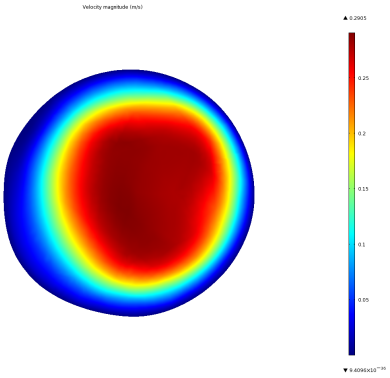

(c) Physiological Pressure (PP)

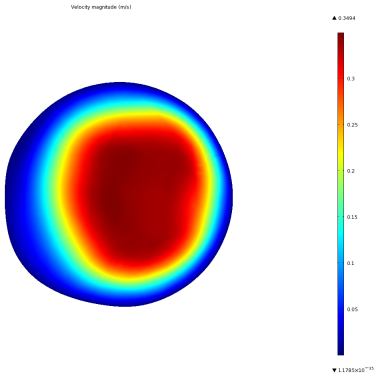

(d) Rescaled Pressure (RP)

Figure 43: Comparison between Physiological Pressure (PP) FSI and Rescaled Pressure (RP) FSI at the Peak of Systole (PS) in subject 2

and the maximum velocity of RP is $12.65cm/s$. The maximum velocity of PC MR is very similar to RP results by $12.5cm/s$. This trend is present at all time points (Figs. $42 \sim 46$). At the peak of systole (PS) the difference of maximum velocity is more evident. The peak value of the velocity of PC MR is around $35cm/s$, and this value is very similar to the maximum velocity in the RP ($34.94cm/s$); however, the maximum velocity in the PP reaches at most $29.05cm/s$. There is a gap of $5cm/s$ between PC MR and PP cases because at this time point the in-vivo artery is maximally deformed by the highest pressure in a cardiac cycle. Thus, the maximum increase of the volume to hold the fluid reduces the velocity to a lower value.

The comparison of the velocity profile at the cross section between PP and RP also

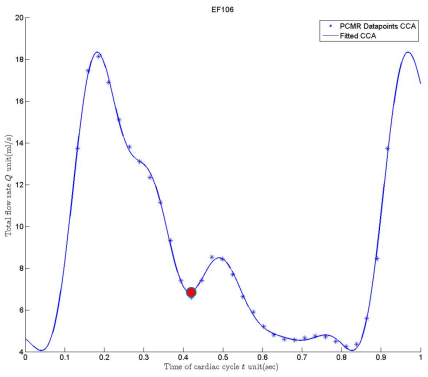

(a) Time points (BAD, the Beginning of the Acceleration in the Diastole)

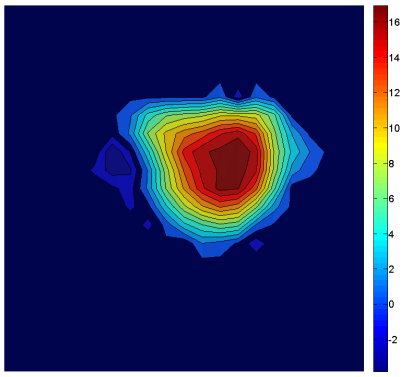

(b) PC MRI

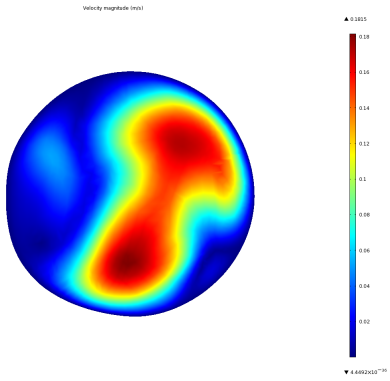

(c) Physiological Pressure (PP)

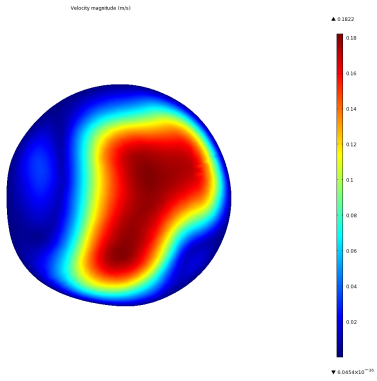

(d) Rescaled Pressure (RP)

Figure 44: Comparison between Physiological Pressure (PP) FSI and Rescaled Pressure (RP) FSI at the Beginning of Acceleration in Diastole (BAD) in subject 2

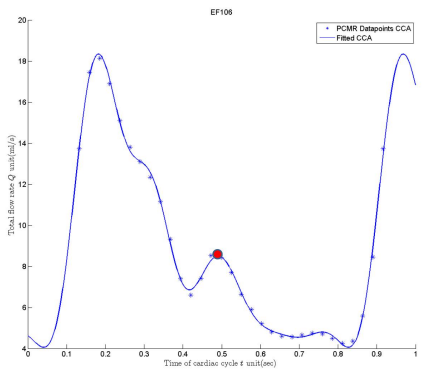

(a) Time points (PD, the Peak of the Diastole)

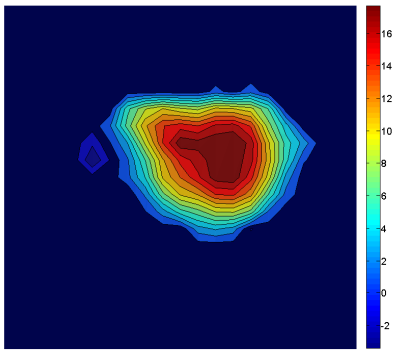

(b) PC MRI

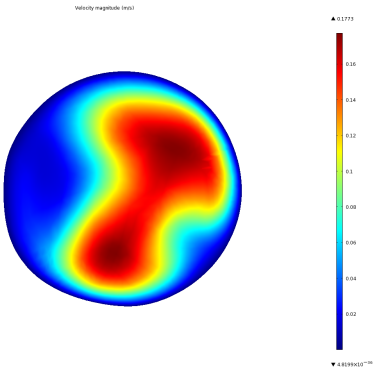

(c) Physiological Pressure (PP)

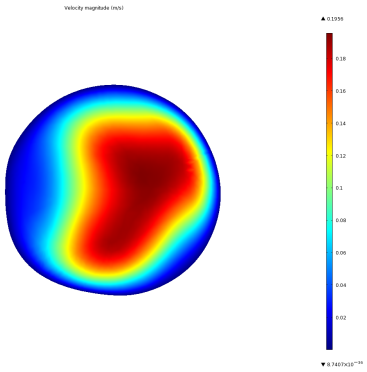

(d) Rescaled Pressure (RP)

Figure 45: Comparison between Physiological Pressure (PP) FSI and Rescaled Pressure (RP) FSI at the Peak of Diastole (PD) in subject 2

supports the justification of RP application. In general, PC MR supplies the velocity pattern at the cross section; however, it is not enough to be used for segmentation of the carotid artery. Steinman et al. [85] compared the results from CFD and PC MR data. At each time point the core region around the maximum velocity shows a similar flow pattern. However, away from the core region and approaching the arterial wall the CFD flow pattern did not follow the same pattern of PC MR exactly. The deviation was maximized when PC MR were acquired at the bifurcation apex. At this location, delineation of the outline of the artery is vague, due to poor resolution of PC MR data by comparison to the CFD results at this region of complex flow patterns and large movement of arterial wall. The comparison between PC MR and

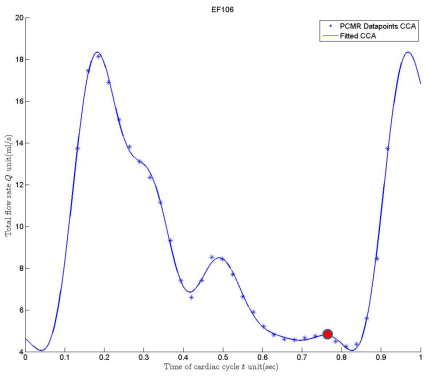

(a) Time points (MD, the Minimum flow in the Diastole)

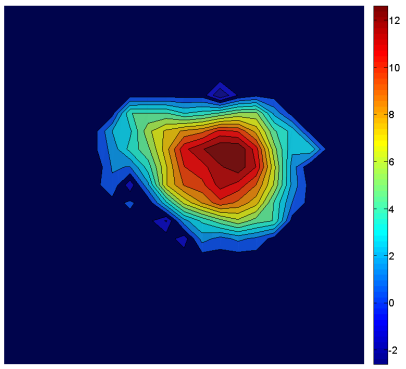

(b) PC MRI

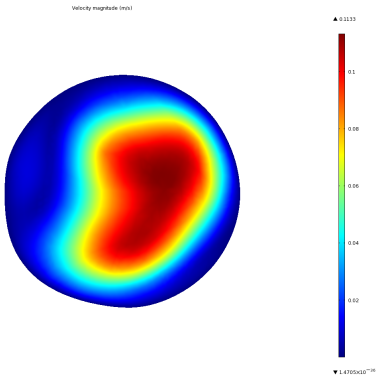

(c) Physiological Pressure(PP)

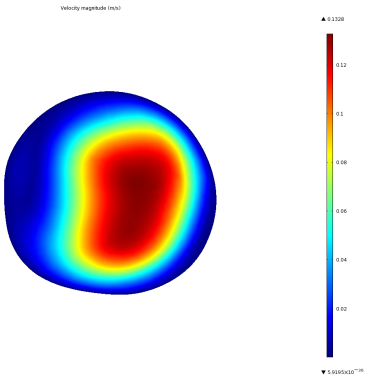

(d) Rescaled Pressure (RP)

Figure 46: Comparison between Physiological Pressure (PP) FSI and Rescaled Pressure (RP) FSI at Minimum flow in Diastole (MD) in subject 2

the result from FSI modeling in our research subjects also follows this trend. The core region around the maximum velocity at each case is similar to the numerical calculation but does not match all flow patterns over the cross section. On the other hand, results from the rescaled pressure case are more similar to PC MR data at all time points, especially at the beginning of acceleration in diastole (BAD) and at the peak of diastole (PD) in Figs. 44 and 45.

In our research, due to the geometrical distortion by stretching and the mismatch of peak value and pattern of velocity by extra dilation caused by initial physiological pressure, the rescaled pressure approach was applied at the CCA inlet to give proper geometrical deformation with the boundary condition in which the movement of the surface of CCA and ICA/ECA was fully constrained.

4.3 Results and Discussion

It is necessary to set up the boundary layer to detect shear rate on the surface more accurately. For this reason this layer is divided into four grid layers on the lumen surface, and the remaining parts of the flow domain were meshed with tetrahedral elements by $79,000$ in subject 1, $255,000$ in subject 2 and $191,000$ in subject 3. To determine the size of grids in the flow domain, blood flow was calculated with the N-S equations without coupling the arterial wall and the final size was set up when the maximum value of each hemodynamic factor did not change more than 1%. The mesh size for the arterial wall also was determined in a similar way, in which wall structure was calculated without coupling with the blood flow. The final mesh size is $146,000$ in subject 1, $282,000$ in subject 2 and $209,000$ in subject 3, when the change of structural parameters including the displacement, mechanical stress and strain are less than 1%. A fully two-way coupled FSI model was calculated during three periods of the cardiac cycle, and the last period was chosen to visualize the complete data set.

4.3.1 Dilation of carotid artery

The distensibility of the arterial wall of each subject is analyzed by comparing the displacement at maximum and minimum pressures. In Figs. 47 $\sim$ 49, the upper

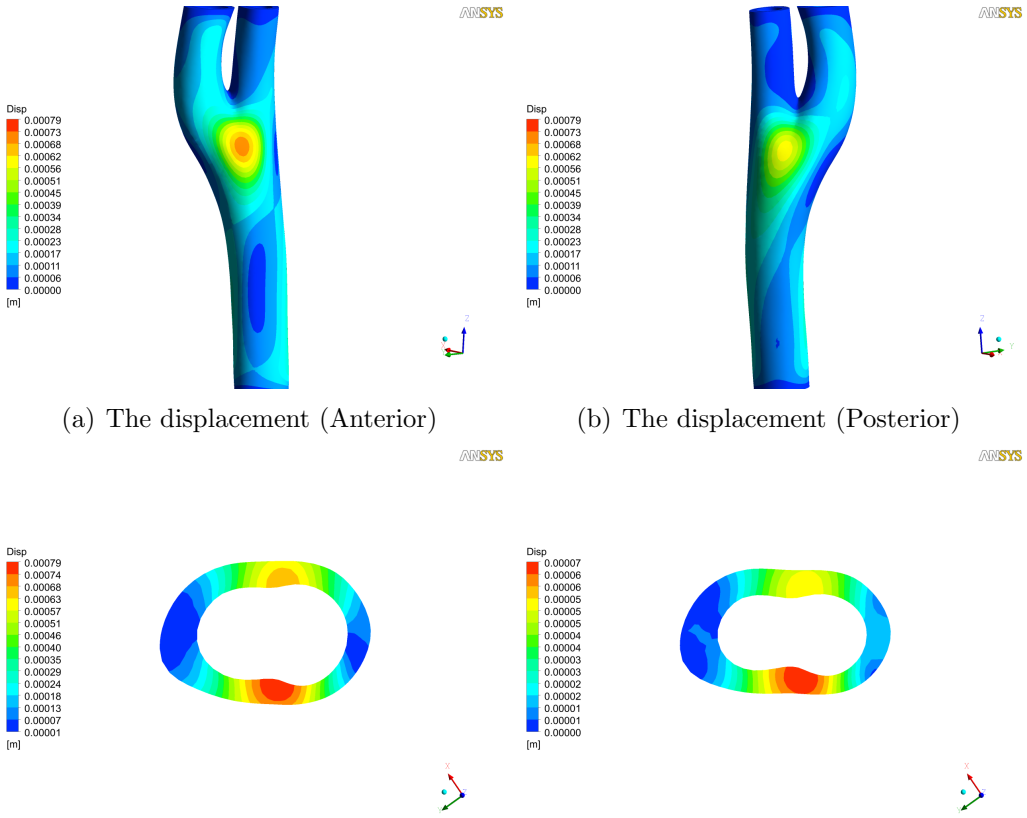

(a) The displacement (Anterior) (b) The displacement (Posterior)

(c) Cross section at maximum pressure (d) Cross section at minimum pressure

Figure 47: The dilation at the maximum pressure in subject 1

diagrams represent the displacement of the subjects in an anterior view and posterior view, and in the lower diagrams the cross section of arterial wall at the site of maximum displacement is exhibited to exclude lateral movement and to visualize only the dilation. The geometry of subject 1 is simple compared to other subjects in our research. The wall thickness is relatively uniform over the carotid artery, and the curvature is not dominant in the connection between CCA and ICA/ECA. Most of all, there is no tortuous curvature in the ICA. For this reason the lateral displacement is not evident in this subject. The maximum displacement happens around the

bifurcation junction between the CCA and ICA/ECA (Fig. 47 (a)).

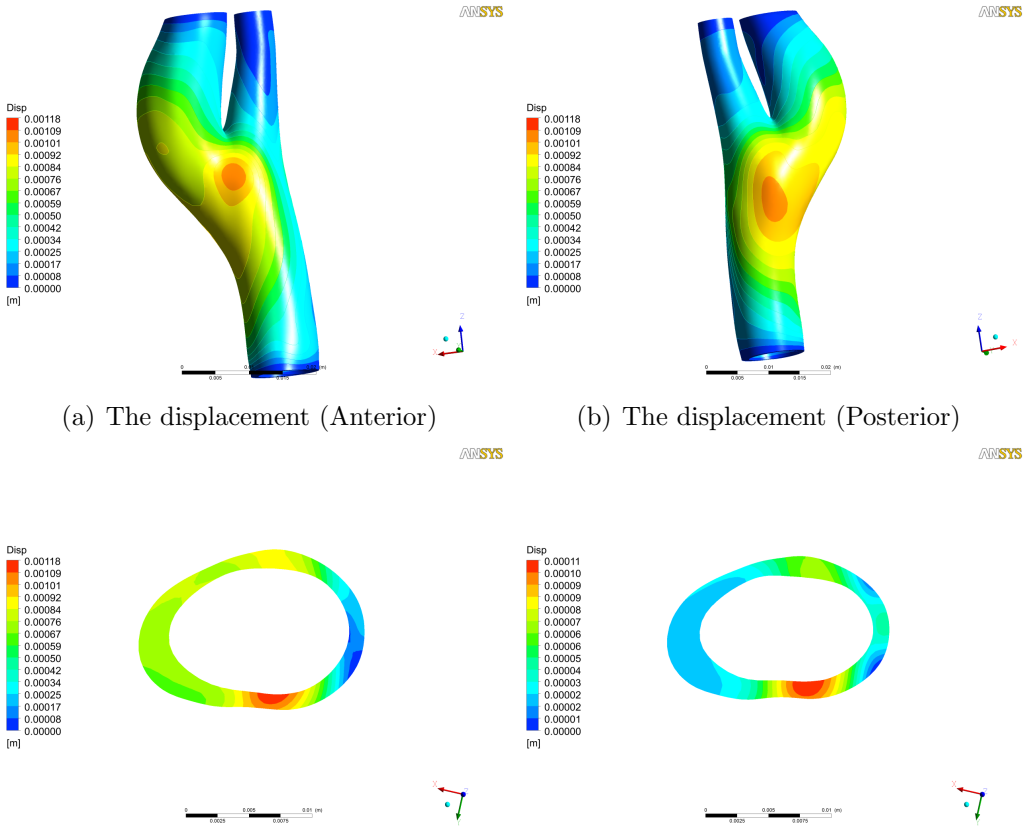

(a) The displacement (Anterior)

(b) The displacement (Posterior)

(c) Cross section at maximum pressure

(d) Cross section at minimum pressure

Figure 48: The dilation at the maximum pressure in subject 2

In subject 2, the irregular in-vivo geometrical features including mild curvature in the CCA and tortuous curvature in the ICA make the lateral movement to the left side of the carotid artery. This can be seen in upper diagram of Fig. 48. Higher displacement is dominant in the carotid bulb. This can be caused by the strong asymmetry of the flow pattern due to the tortuous curvature of ICA and the mild stenosis at the beginning of bifurcation and proximal ICA. Maximum displacement is exhibited around the middle of the connection between CCA and ICA/ECA on the anterior and posterior side.

Consistent with the previous subject 2, there is a curvature between CCA and ICA/ECA in subject 3. However, tortuous curvature is present not in the ICA but

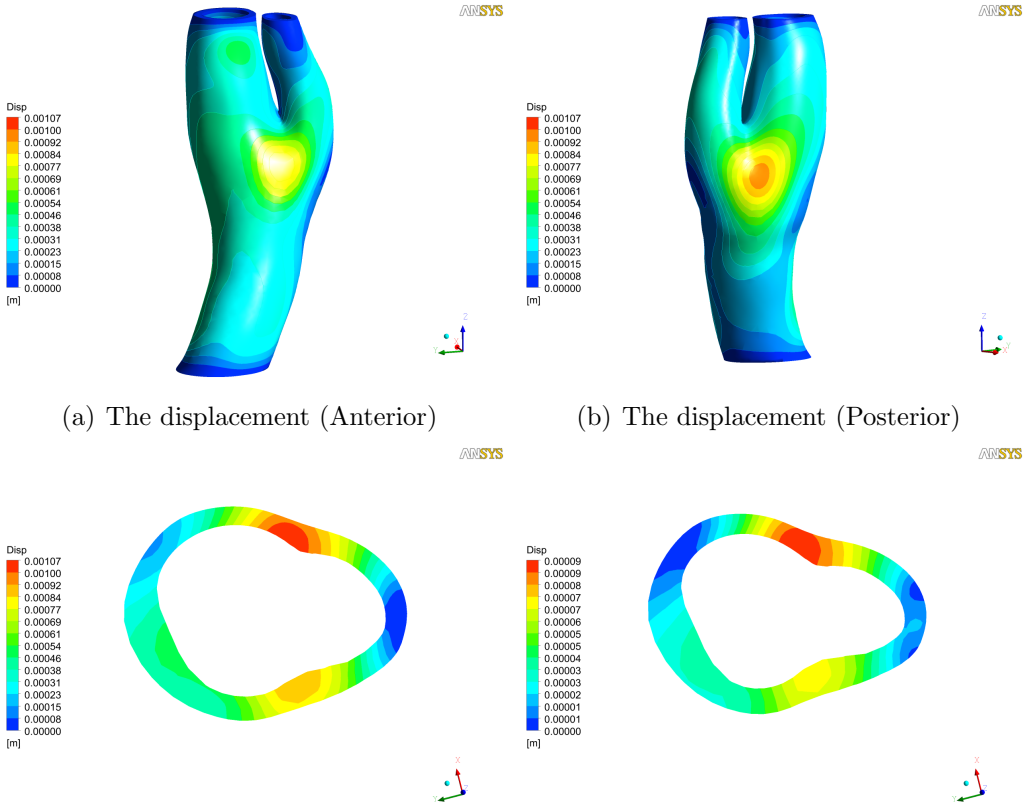

(a) The displacement (Anterior)

(b) The displacement (Posterior)

(c) Cross section at maximum pressure

(d) Cross section at minimum pressure

Figure 49: The dilation at the maximum pressure in subject 3

in the ECA (Fig. 49). In contrast to the previous two subjects, it can be found that high displacement is exhibited around the ECA due to shallow wall thickness and out-of-plane curvature. The stenosis is developed at both sides of the bifurcation outer wall, thus the dilation of arterial wall is not dominant in subject 3 (Fig. 49 (c), (d)); and this stenosis has maximum displacement taking place on the posterior side.

4.3.2 Flow patterns

Several cross sections are selected in the carotid artery to represent the flow patterns. This selection consists of four sites, i.e., CCA, middle of bifurcation, bifurcation apex and after the bifurcation apex. In the beginning of acceleration in diastole it is found that the flow pattern at this phase shows the most complex and complicated patterns. For this reason, the detailed velocity distribution at this time point on the selected cross section is presented in Figs. 50, 53, 56.

In subject 1, the flow pattern is less dynamic due to the simple geometric features including no evident curvature in the CCA. For this reason, reverse flow is restricted to the outer wall of ECA around the bifurcation apex (Fig. 50 (c)) for an entire cycle, and fully developed flow patterns are observed in the CCA. However, at the beginning of the bifurcation low velocity flow is present on the luminal surface around the connection of CCA and ICA/ECA due to the expansion of this area. Most of all, even in the diastolic phase there is no evident vortex flow pattern downstream of the carotid bulb in this subject. To demonstrate the effect of wall distensibility on flow patterns the detailed velocity field based on the rigid body assumption is exhibited in Fig. 51, and the flow patterns with FSI model are presented in Fig. 52. The cross section was chosen at the site where the maximum displacement took place, and several time points were selected to represent the flow pattern change over a cardiac cycle. The exact time points including the beginning of systole (BS), peak of systole (PS), the beginning of acceleration in diastole (BAD), peak of diastole (PD) and

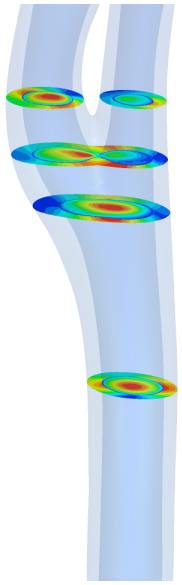

(a)

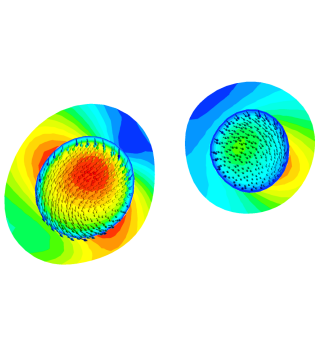

(b) After the bifurcation apex

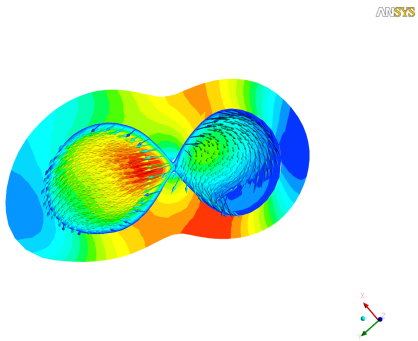

(c) Bifurcation Apex

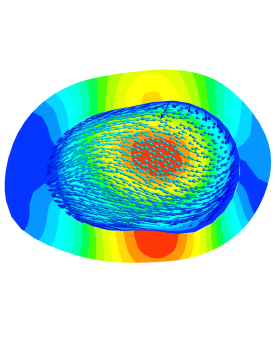

(d) Middle of bifurcation

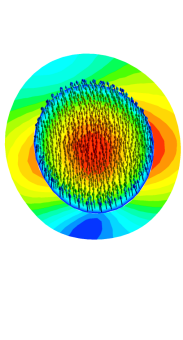

(e) CCA

Figure 50: Cross section in subject 1

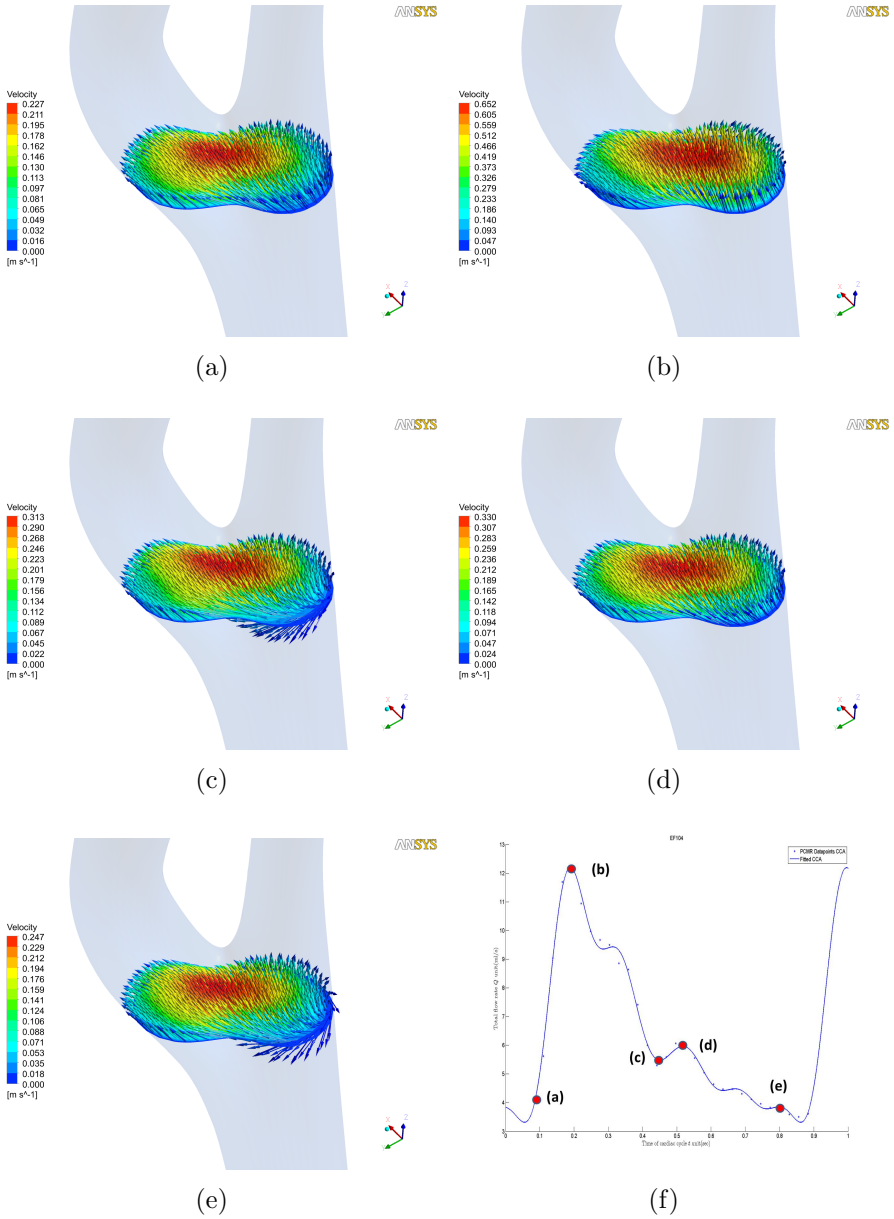

Figure 51: The flow pattern of subject 1 on rigid body assumption at selected phase in a cardiac cycle

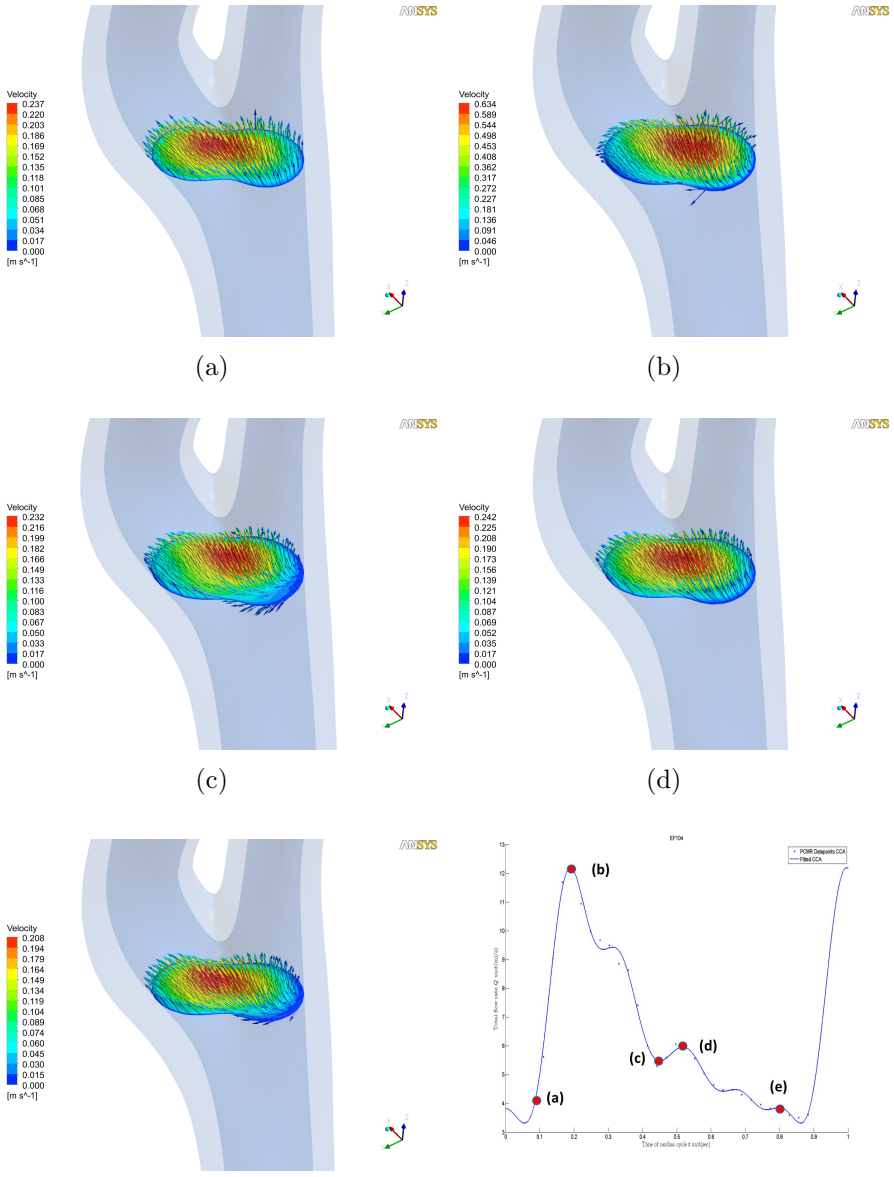

Figure 52: The flow pattern of subject 1 with FSI at selected phase in a cardiac cycle

minimum flow in diastole (MD) can be seen at the lower last diagram in each figure. Through a comparison between rigid body and FSI models it is found that global flow characteristics are very similar except that the strength of the recirculation and the maximum velocity magnitude are different between the two cases. The maximum velocity for the rigid body case is higher than that of FSI because the total volume available to hold the fluid is extended by the intraluminal pressure on the compliant arterial wall. This trend is observed at all selected time points. At the BAD, the recirculation in the region immediately proximal to the ECA (Fig. 52 (c)) increases somewhat in the FSI model. In each case, the reverse flow at the BAD in diastole is more developed than at the minimum flow in diastole, even though the flow rate at this time point is larger than the minimum flow.

In Fig. 53, the detailed flow field on the selected cross section in subject 2 at the BAD is presented. The geometrical features of this subject are more complicated than in subject 1. There is a severe curvature in the ICA and a mild stenosis in the beginning of the bifurcation proximal to the ICA. For this reason, strong and evident reverse flow and recirculation are observed downstream of the stenosis (Fig. 53 (d)). In the carotid bulb a helical complex flow pattern, accompanied by single vortex motion, is present at the outer wall. In contrast to the flow field in the ECA of subject 1, there is a mild recirculation at the outer wall and this pattern induces asymmetry in the ECA even far away from the flow divider (Fig. 53 (b)). In the CCA fully developed flow is present even though there is an out-of-plane moderate curvature between CCA and ICA/ECA. Consistent with the comparison between rigid body and FSI models in subject 1, the global flow features are similar in these two cases except for the strength of recirculation and the occurrence of reverse flow. In the rigid body model, there is no reverse flow at the maximum flow rate, however, there is a small reverse flow near the wall in the FSI model (Fig. 55 (b)). In contrast small reverse flow can be seen in the rigid body case at the minimum flow phase, but

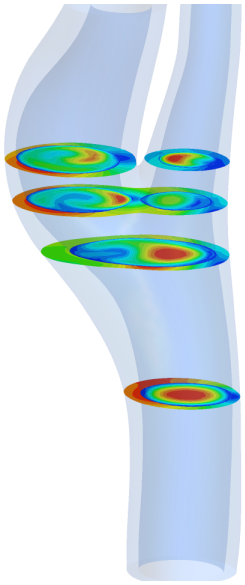

(a)

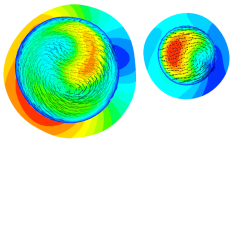

(b) After the bifurcation apex

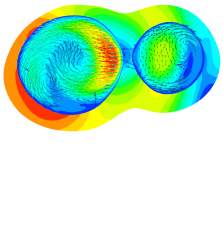

(c) Bifurcation Apex

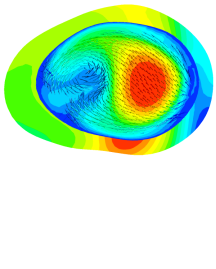

(d) Middle of bifurcation

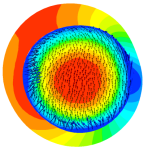

(e) CCA

Figure 53: Cross section in subject 2

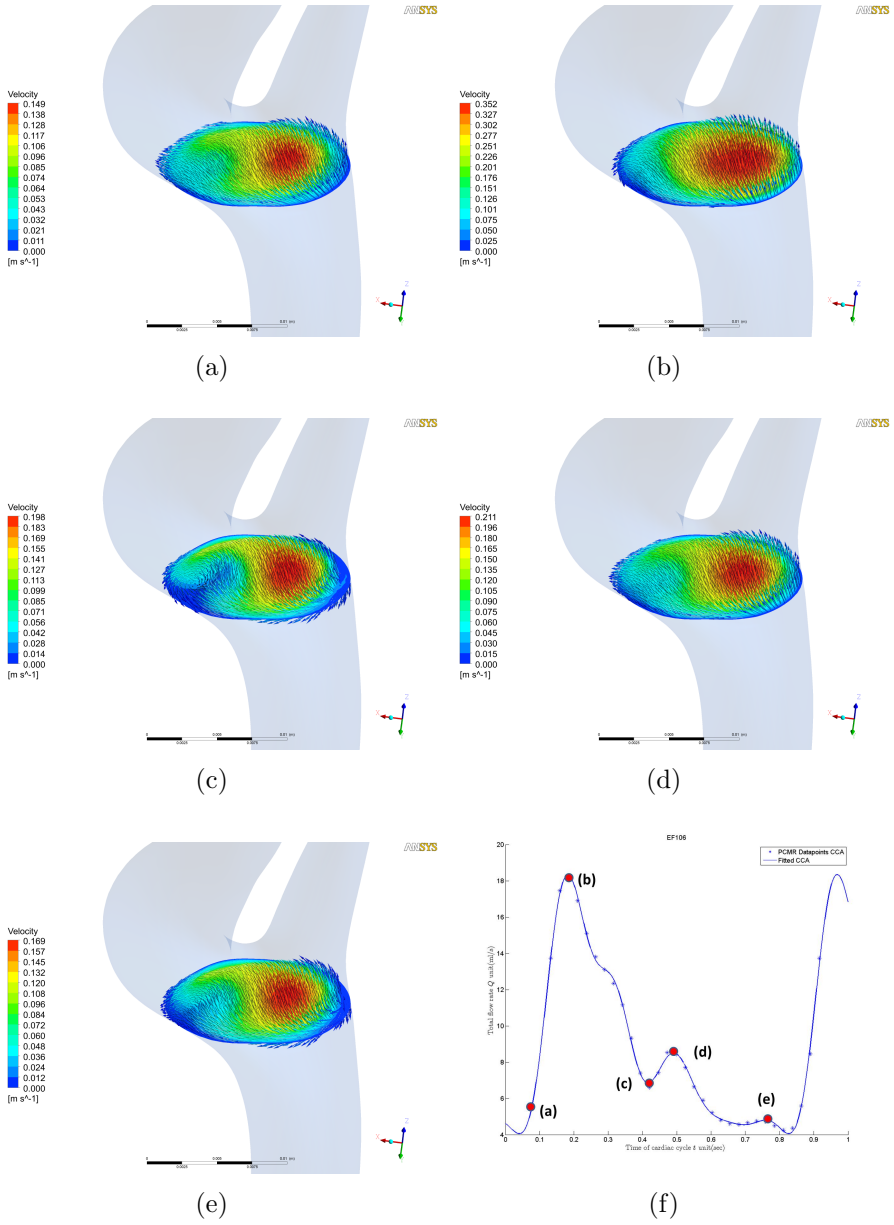

Figure 54: The flow pattern of subject 2 on rigid body assumption at selected phase in a cardiac cycle

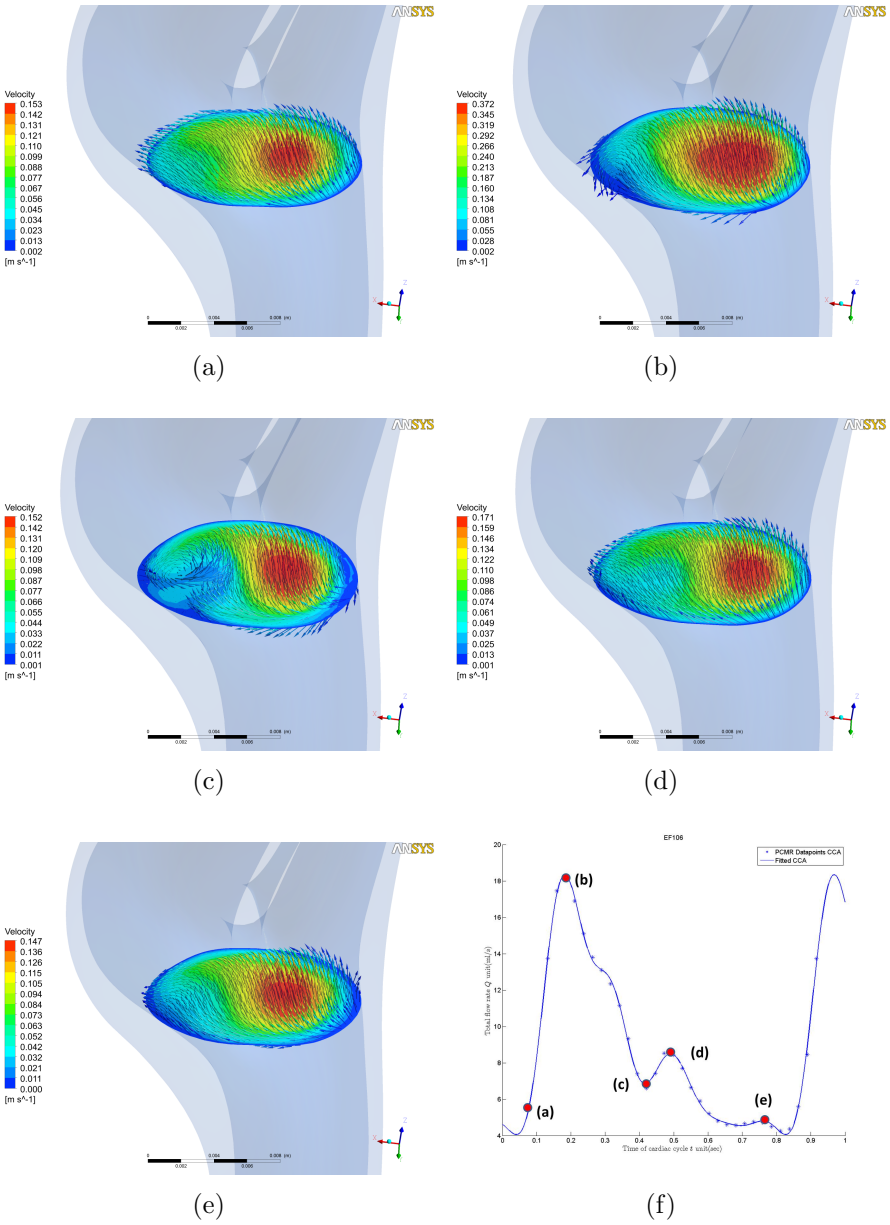

Figure 55: The flow pattern of subject 2 with FSI at selected phase in a cardiac cycle

no reverse flow is apparent in the FSI model. At the BAD, the area of recirculation is extended to the core of the main flow and at the same time this motion causes stronger reverse flow patterns than the rigid body model downstream of the stenosis and in the proximal ICA (Fig. 55 (c)).

In subject 3, there is no tortuous curvature in the ICA but the curvature in the CCA shows non-planarity. The stenosis is evident in the entrances of ICA and ECA on the anterior side (Fig. 9). This geometrical feature stimulates the occurrence of complex flow fields in both of ICA and ECA (Fig. 65 (a)). The detailed flow pattern on a selected cross section is shown in Fig. 56 at the beginning of the acceleration phase in diastole. The curvature in the CCA yields asymmetrical flow patterns. On the middle of the bifurcation, flow is skewed to the posterior side of the wall, inducing a vortex flow at the entrance of the ICA, and this yields reverse flow on the opposite side. Downstream of both stenoses there is a recirculation, and this pattern extends into the entrance of ICA and ECA; thus at the bifurcation apex, a vortex and reverse flow are observed at the anterior side of the wall. The spiraling flow pattern with single vortex motion downstream of ICA and ECA exhibits even beyond the bifurcation apex (Fig. 56 (b), (c)). As with the previous subjects 1 and 2, high velocity is present at the flow divider in the inner wall of the bifurcation apex. Consistent with the comparison between rigid body and FSI model of subject 1 and 2, the global flow characteristics remain unchanged, however, it still has transient and spatial differences between the two cases. At the time of maximum flow the reverse flow area is present on the anterior side in the proximal ICA in the FSI model (Fig. 58 (b)), but it cannot be found in the rigid model (Fig. 57 (b)). However, at the time of minimum flow rate, a stronger vortex and an increase in recirculation is observed in the rigid body calculation. At the BAD, it can be shown that a strong vortex and recirculation develops on both anterior sides of the connection of CCA and ICA/ECA in both models (Fig. 57 (c), 58 (c)). In all phases, the maximum velocity in the rigid

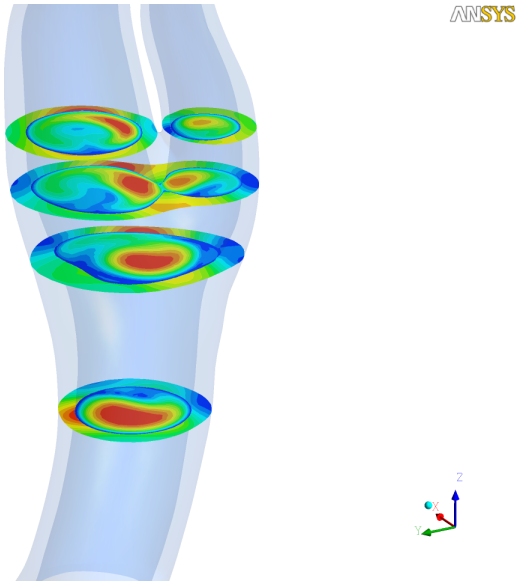

(a)

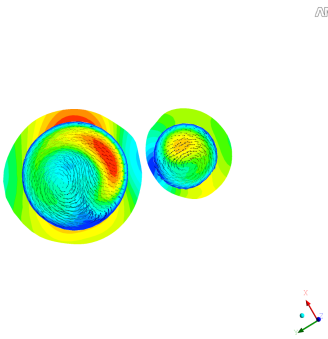

(b) After the bifurcation apex

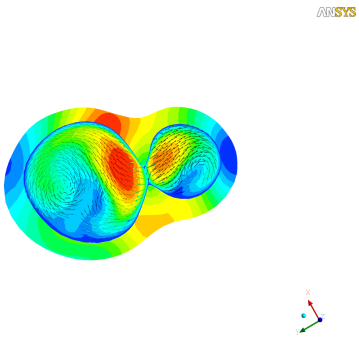

(c) Bifurcation Apex

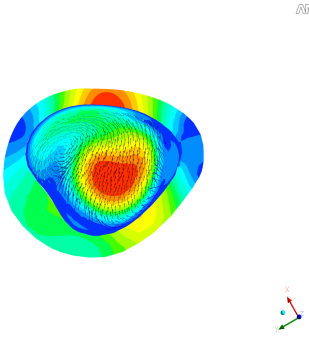

(d) Middle of bifurcation

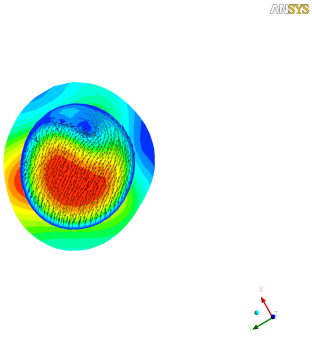

(e) CCA

Figure 56: Cross section in subject 3

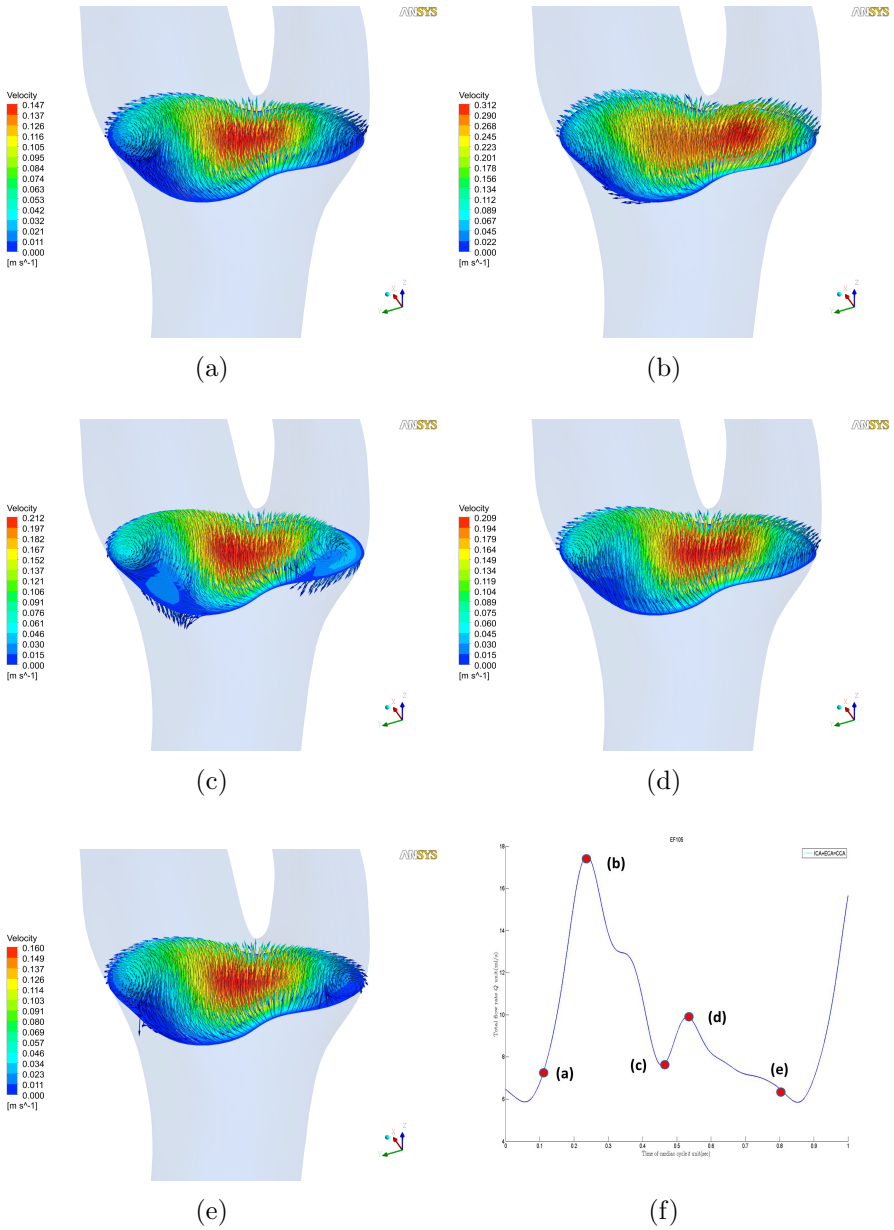

Figure 57: The flow pattern of subject 3 on rigid body assumption at selected phase in a cardiac cycle

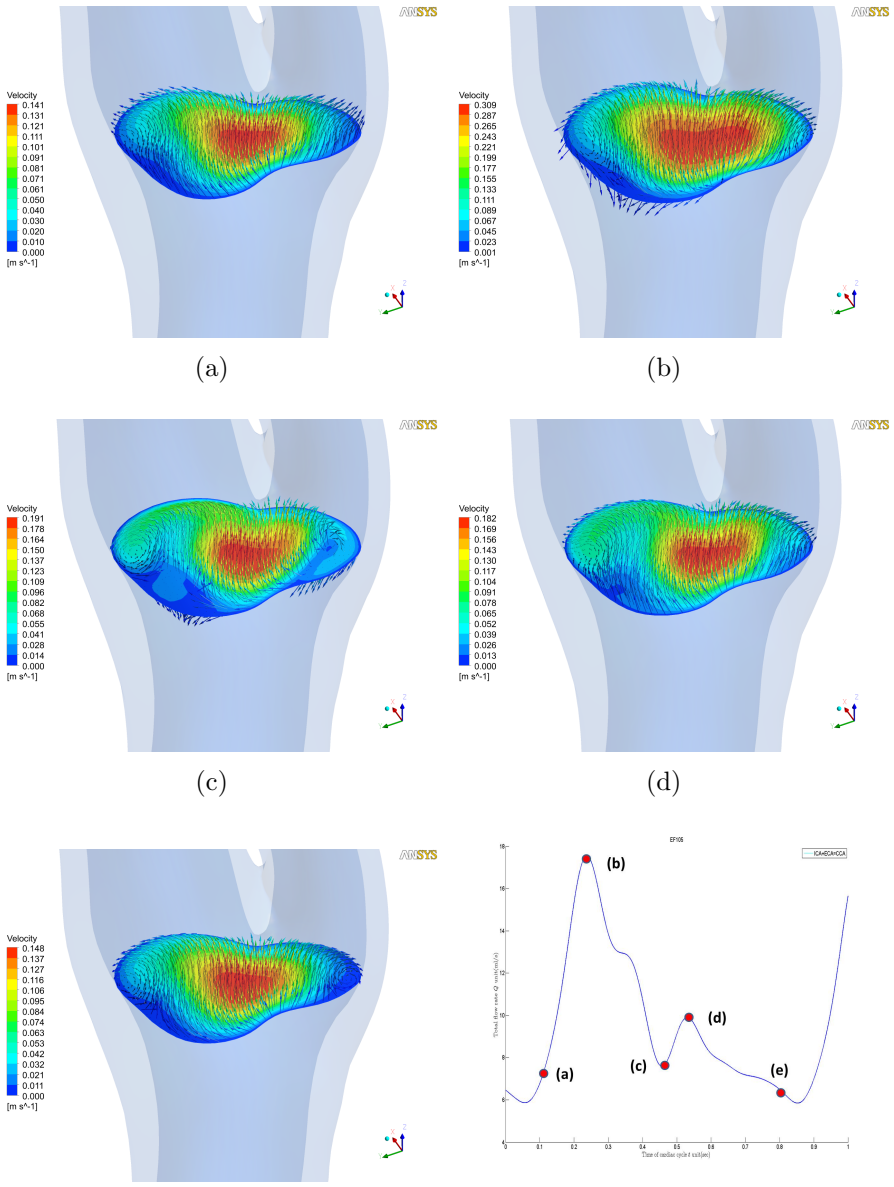

Figure 58: The flow pattern of subject 3 with FSI at selected phase in a cardiac cycle

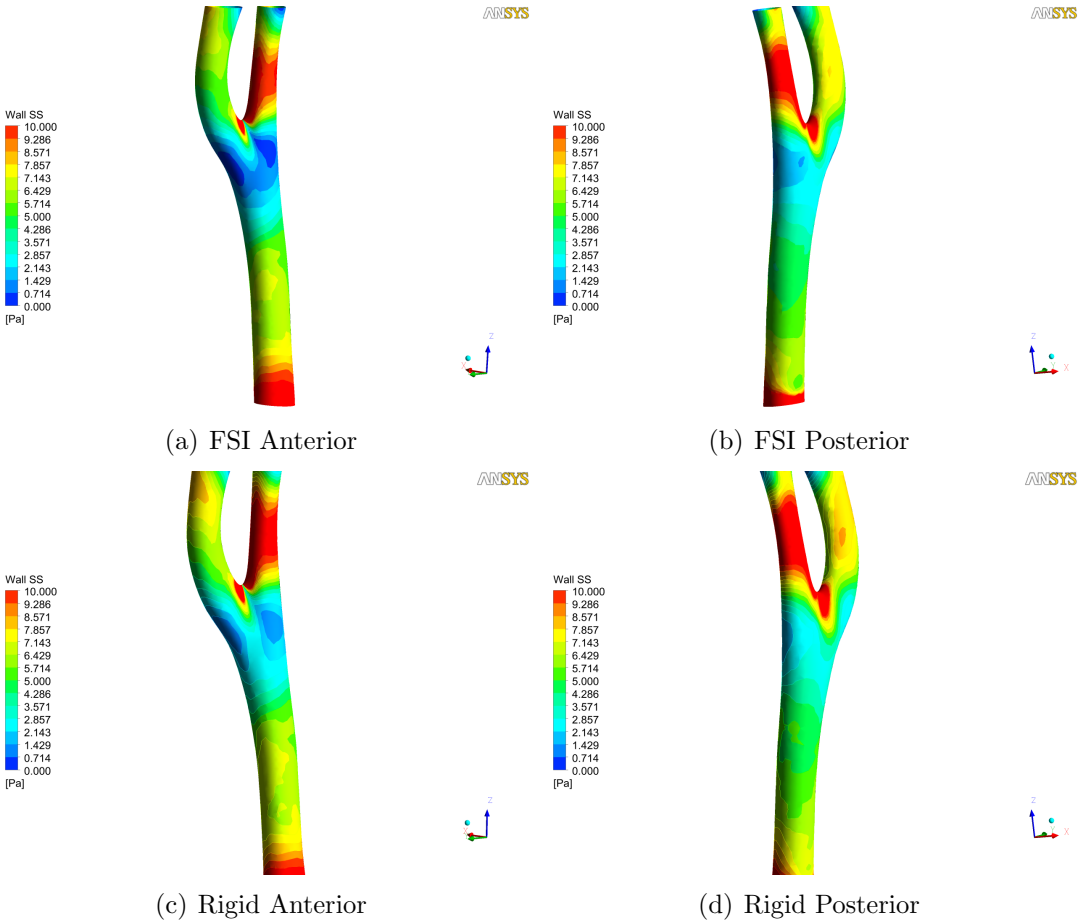

(a) FSI Anterior

(b) FSI Posterior

(c) Rigid Anterior

(d) Rigid Posterior

Figure 59: Comparison of wall shear stress at the maximum flow in subject 1

body model is higher than in the FSI case due to the expansion of the compliant arterial wall which leads to extra volume.

4.3.3 Wall shear stress

Wall shear stress is influenced primarily by the flow pattern thus the distribution of wall shear stress follows the similar trend of the flow pattern in rigid body and FSI models. In each subject WSS arising from the two models at maximum flow in systole and minimum flow in diastole is compared to determine the effect of wall distensibility. In subject 1, at the maximum flow rate, it can be shown that low WSS (below $0.5Pa$) in the FSI model is present at the beginning of carotid bulb and at the anterior side of the connection between CCA and ECA. However, there is no comparable low WSS

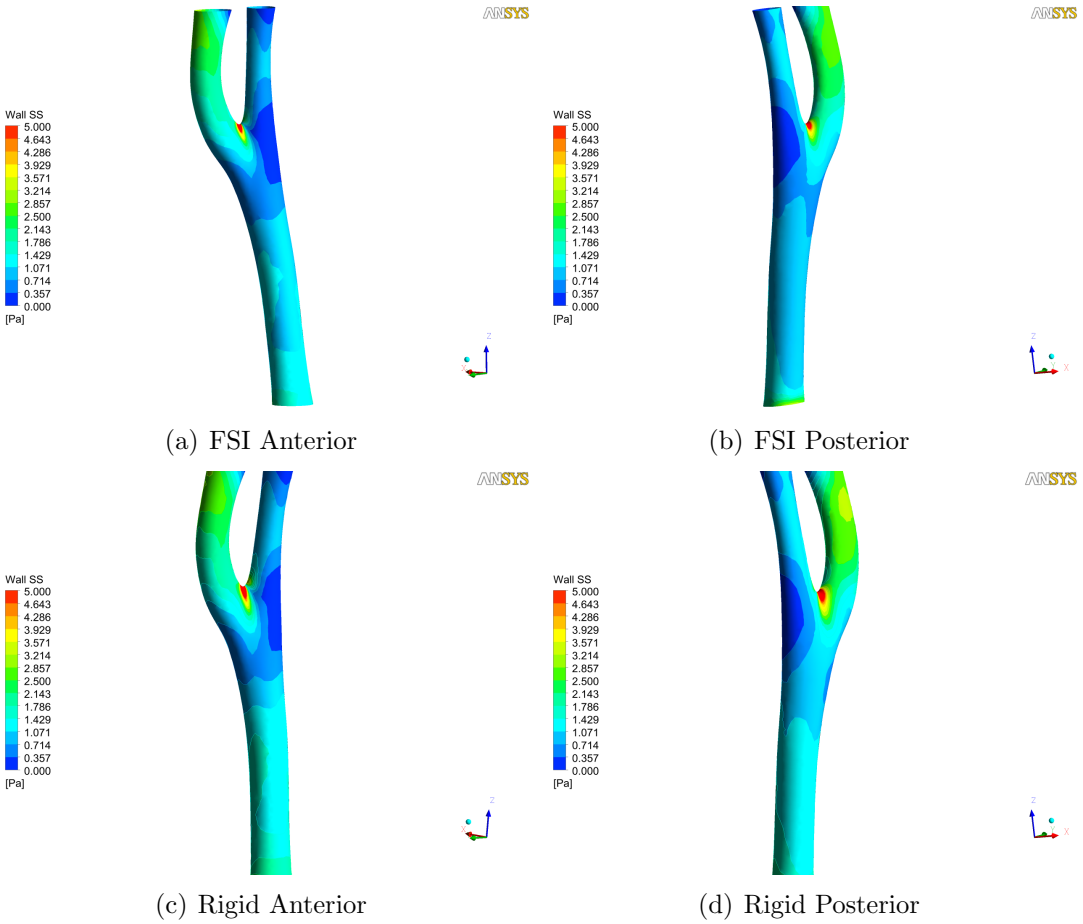

(a) FSI Anterior (b) FSI Posterior

(c) Rigid Anterior (d) Rigid Posterior

Figure 60: Comparison of wall shear stress at the minimum flow in subject 1

in the rigid arterial model (Fig. 59). Through comparison between the lowest WSS region in each case the compliant arterial wall induces a reduction of WSS by as much as 100% (Fig. 59 (a), (c)). In both cases, at maximum flow phase, there is no LWSS (Low WSS) at the posterior side of subject 1. In the minimum flow rate state, the distribution of LWSS is similar between both cases, in which the lowest WSS is shown at the anterior side and outer wall of the ECA around the connection between CCA and ECA (Fig. 60).

The lateral movement of the arterial wall due to the asymmetrical geometrical features in subject 2, including the stenosis at the entrance of carotid bulb and tortuous curvature of ICA, leads to a helical flow pattern in the carotid sinus distal to the stenosis. Thus, it can be expected that LWSS is dominant in the ICA and a

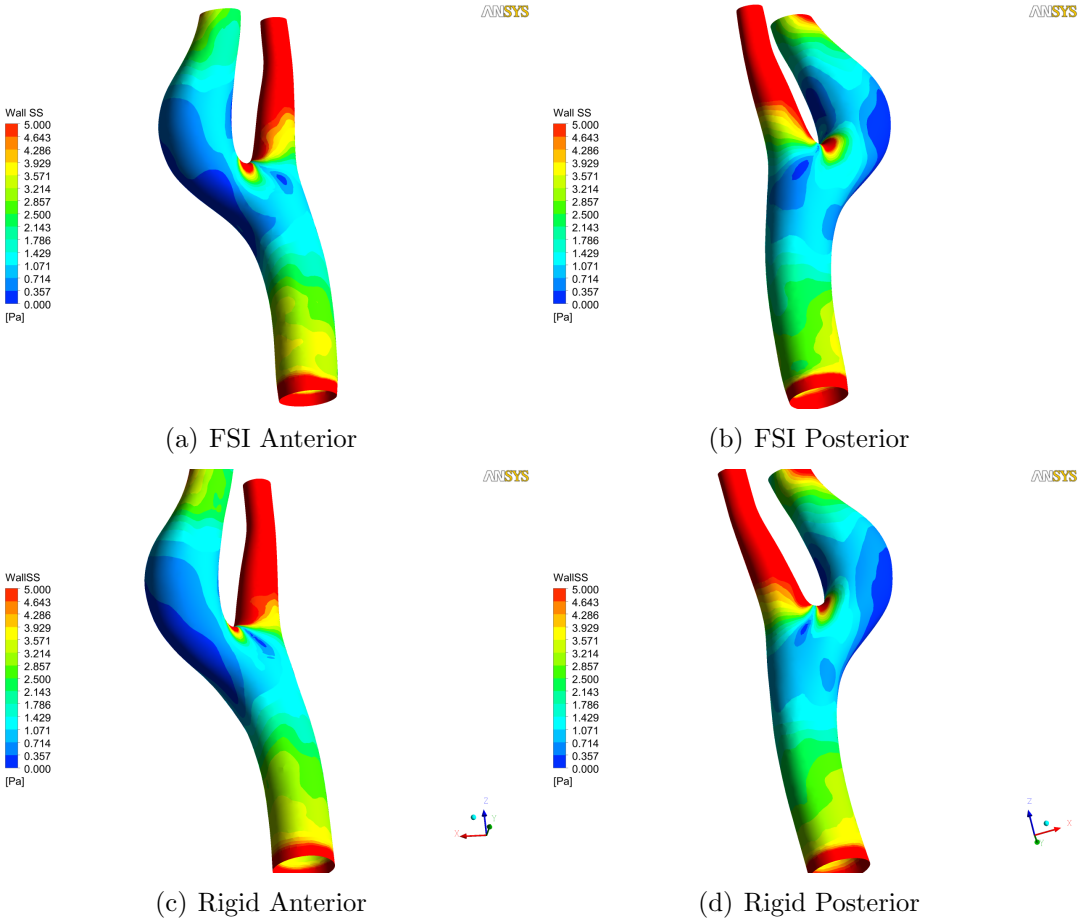

(a) FSI Anterior (b) FSI Posterior

(c) Rigid Anterior (d) Rigid Posterior

Figure 61: Comparison of wall shear stress at the maximum flow in subject 2

relatively higher WSS in the ECA. The consequences of WSS in both models support this expectation, as shown in Figs. 61, 62. At the maximum flow in systole, there is no LWSS region in the ECA, however, on the downstream of the stenosis to the superior direction to ICA, LWSS covers most of area of the carotid bulb including the wall of the flow divider right after the bifurcation apex. In general, the wall of the flow divider experiences high WSS around the bifurcation apex, but the tortuous curvature of ICA and the non planarity between CCA and ICA/ECA brings about the asymmetric single core vortex after the bifurcation apex, and this makes LWSS exhibit on this sites in contrast to the high WSS in the ECA (Fig. 61). The wall shear stress distribution exhibits a similar trend between rigid body model and FSI except the size of covered area by LWSS due to the wall expansion, which causes the

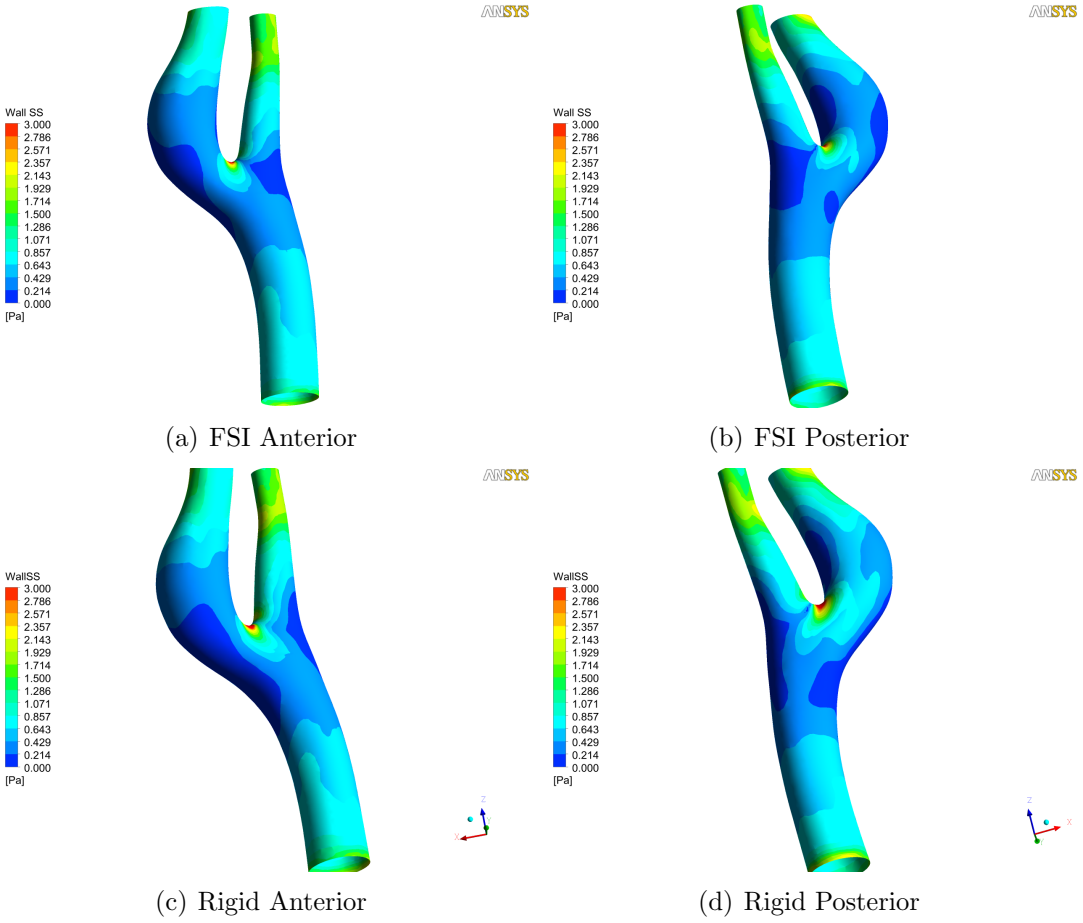

(a) FSI Anterior

(b) FSI Posterior

(c) Rigid Anterior

(d) Rigid Posterior

Figure 62: Comparison of wall shear stress at the minimum flow in subject 2

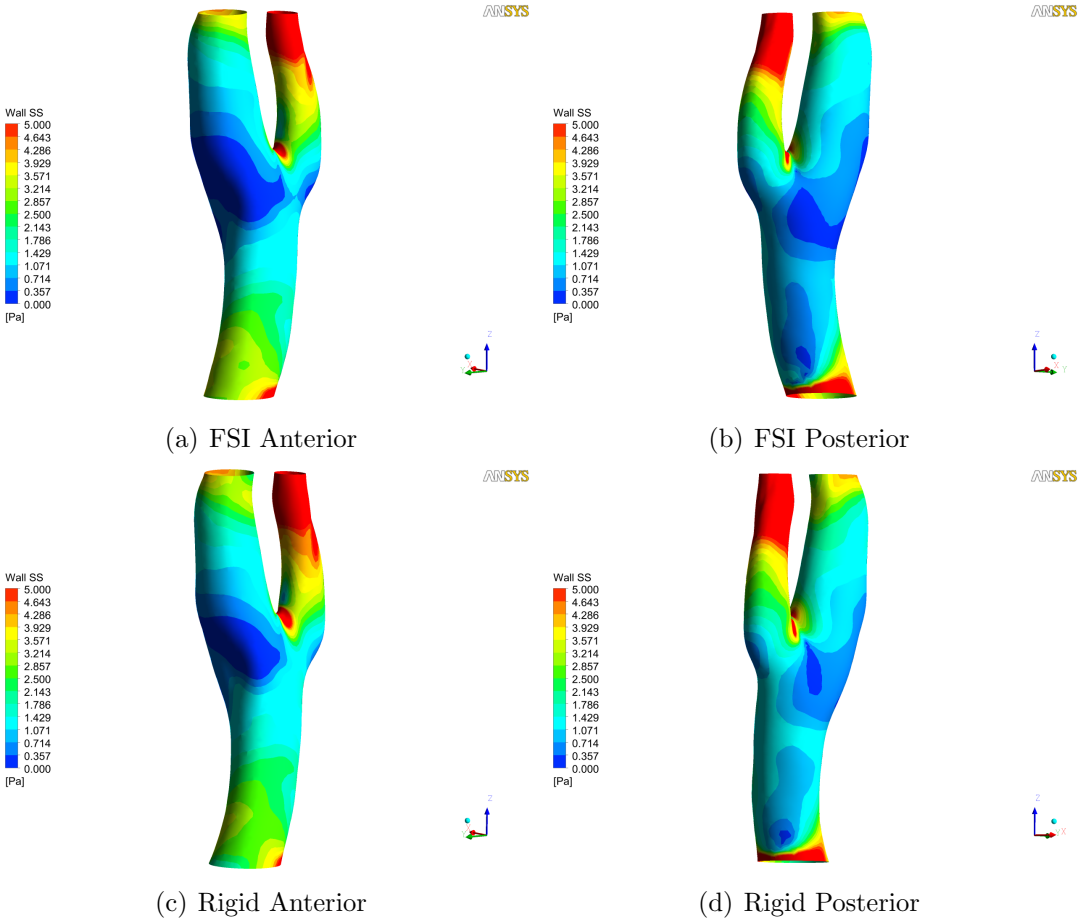

(a) FSI Anterior

(b) FSI Posterior

(c) Rigid Anterior

(d) Rigid Posterior

Figure 63: Comparison of wall shear stress at the maximum flow in subject 3

velocity to decrease instantaneously at maximum flow phase. In the minimum flow phase, the LWSS is extended into the region upstream of the stenosis in CCA and is present at the connection of CCA and ICA/ECA on the anterior and posterior sides (Fig. 62). LWSS is observed at the entrance of ECA and CCA, which is not found in the maximum flow phase.

At maximum flow in the FSI model the LWSS covers more area due to the wall distensibility, and this trend is also found in subject 3, consistent with findings in subjects 1 and 2. LWSS in FSI model is observed downstream of the stenosis at the entrance of the ICA, and it extends to the posterior side of CCA (Fig. 63). In the rigid body case LWSS is present at the same site even though the size is reduced by around half and there is no dominant LWSS region in the CCA posterior side. At

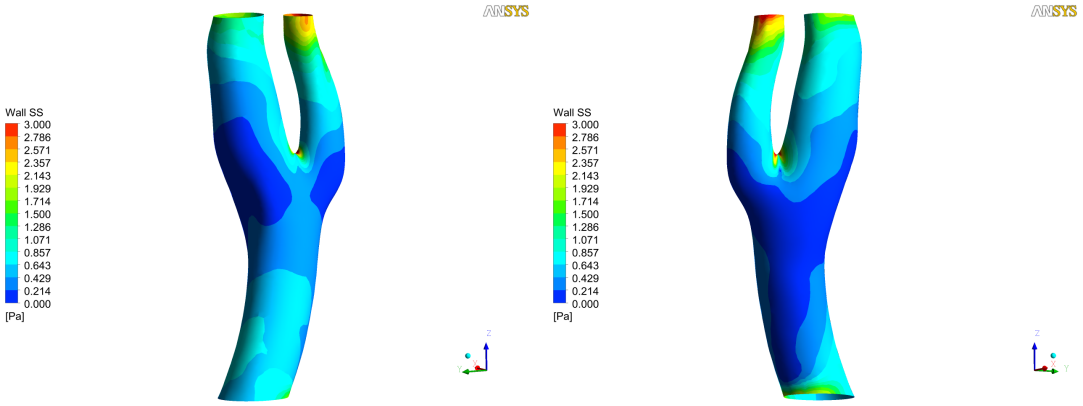

(a) FSI Anterior

(b) FSI Posterior

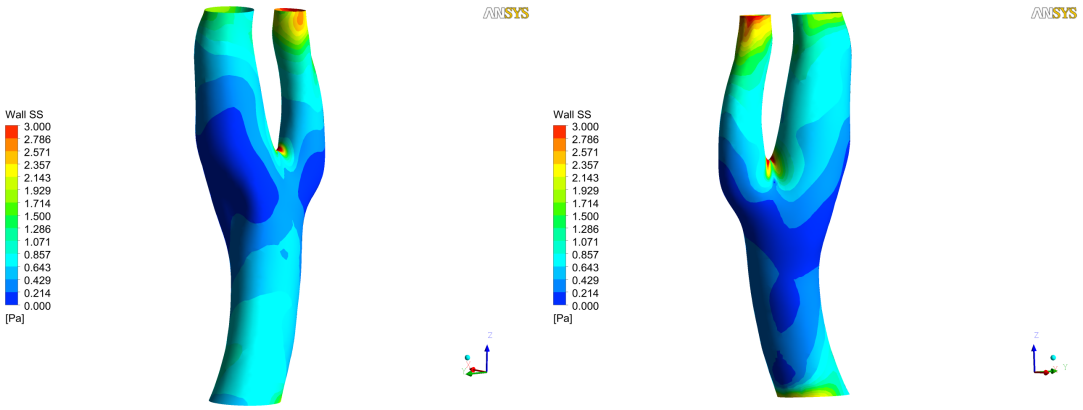

(c) Rigid Anterior

(d) Rigid Posterior

Figure 64: Comparison of wall shear stress at the minimum flow in subject 3

the entrance of ECA, LWSS also can be found due to the sudden expansion of area, however, this is very restricted to right after the stenosis. In the minimum phase it is hard to find difference of the distribution of WSS in both cases except on the posterior side of the CCA. The LWSS area extends to the entrance of CCA and covers most of the carotid bulb. Downstream of the stenosis around the entrance of ECA, also shows that LWSS is dominant in this region.

The streamlines which were calculated from the inlet of the CCA at the BAD demonstrate that complex helical flow patterns prevail in most of the region in subject 3, including at the posterior side of the CCA, downstream of the stenosis proximal to the entrance of ECA, and downstream of the stenosis in the carotid sinus (Fig. 65 (a)). To demonstrate that LWSS regions experience the oscillation of WSS with various magnitude and direction, WSS vectors which are taken from above the three locations (Fig. 65 (b)), are visualized in a cardiac cycle. 3D vectors are projected into the principal plane in which two WSS vector components are dominant to the other component and the cartesian coordinates of each vector are transformed to polar coordinates. The result of these vector distributions shows that WSS oscillates with varying direction and magnitude in these regions (Fig. 65 (c),(d),(e)) and this suggests the possibility that the physiological response of endothelium to the formation of leaky junctions is not simply in the case of only considering LWSS. The oscillation effect on the incidence of apoptosis and mitosis should also be considered if experimental evidence exists to support this.

It is not easy to make general statements on the effects of wall distensibility upon general WSS patterns because WSS changes transiently and spatially with geometrical characteristics in each subject. However, the intraluminal pressure acts on the compliant arterial wall, and this leads to an expansion of the lumen space containing the fluid and finally brings about a velocity decrease which, in turn, tend to cause lower shear rate at the surface. For this reason, the difference of WSS in the

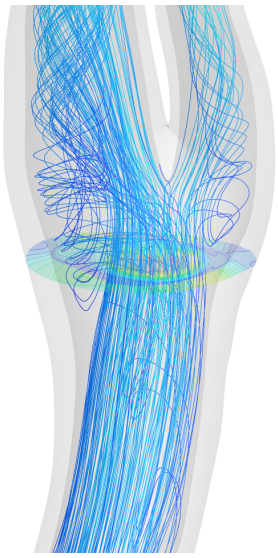

(a) Streamlines from the CCA of subject 3 at BAD

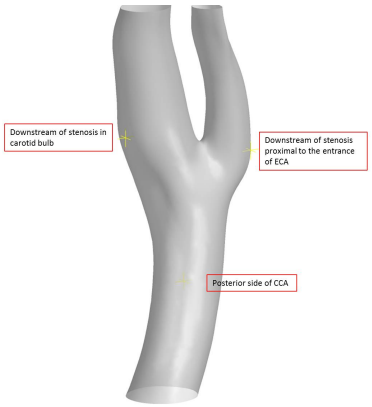

(b) The location of WSS vector taken

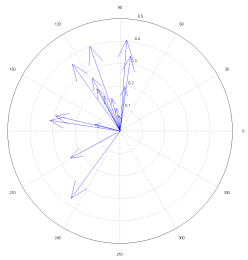

(c) Downstream of stenosis in carotid sinus

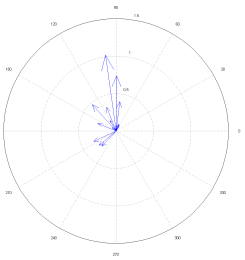

(d) Downstream of stenosis proximal to the entrance of ECA

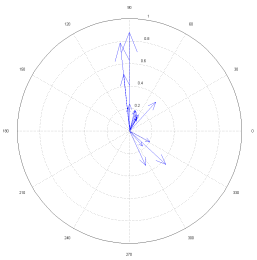

(e) Posterior side of the CCA

Figure 65: Oscillation of WSS vector at low WSS regions of subject 3

specific location and time between rigid body and FSI model is more evident when the displacement is maximized by the pressure. This can be seen in all subjects in our research. At the same site the area covered by LWSS regions in the rigid body assumption are enlarged and the magnitude is reduced as much as over 100% when this site is distended by the pressure. This is not apparent at the minimum flow rate in diastole due to lower pressure, but WSS differences still can be seen in comparing LWSS regions. This result is supported by previous research done by other FSI experiment and computational calculation. Perktold et al. [67] calculated the WSS based on an ideal carotid bifurcation model using FSI method, and they found that WSS was reduced by 25% due to the wall distensibility. Anayiotos et al. [3] measured the wall velocity near the wall using laser doppler velocimetry from carotid bifurcation models with rigid and compliant walls which had the same internal configuration. WSS calculated from these measurements showed that time averaged WSS from the compliant wall dropped about 30% compared to rigid wall model, and they also found that in some locations instantaneous WSS alterations by the wall expansion reached as much as 100%. This observation is consistent with our research results.

CHAPTER V

LDL MASS FLUX AND VOLUME FLUX THROUGH THE ENDOTHELIUM

5.1 Fraction of leaky junction and three pathways

In previous research on mass transfer it has been found that the permeability of LDL and the filtration flow are critical for determining the LDL distribution qualitatively and quantitatively on the surface between lumen and endothelium. On the endothelium, the permeability and the filtration flow were treated as though these parameters have constant values over the surface, without considering that the mechanical environment affects the endothelium and arterial wall, which may cause these parameters change locally as a result.

The endothelium is a major resistance to LDL mass transfer from the lumen to arterial walls. LDL cannot pass through paracellular pathways because the size of LDL is too large to pass through tight junctions between endothelial cells. For this reason the major pathway for LDL particle transport is through so-called leaky junctions by convective filtration flow caused by the pressure gradient in the arterial wall [14, 15, 99]. Leaky junction formation depends on apoptosis and mitosis of endothelial cells, and the incidence of cellular death and proliferation is related to the mechanical environment. To elucidate causal relationships for the effect of mechanical force on LDL mass transport via the leaky junction pathway it is essential to develop biological evidences and experimental results and construct a theoretical model. Even though hypertension [102] and cyclic mechanical strain [59] have been recognized as possibly affecting the increase of the incidence of leaky junctions, there is inadequate information to support a theoretical model. In contrast, the relationship of WSS

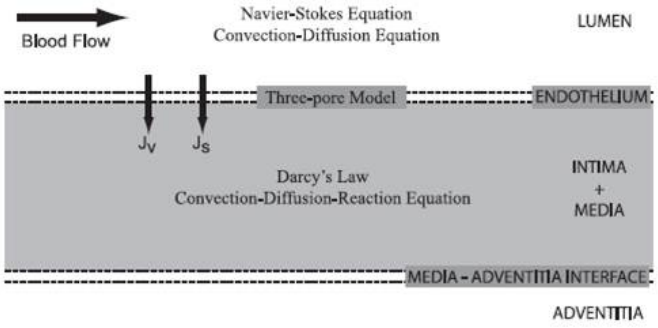

Figure 66: Three pathways through the endothelium [65]

(wall shear stress) with LDL mass transport has been examined through in-vivo and in-vitro studies, and it is found that the incidence of leaky junctions changes with the amount of wall shear stress acting upon endothelial cells. In the vasculature, greater formation of leaky junctions has been observed at sites where LWSS is present, i.e., bifurcations and curvatures. Macromolecule mass transport through the endothelium is enhanced at these locations by plasma filtration flow via leaky junctions. For this reason it is not enough to assume constant permeability of LDL on a subject specific arterial model because the variation of wall shear stress causes change in the occurrence of leaky junction formation, which in turn leads to variations in solute flux. There is little research to define precise mechanisms between WSS and leaky junction formation on the endothelium. Thus, it is critical to set up a mathematical model for the computational study based on experimental results about the physiological adaptation of endothelial cells to WSS and the incidence of apoptosis and mitosis after endothelial cell reaction to WSS. This approach has been taken by Olgac et al. [65].

These investigators consider LDL mass transport across the endothelium to consists of three pathways, vesicular transcytosis, flux through normal junctions, and flux through leaky junctions. Most macromolecule mass transport investigations [2, 29, 49, 68, 81, 86, 96] treat the endothelium as having a single pathway. However,

in their research the contribution of each pathway to solute flux and volume flux was determined and the role of leaky junctions in LDL mass transport was examined more detail. To overcome the lack of knowledge of no direct physiological causal relationship between leaky junctions and wall shear stress they set up the concept of the fraction of leaky junctions (ϕ), which is defined as the ratio of the area occupied by leaky cells to the total area of cells. Based on published biological experimental data they formulated a quantitative mathematical model to link the local fraction of leaky junction and local wall shear stress as seen in Eqn. (16).

$$\begin{aligned} SI &= 0.380e^{-0.790WSS} + 0.225e^{-0.043WSS} \\ \#MC &= 0.003797e^{14.75SI} \\ \#LC &= 0.307 + 0.805 \times (\#MC) \\ \phi &= \frac{\#LC \times \pi R^2{}_{Endo}}{Unitarea} \end{aligned} \tag{16}$$

where SI is the shape index of endothelial cells and represents the alignment of these cells under local wall shear stress, $\#MC$ is the number of mitotic cells at the regions with specific shape index observed by Chien et al. [22], $\#LC$ is the number of leaky cells which is correlated with the number of mitotic cells. Finally the local fraction of leaky junction is assigned based on the number of leaky cells in the unit area. After obtaining the fraction of leaky junction, transport properties of normal junction and leaky junction, i.e., hydraulic conductivity, LDL diffusive permeability, the reflection coefficient of particle, were computed using pore theory. More detailed background of pore theory can be found in Olgac et al. [65].

In LDL mass transport research, an electrical circuit concept has been utilized to acquire the filtration flow in the arterial wall, in which the pressure gradient between endothelium and the interface to the media-adventitia acts as the moving force for plasma flow in the porous media, and the overall resistance is replaced by the contribution from each structure, i.e., endothelium, IEL and media to filtration flow

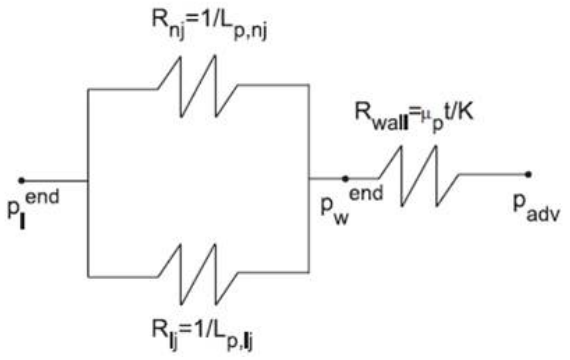

Figure 67: Electrical circuit analogy to the volume flux [65]. P_l^{end},P_w^{end} and P_{adv} are the pressure at the lumen on the endothelium, at the wall side of below endothelium and at the interface of the media and adventitia.

[2, 68]. Fig. 67 illustrates how they calculate the volume flux ($J_{v,i}$) for each pathway. The resistance of endothlelium and IEL is represented by the inverse of the hydraulic conductivity of leaky junction ($L_{p,lj}$) and normal junction ($L_{p,nj}$) at the site, which is obtained by pore theory based on the local fraction of leaky junctions. The latter is set up as a constant value and works as the resistance to filtration flow through normal junctions. In the media region, the filtration is determined by the wall thickness (t) and the permeability of the media structure, which has been recognized as Darcy′s permeability (K_D).

In general, to obtain the filtration flow it is necessary to set up the governing equation for flow in the porous medium. Several models, i.e., Darcy′s law [49, 65, 86], Brinkman′s model [81, 96] and homogenized Navier-Stokes equations [2], have been suggested to implement the filtration flow calculation. In the arterial wall environment Darcy′s law model (Eqn. (18)) is a appropriate model for filtration flow because the corresponding Re is much less than 1 and accordingly transient effects of flow are negligible [86]. In our research, wall thickness is obtained from black blood MRI image processing and Darcy′s permeability is assigned as $2.0 \times 10^{-18} m^2$ [2]. The luminal pressure P_w^{end} is set as $120 mmHg$ which is a middle value of the physiological pressure range applied in FSI calculation and $30 mmHg$ is chosen as the pressure boundary condition at the media-adventitia interface P_{adv} [2]. Thus, $90 mmHg$ was applied as the actual pressure difference (∇P) to induce the filtration flow. The plasma viscosity

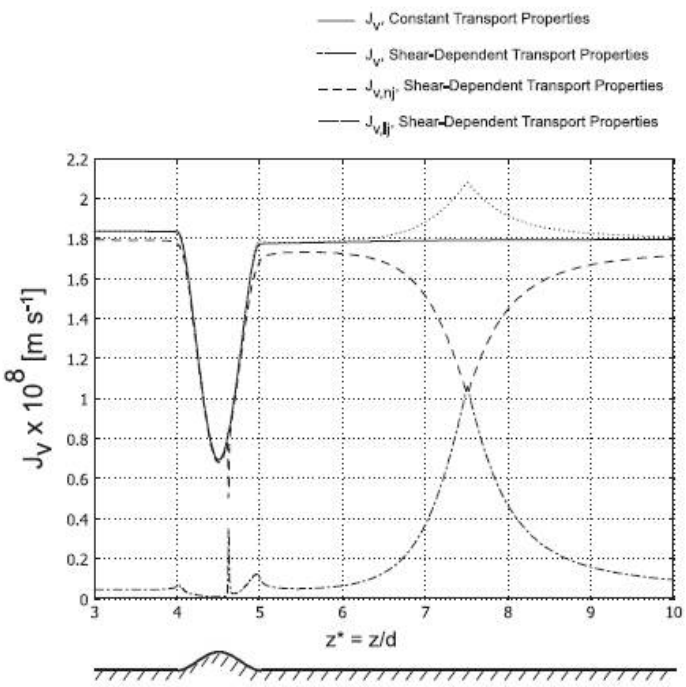

Figure 68: Volume flux at each pathway in 2D stenosis [65]

is less viscous than the bulk blood flow and taken as $7.2\times10^{-4} Pa{\cdot}s$ [26].

The verification of this approach using a 2D stenotic arterial geometry, which is simple but can produce key flow field features including recirculation, demonstrates the importance of the WSS dependent feature in plasma flow as shown in Fig. 68. The results of volume flux through normal and leaky junctions show that in the vicinity of the reattachment point ($z^* = 7$) where the lowest WSS is present, the volume flux through leaky junctions increases. In contrast, volume flux through normal junctions decreases because the formation of leaky junctions enhances hydraulic conductivity of this pathway, which means the resistance to movement of filtration flow is reduced. However, total volume flux is not influenced significantly by leaky junction formation, supporting the fact that the cleft in the normal junction is a main passage for plasma flow [91]. Total volume flux is dependent on the wall thickness, and this also can be found through total volume change in the stenosis region in which total filtration flow decreases as wall thickness become greater. For this reason, it is necessary to include

in-vivo arterial wall thickness from MRI.

To obtain LDL mass flux into the intima the apparent permeability Pe_{app} needs to be calculated because mass flux is determined by the multiplication of Pe_{app} and the concentration of LDL in the lumen. As already mentioned, an LDL particle cannot move into the intima via a normal junction, and thus the contribution of normal junctions to the permeability of endothelium to LDL (${Pe_{app}}^{NR}$), is not included for LDL pathways. Local WSS effects on the permeability via transcytosis, Pe_{trans}, is also negligible based on the observation by Cancel et al. [14]. Thus, the distribution of Pe_{app} is determined primarily by the apparent permeability of leaky junction, ${Pe_{app}}^{LK}$, which consists of the convective effect of volume flux through leaky junctions ($J_{v,lj}$), and the diffusion effect of LDL concentration at the pore entrance. This approach finally makes it possible to consider local WSS effects on the apparent permeability of endothelium to LDL particles.

It should be noted that in our research, mass transport with in the arterial wall itself is not considered due to the consequences of various theoretical and experimental studies of LDL [2, 65, 68, 86, 87]. While it would be interesting to model the LDL concentration across the arterial wall, it is found that high mass flux on the endothelium leads to high concentration in the intima and, sequentially, in the media. This concentration pattern follows a smooth curve in which the concentration decreases gradually from the wall side of endothelium to the interface of media-adventitia [58]. Even though a slight rise of LDL concentration is observed in the intima in a multi-layered model compared with the single-layered case, the general trend remains unchanged [68]. For this reason, mass flux distribution is considered as the indicator to show the possible sites for plaque formations in our research. Therefore, based on time averaged WSS from FSI calculations, the mechanism suggested by Olgac is implemented with Matlab and the result is visualized by CFX post (Ansys, Canonsburg, PA).

5.2 Results and Discussion

5.2.1 Time averaged WSS from FSI

The characteristic time scale of the pulsatility of blood flow is on the order of one second compared with a time on the order of hours required for many forms of endothelial cell response to shear stress, such as cell alignment with flow and adhesion molecule expression. In the experiment which is utilized to extract a mathematical relationship between WSS and the fraction of leaky junction, the endothelial cell layers were exposed to shear stress for enough time to induce the cell response. For this reason, it is reasonable to calculate time averaged WSS in a cardiac period and obtain the formation of leaky junctions with respect to this value.

In Figs. 69 $\sim$ 71, TAWSSs (time averaged WSS) which come from FSI and rigid body simulations are presented and visualized based on the inner wall of each subject. In all subjects, the global trend of TAWSS distribution in both models is similar. However, arterial deformation caused by intraluminal pressure decreases TAWSS of FSI model. The influence of wall distensibility can be seen in the lower diagram in each figure by the percentage difference between TAWSS in two cases. A positive percentage value means that TAWSS of the rigid body model is larger, typically due to wall expansion causing a lower TAWSS for the FSI case. In contrast, a negative value means that TAWSS of the FSI model is higher than that of rigid body assumption.

In subject 1, which shows the simplest geometrical features in our research, TAWSS of the rigid body model is reduced by 20 $\sim$ 30% by comparison with the FSI model with some parts experiencing over 50% change in the CCA and the beginning of bifurcation around the entrance of ICA/ECA. However, in subject 2 and 3 which exhibits more complex geometrical characteristics compared with subject 1, TAWSS of FSI is higher than rigid case in the area around the stenosis. Just distal to the stenosis, TAWSS in the FSI model is higher by about double, even though

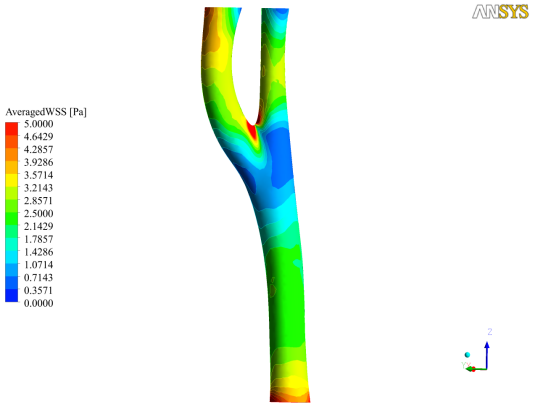

(a) FSI Anterior

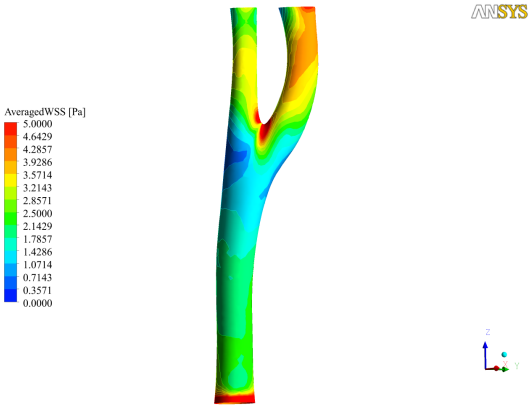

(b) FSI Posterior

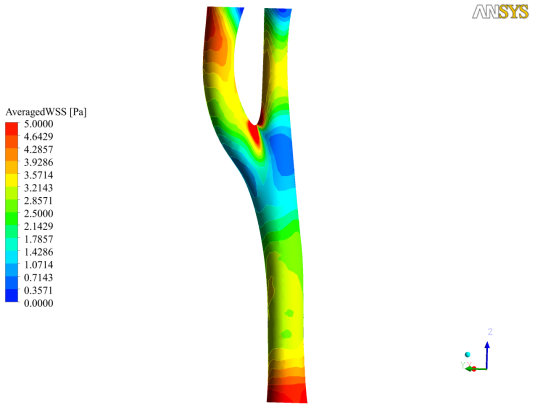

(c) Rigid Anterior

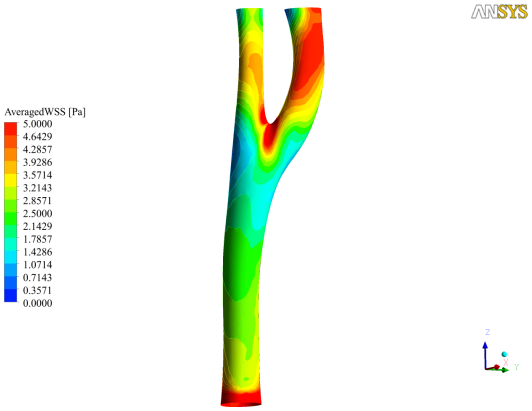

(d) Rigid Posterior

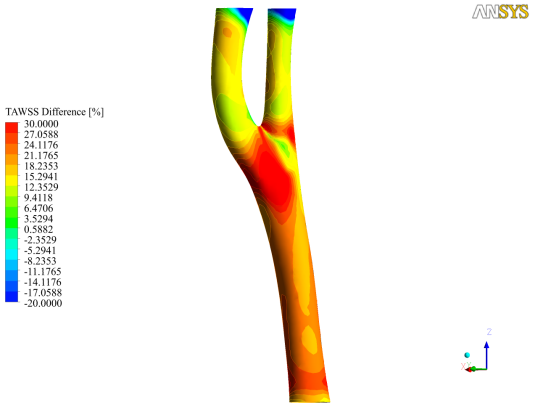

(e) Difference(%) Anterior

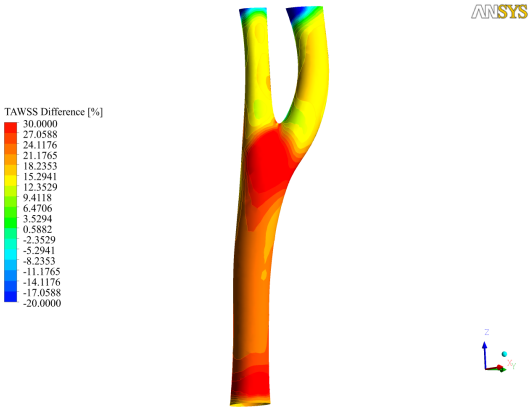

(f) Difference(%) Posterior

Figure 69: Comparison of time averaged Wall Shear Stress in subject 1

the majority of the CCA and other parts of the ICA/ECA, (excluding the beginning of bifurcation around proximal to each entrance of the ICA/ECA) follows the same trend in subject 1 in which wall distensibility decreases TAWSS by comparison to the rigid body model by $20 \sim 30$ % (Fig. 70). For subject 2, high TAWSS of the FSI case compared with the rigid model around the stenosis can be accounted for by the effect of tortuous curvature of the ICA and the development of IMT. This WSS profile is also observed in subject 3 in which there is a relatively severe stenosis around the junction of CCA and ICA and a lesser stenosis around the CCA and ECA (Fig. 74). Just distal to the stenosis, negative values for the difference of TAWSS are present, and this means that in the FSI model, TAWSS of this site is higher than the rigid body case. In this subject, at the side of stenosis which experiences the most deformation of the arterial wall (Fig. 49), TAWSS of the rigid body model is reduced by $20 \sim 30\%$ consistent with subjects 1 and 2. However, the majority of the CCA and most areas of the ICA and ECA exhibit around $10 \sim 15\%$ reduction of TAWSS. The relatively small reduction of TAWSS can be explained by high wall thickness of this subject. On the other hand, with subject 1 and 2, IMT develops in the CCA and most of the ICA/ECA, including the junction of CCA and ICA/ECA. This hinders the expansion of the arterial wall and thus the difference of TAWSS of two cases shows relatively slight change, in contrast with the other subjects.

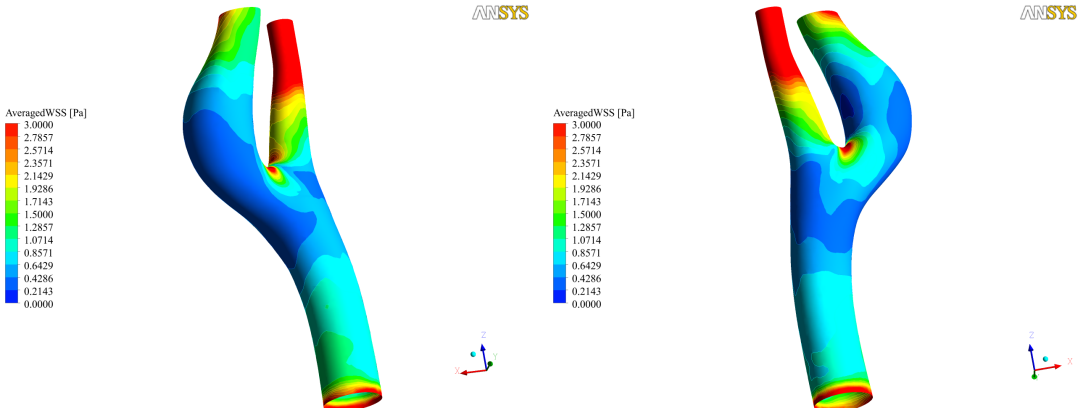

(a) FSI Anterior

(b) FSI Posterior

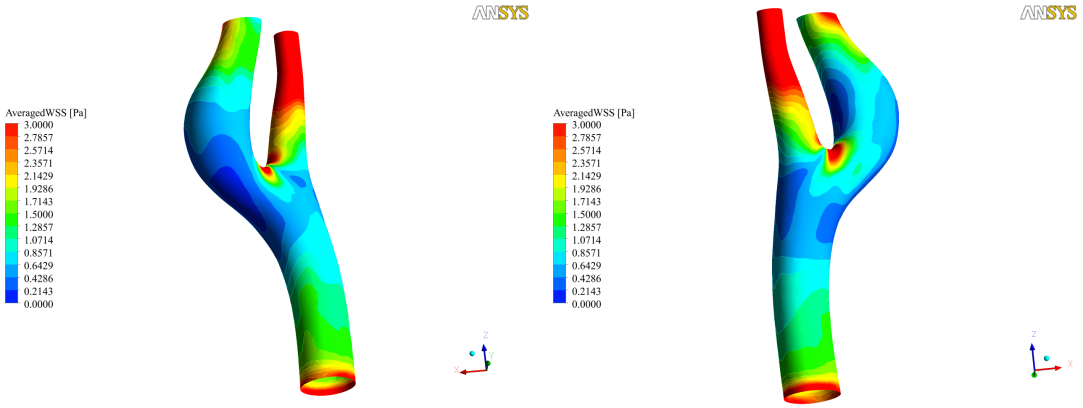

(c) Rigid Anterior

(d) Rigid Posterior

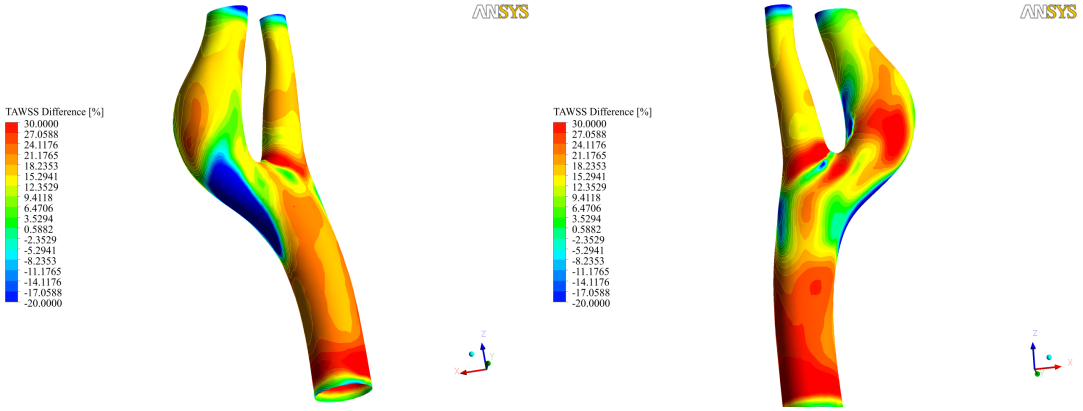

(e) Difference(%) Anterior

(f) Difference(%) Posterior

Figure 70: Comparison of time averaged Wall Shear Stress in subject 2

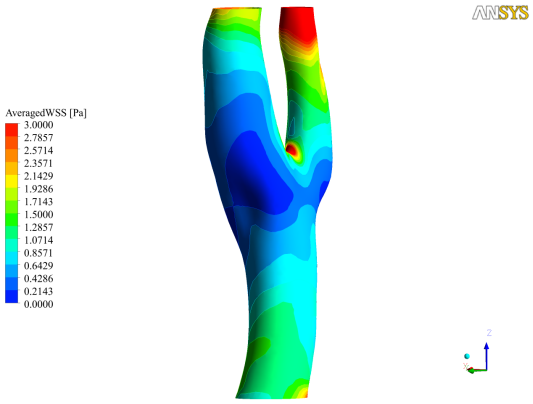

(a) FSI Anterior

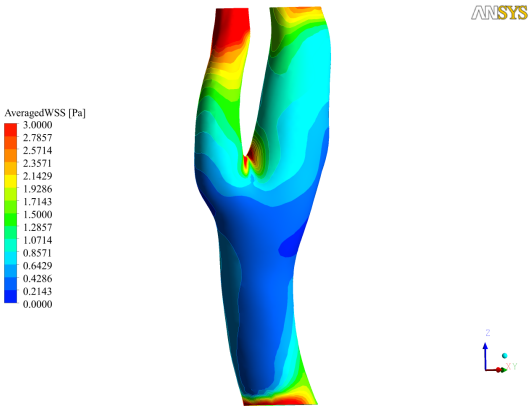

(b) FSI Posterior

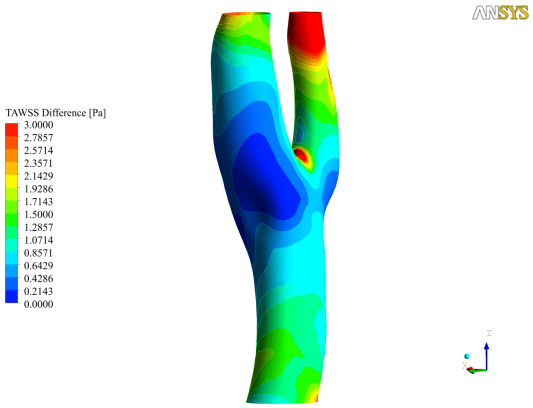

(c) Rigid Anterior

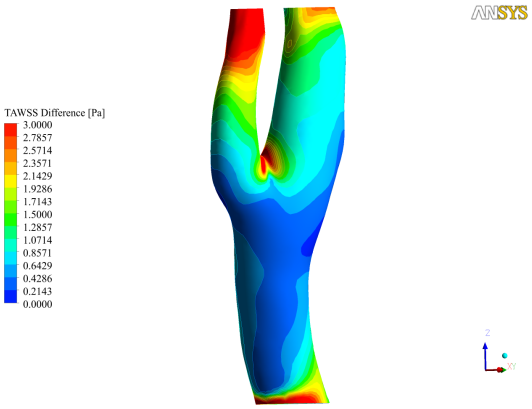

(d) Rigid Posterior

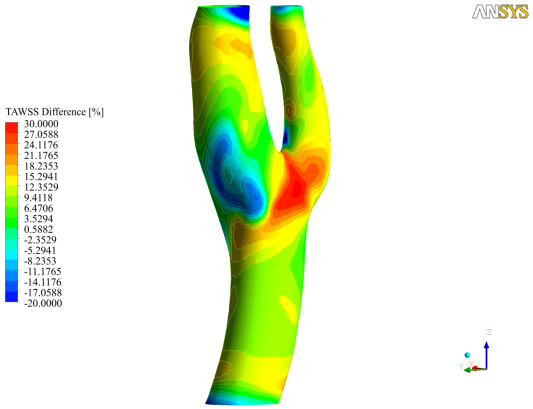

(e) Difference(%) Anterior

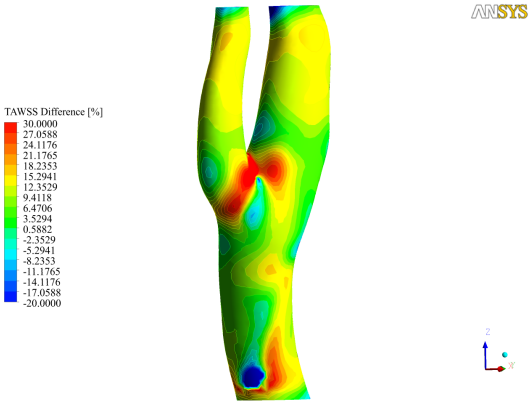

(f) Difference(%) Posterior

Figure 71: Comparison of time averaged Wall Shear Stress in subject 3

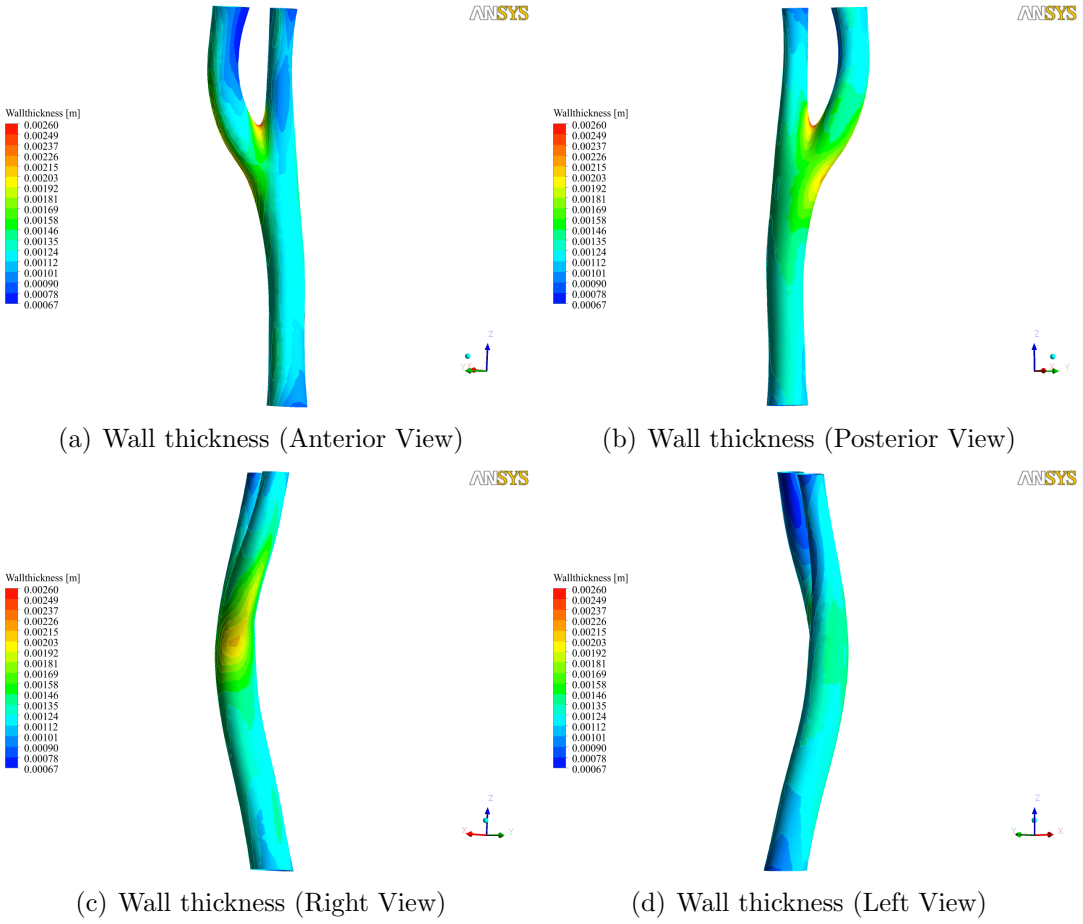

(a) Wall thickness (Anterior View)

(b) Wall thickness (Posterior View)

(c) Wall thickness (Right View)

(d) Wall thickness (Left View)

Figure 72: Wall thickness in subject 1

5.2.2 Wall thickness

Wall thickness is calculated in a way similar to that is used to obtain the radius from the centerline of the shrinkage process in chapter 4. Based on the grid points on the inner wall, the shortest length is determined by comparing the distance from inner wall grid points to outer wall. This shortest distance is chosen as the definition of wall thickness, and this value is visualized based on the inner wall at diastole state in Figs. 72 $\sim$ 74.

The measurements in healthy human subjects by Zhao et al. [106] indicate the range of wall thickness of the CCA to be around $0.6 \sim 0.8mm$, which is 10% of the

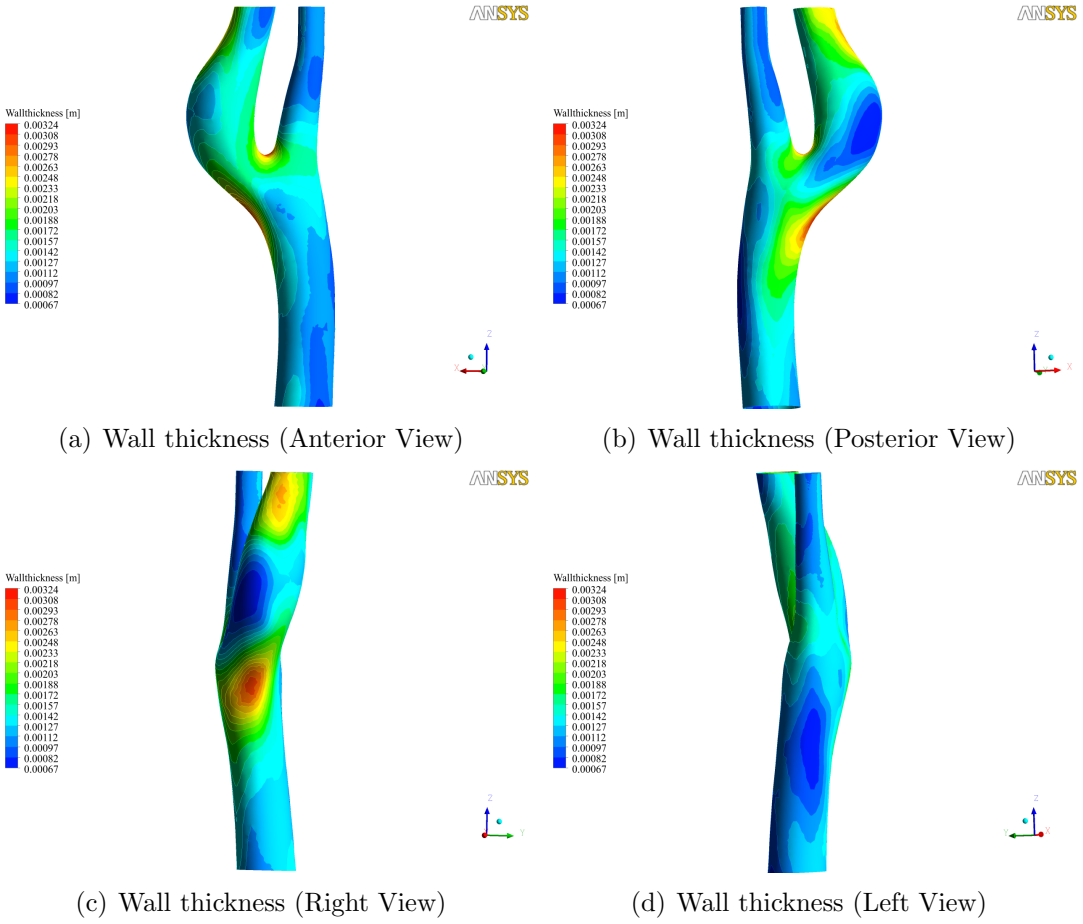

(a) Wall thickness (Anterior View)

(b) Wall thickness (Posterior View)

(c) Wall thickness (Right View)

(d) Wall thickness (Left View)

Figure 73: Wall thickness in subject 2

diameter of common carotid artery. However, depending on individual, the distribution of wall thickness may vary from this value, and in general being larger with older subjects. The research of Steinman et al. [84] using black blood MRI to construct in-vivo artery reveals that wall thickness in most of the CCA is around $1mm$ and at the junction of the CCA and ICA/ECA, except for the stenosis, wall thickness increases to $1.5 \sim 2mm$ in the human carotid artery. This wall thickness (WT) distribution is in consistent with observations in our research.

In subject 1, WT in the majority of the CCA and ICA/ECA is in the range of 0.6 to $1.0mm$, however, obvious IMT progression is found ($2.0mm$) at the junction of the CCA and ICA proximal to the entrance of ICA (Fig. 72 (c)). Wall thickness increases somewhat at the beginning of the bifurcation on both anterior and posterior

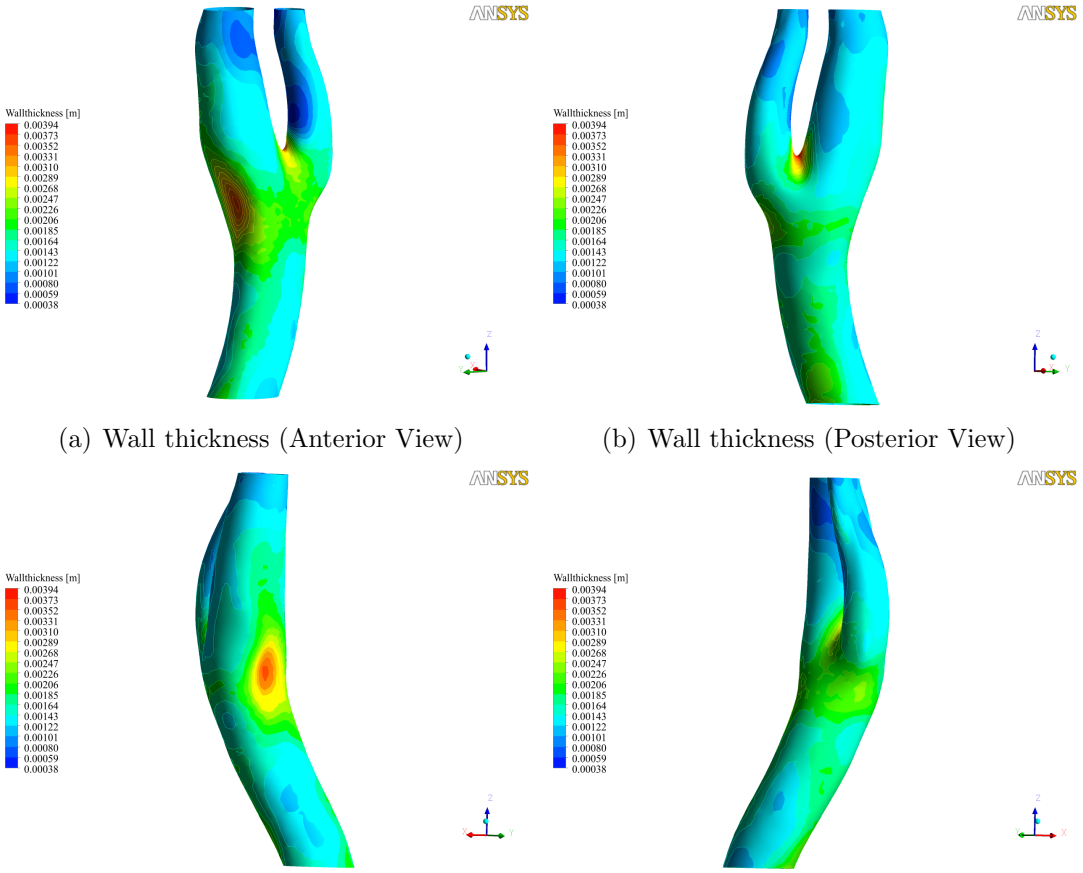

(a) Wall thickness (Anterior View)

(b) Wall thickness (Posterior View)

(c) Wall thickness (Right View)

(d) Wall thickness (Left View)

Figure 74: Wall thickness in subject 3

sides of this subject. In subject 2, a mild stenosis is present at the entrance of the ICA around the junction of the CCA and ICA, and it increases up to $3.2mm$. Due to geometrical features of this subject, in which there is a tortuous curvature in the ICA, IMT progression is more dominant around the beginning of bifurcation and in the ICA, including the stenosis. Except for the aforementioned segments the wall thickness is in the range of $0.6mm$ to $1.0mm$.

In subject 3, the curvature in the CCA induces asymmetrical flow patterns and these lead to LWSS on the posterior side of the CCA (Fig. 56). For this reason, in contrast with subjects 1 and 2, high wall thickness is observed at this site. The majority of the carotid artery except for the ECA and a small portion of the ICA and CCA is over $1.5mm$ in wall thickness. The most severe stenosis ($4.0mm$) in our

research is present at the entrance of the ICA. And mild stenosis is found at the entrance of the ECA which is not observed in other subjects in this research.

5.2.3 Mass and volume flux

To obtain the volume flux through leaky junctions, the fraction of leaky junction needs to be determined from local wall shear stress (WSS). In our research WSS is extracted from TAWSS of the FSI model. Using the suggested approach by Olgac et al. [65] (Eqn. (16)), the fraction of leaky junction (ϕ) is obtained from TAWSS on the luminal surface, and mass and volume flux is calculated based on ϕ and is visualized in Figs. $75 \sim 77$.

Over the majority of the carotid artery, the overall volume flux (J_v) is in the range between $1.0 \times 10^{-8} \sim 2.0 \times 10^{-8}\ ms^{-1}$ in subject 1, except for IMT progression regions because the resistance to the transmural flow of plasma is dependent on the wall thickness (Fig. 68). This range seems acceptable based on measurements by Meyer et al. [58]. In their study, the volume flux of a straight segment of rabbit thoracic aorta was observed, and they found the filtration was $1.78 \times 10^{-8}\ ms^{-1}$ when the luminal surface was pressurized by $70mmHg$. This range is also supported by the theoretical research with a multi-layered model by Prosi et al. [68]. They showed that when the pressure difference between the endothelial surface and the interface of the media and adventitia is $70mmHg$, the corresponding filtration flow is $1.76 \times 10^{-8}\ ms^{-1}$.

In subject 2, the pattern of total filtration is similar to subject 1. Except for the stenosis and IMT development regions, the overall filtration (J_v=$J_{v,lj}$+$J_{v,nj}$) is in the range between $1.0 \times 10^{-8} \sim 2.0 \times 10^{-8}\ ms^{-1}$. Most of all, the maximum filtration value ($2.82 \times 10^{-8}\ ms^{-1}$) in this subject is very similar to the measurements conducted by Tedgui et al. [92] in which the total transmural flow is $2.8 \times 10^{-8}\ ms^{-1}$ when the rabbit aorta was pressurized by $70mmHg$ intraluminal pressure. However,

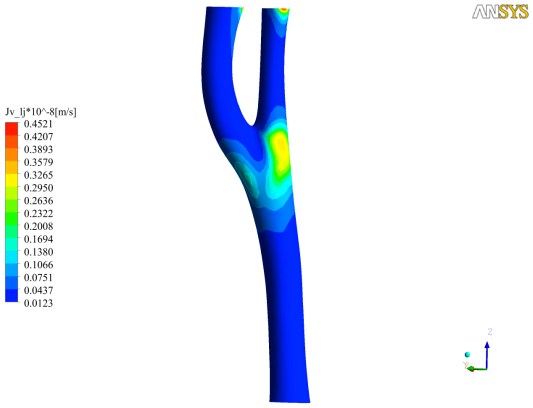

(a) Volume flux through leaky junctions (Anterior View)

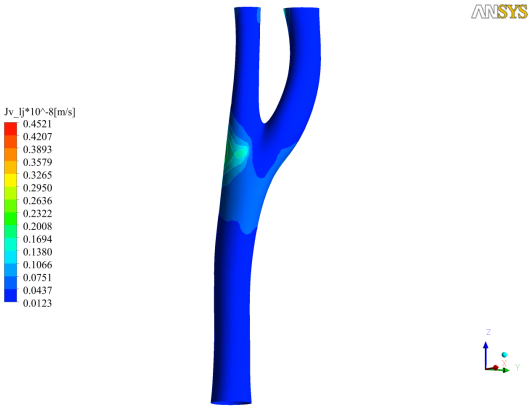

(b) Volume flux through leaky junctions (Posterior View)

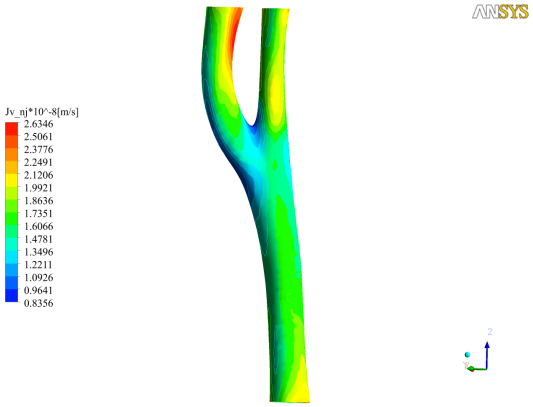

(c) Volume flux through normal junctions (Anterior View)

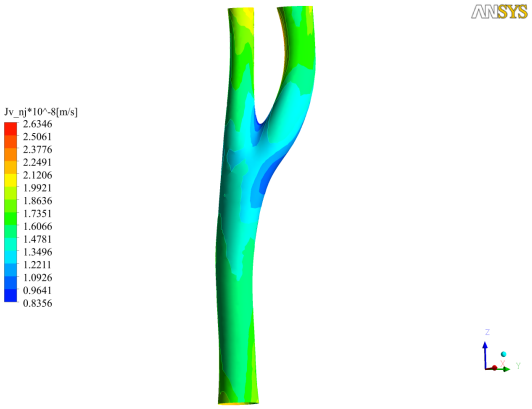

(d) Volume flux through normal junctions (Posterior View)

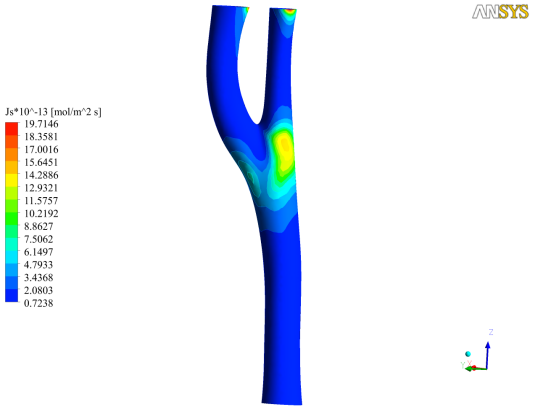

(e) Mass flux on the endothelium (Anterior View)

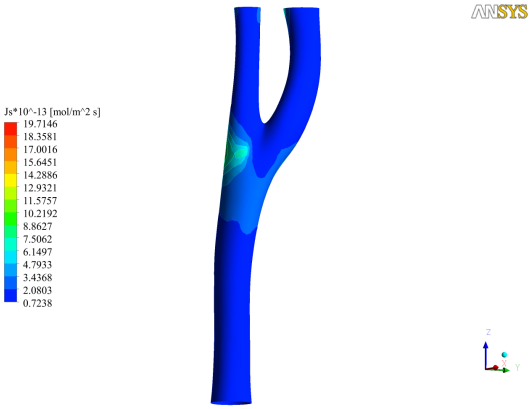

(f) Mass flux on the endothelium (Posterior View)

Figure 75: Mass and volume flux into the endothelium of subject 1

the total filtration flow in the majority of the carotid artery in subject 3 is lower and in the range between $1.0 \times 10^{-8} \sim 1.5 \times 10^{-8}\ ms^{-1}$. This can be explained by the greater IMT development in this subject which acts as increased resistance to plasma flow in the arterial wall.

The filtration flow through the leaky junctions is meaningful to LDL particles passing through the endothelium because the majority of LDL is carried with the convective filtration flow caused by the pressure gradient, except for a small portion of transcytosis contribution to LDL movement. For this reason it is necessary to separate the plasma flow through each pathways, i.e., cleft in the normal junctions and leaky junctions, which are induced by cell death or proliferation. In Fig. 75, the volume flux via normal ($J_{v,nj}$) and leaky junctions ($J_{v,lj}$) and mass flux (J_s) which is related with the volume flux via leaky junction is visualized in subject 1. The region experiencing high volume flux via leaky junctions is limited to a small region proximal to ECA entrance. This can be explained by the size of LWSS region. The geometry of this carotid artery is relatively simple compared with subjects 2 and 3, and this leads simpler flow patterns. The simpler flows also result in a higher TAWSS over most of the luminal surface except for the aforementioned site (Fig. 69).

By comparison of the pattern of J_s and $J_{v,lj}$ in each subject, it is convincing that the overall apparent permeability Pe_{app} is decided by the leaky junction formation and the volume flux through this pathway because the distributions of these parameters are similar in carotid artery. In other words, at low WSS regions the increase of apoptosis and mitosis rate extends the formation of leaky junctions. Accordingly, more LDL particles can enter into the intima via this gap; and finally, this phenomenon is represented by the increase of the permeabiltiy of endothlelium to LDL. The magnitude of mass flux and its distribution is very different in each subject. Mass flux proximal to the ECA entrance in subject 1 is $14.0 \times 10^{-13}\ mol/m^2{\cdot}s$ (Fig. 75 (e)), which is half of the value compared with subjects 2 and 3. In subject 2, max-

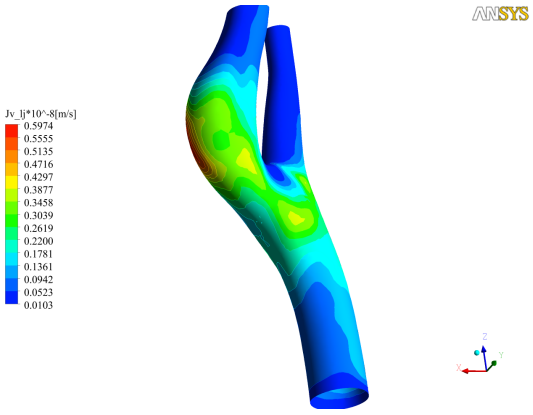

(a) Volume flux through leaky junctions (Anterior View)

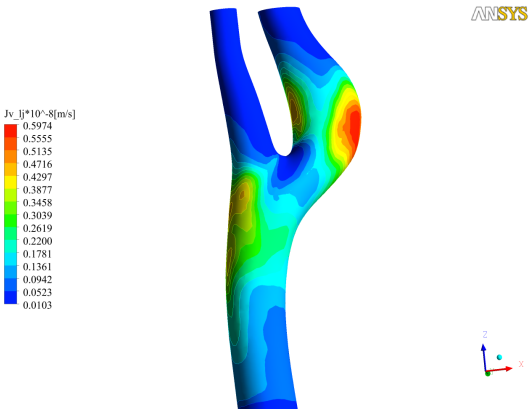

(b) Volume flux through leaky junctions (Posterior View)

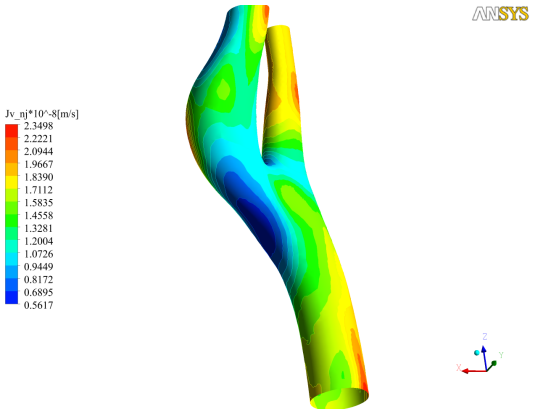

(c) Volume flux through normal junctions (Anterior View)

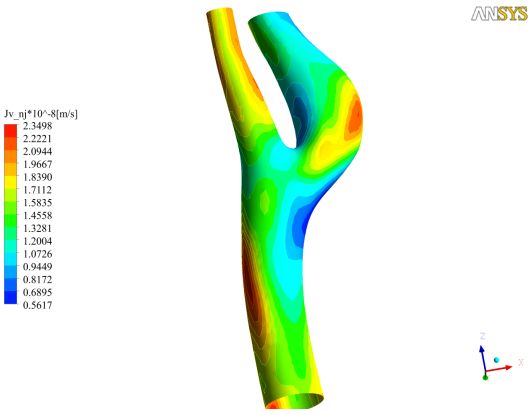

(d) Volume flux through normal junctions (Posterior View)

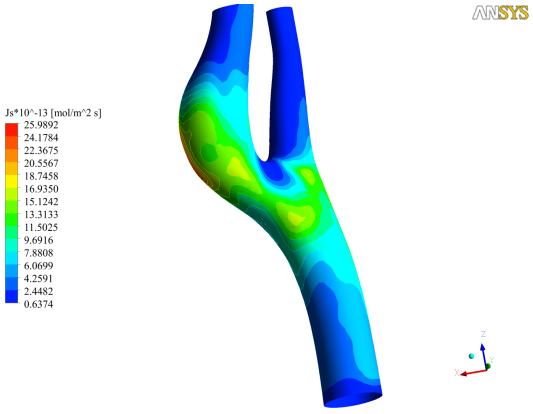

(e) Mass flux on the endothelium (Anterior View)

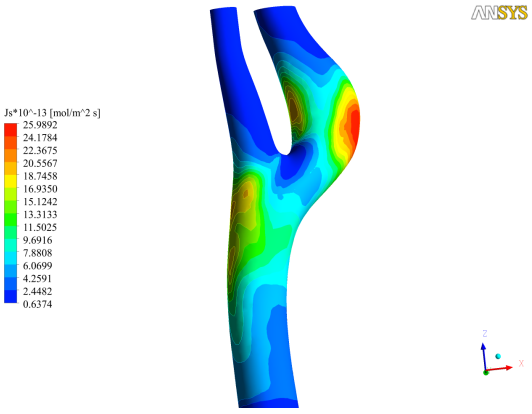

(f) Mass flux on the endothelium (Posterior View)

Figure 76: Mass and volume flux into the endothelium of subject 2

imum mass flux is observed in the carotid bulb distal to the stenosis (26.0×10^{-13} $mol/m^2 \cdot s$) and most regions of the carotid bulb and the junction of the CCA and ICA/ECA are subjected to high mass flux of LDL particles. This region is coincident with low TAWSS regions in Fig. 70 and is similar to the distribution of the volume flux via leaky junctions. The distribution of the volume flux via normal junctions ($J_{v,nj}$) exhibits the role of wall thickness as the major resistance to the flow. As seen in 2D stenosis model (Fig. 68), $J_{v,nj}$ is reduced rapidly at the stenosis region due to the dominant role of cleft in normal junctions to pass plasma fluid (Figs. 76, 77).

In subject 3, maximum mass flux is less than in subject 2 because IMT developed more than in subject 2; however, the region experiencing high mass flux is largest, including carotid bulb, the junction of the CCA and ICA/ECA and the posterior side of the CCA. Severe curvature in the CCA creates asymmetric flow patterns and this leads the posterior side of the CCA to be exposed to low TAWSS. Geometrical non-planarity and the area expansion at the junction of the CCA and ICA/ECA also induce the formation of low TAWSS (Fig. 71). The enhancement of the volume flux via leaky junctions by low WSS leads to the increase of the apparent permeability (Pe_{app}) at this site, and accordingly high mass flux can be observed in Fig. 77 (e), (f).

The research done by Sang et al. [74] tested which hemodynamic wall parameters (HWP) had the best potential to predict endothelial dysfunction using subject specific CFD with MRI from 50 normal carotid arteries. It was found that among these indicators excepting RRT (relative residence time which is actually inversely related to TAWSS), TAWSS is a basic indicator related to other HWP and is recommended as a standard of measurement to predict regions prone to plaque formations. However, TAWSS alone is not enough to indicate which areas will progress and enlarge the plaque formation in FSI model because low TAWSS of FSI simulation covers most part of bifurcation junction including the stenosis which occurs at the entrance of the

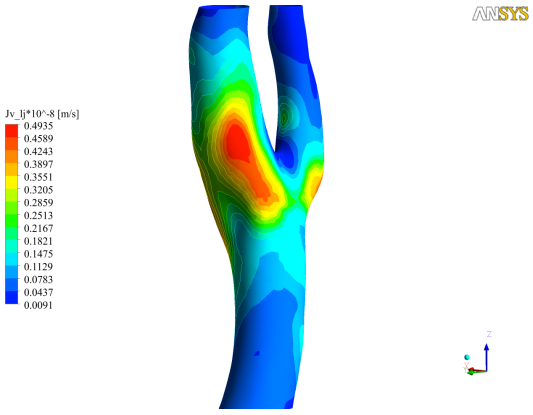

(a) Volume flux through leaky junctions (Anterior View)

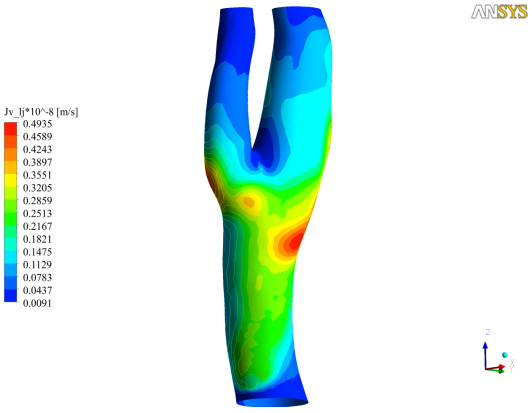

(b) Volume flux through leaky junctions (Posterior View)

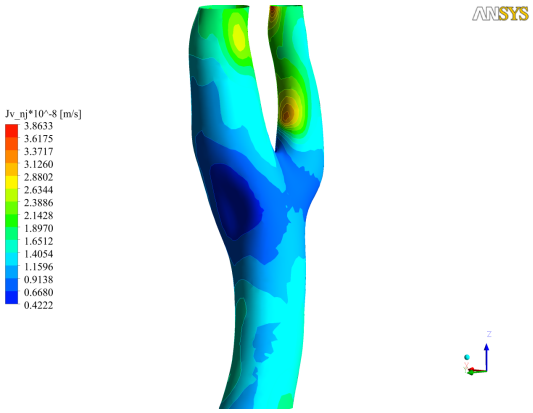

(c) Volume flux through normal junctions (Anterior View)

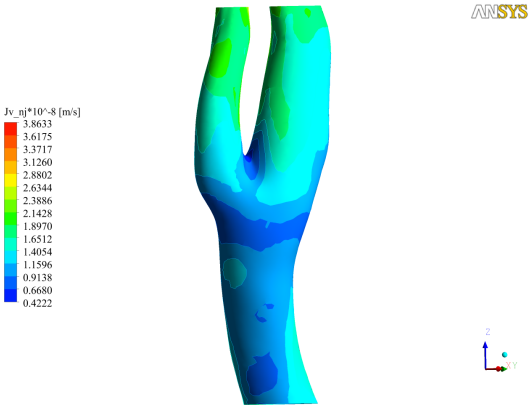

(d) Volume flux through normal junctions (Posterior View)

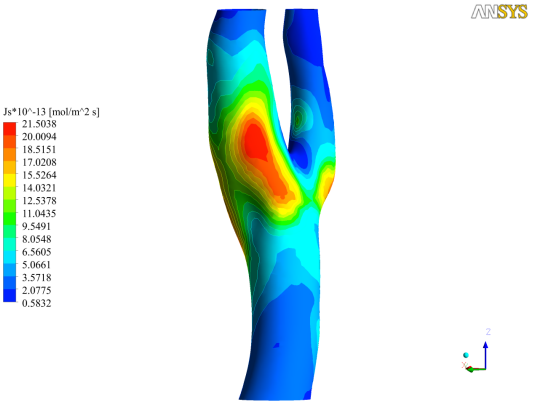

(e) Mass flux on the endothelium (Anterior View)

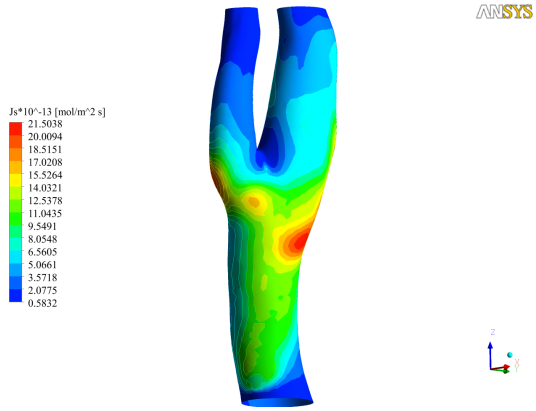

(f) Mass flux on the endothelium (Posterior View)

Figure 77: Mass and volume flux into the endothelium of subject 3

ICA and ECA and extends into the CCA regions [84]. TAWSS distribution in our research is consistent with this pattern. In subject 2 and 3, low TAWSS regions also cover the majority of carotid bulb and the junction of the CCA and ICA/ECA and spread over the stenosis, extending to most of the posterior side of the CCA (Figs. 70, 71). The insufficiency of TAWSS as indicator is supported by the clinical observation by Smedby et al. [79], in which most of atherosclerotic plaque progression is found in the downstream of the stenosis in human femoral arteries. Based on the findings in our subjects, mass flux may be a predictor to show the plaque formation in the artery because it deals with direct LDL particle movement through the endothelium and maximum mass flux is present distal to the stenosis in the carotid bulb and it is also found proximal to the ECA entrance, which is the site immediately distal to the mild stenosis in subject 3 (Fig. 74). On the basis of the fact that high mass flux leads high concentration of LDL in the intima and media, it could be predicted that maximum mass flux regions should have the most possibility of the enlargement of plaque formations and growth into the downstream direction.

CHAPTER VI

IMPLEMENTATION OF POROELASTICITY OF BLOOD VESSEL WALL TO CALCULATE THE PORE FLUID FILTRATION

6.1 Evaluate poroelasticity for 2D simple carotid artery case and compare with previous research results

6.1.1 Introduction

In the arterial wall, interstitial flow of plasma transports LDL particles. Plasma flow is determined by the pressure gradient between the luminal surface and the interface of the media-adventitia and the resistance of the matrix structure forming a porous medium in the artery wall, which is represented by the structural permeability. In experimental studies, arterial tissue is typically pressurized with constant intraluminal pressure for a period of time, and the interstitial flow is measured when steady state is reached. For this reason, the calculation of filtration flow in many studies is simplified as a model with constant permeability without consideration of arterial deformation by the pressure alteration in a cardiac cycle. Therefore, the direction of the filtration flow is always from the lumen to the arterial wall in steady state with same magnitude across the vessel wall.

However, the interstitial flow responds dynamically with pressure changes in arterial wall, and this flow variation was illustrated in investigations by Avinash et al. [4] and Koshiba et al. [49]. It is found that filtration flow near the luminal surface exhibits variations in magnitude and direction of velocity. Although the directional change is not seen in steady state, the direction of filtration flow changes suddenly from the arterial wall to lumen in a cardiac cycle when the mechanical stress of the

structure is coupled with transmural pore pressure of interstitial flow using porohyperelasiticity.

To implement the dynamic response of filtration flow in the carotid artery an idealized 2D cross section of a human common carotid artery was constructed, and computations were performed using a poroelastic model to capture filtration flow patterns in the luminal surface and in the arterial wall imposing a generic intraluminal pressure curve.

6.1.2 Background and methods

Blood vessels can be treated as porous media fully saturated with plasma because the arterial structure consists of a fiber matrix, i.e, elastin, proteoglycan and collagen. The fluid in the pore interacts with arterial matrix stress and strain through the fluid pore pressure in response to matrix deformation caused by external forces. In general, the hydro mechanical coupling between filtration flow and matrix deformation can be formulated according to poroelasticity theory [4, 49, 78].

The force equilibrium is a fundamental equation to describe the physics, and includes the fluid pressure impact the structure through an effective stress concept; must

$$\begin{aligned} -\nabla \cdot \sigma_{total} &= F \\ \sigma_{total} &= \sigma^{'} + \alpha P \\ -\nabla \cdot \sigma_{total} &= F - \alpha \nabla \cdot P \end{aligned} \tag{17}$$

where, σ_{total} is total stress and F is external force. Total stress consists of the effective stress, σ', of the matrix structure and the pore pressure, P. The parameter, α, is a Biot-Willis coefficient which can be interpreted physically as the ratio of increment of fluid content added to storage divided by the change in bulk volume under the constraint that pore pressure remains constant. The constant pore pressure condition means that the volume of fluid that goes into or out of storage is equal to the

change in pore volume only. In the artery, both the solid component of the matrix structure and the plasma fluid in the pore are treated as incompressible, thus the Biot-Willis coefficient must be one. In Eqn. (17) there is no dynamic term to account for a transient structural case. However, this equation can be utilized in transient simulation. In general, the time scale of the structural response is much faster than the time scale of flow by several orders of magnitude. When the filtration flow is calculated in an arterial structure, it can be assumed that the solid component of the vessel reaches the equilibrium state immediately in the response to the flow condition at each time step.

The filtration flow caused by geomechanical deformation is described by Darcy's law in which the flow rate is determined from the pressure gradient multiplied by the permeability of solid matrix. General Darcy's law is defined as:

$$q_{poro} = -\frac{K_D}{\mu_{plasma}} \nabla (P + \rho_{plasma} g z) \tag{18}$$

where, q_{poro} is the flow rate in the porous media, K_D is the permeability of the solid matrix, and μ_{plasma} is the dynamic viscosity of the pore fluid. The effect of gravitational force on the filtration flow in matrix structure is negligible. Inserting the simplified Darcy′s law into the continuity equation produces the generalized governing equation:

$$\frac{1}{M}\frac{\partial P}{\partial t} - \nabla \cdot (\frac{K_D}{\mu_{plasma}} \nabla P) = -\alpha \frac{\partial (\nabla \cdot u)}{\partial t} \tag{19}$$

$$\frac{1}{M} = \frac{\alpha - \phi}{K_s} + \frac{\phi}{K_f} \tag{20}$$

where, M is the Biot modulus, K_s and K_f are the bulk modulus of the solid and the pore fluid, respectively. In the artery, both solid and fluid are incompressible, so Biot modulus becomes infinite. The pore flow in the blood vessel can be implemented by

the balance between Darcy's law and the rate of change of volumetric strain due to solid deformation in Eqn. (19).

The matrix structure consisting of collagen, elastin and proteoglycan (PG) is deformed by external force, and this deformation hinders the pore fluid flow in the porous media. This is observed by the hydraulic conductivity variation with or without the existence of intima in experimental studies. The hydraulic conductivity of vessel wall responds nonlinearly with the increase of applied external pressure in the intact artery; but when the intima was denuded, only the media remains, and the overall filtration flow increases linearly as intraluminal pressure becomes higher. The ratio of the filtration flow and the pressure change can be interpreted as the permeability of the porous media. Hence, the media permeability is relatively unchanged with intraluminal pressure; however, compared to the media, the permeability of the intima changes with blood pressure because the compaction of the intima reduces the volumetric space of the pore fluid and the decrease of pore space acts as the hindrance to interstitial flow [42, 78]. To implement the compaction of intima, the permeability function depending on the volumetric strain of arterial structure is employed based on the form suggested by Homes et al. [39] in which the Darcian permeability (K_D) is a function of volumetric strain and the initial porosity of matrix.

$$K_D = K_0(\frac{J_{vol} - 1 + \phi_0}{\phi_0})^2 exp^{m[J_{vol}^2 - 1]/2} \tag{21}$$

where, K_0 is a Darcian permeability at zero strain state and ϕ_0 is the initial porosity. m is a parameter that comes from the observation that the permeability is an exponential function of the compressive strain and is set as 4. This function makes the permeability change dramatically with the small volumetric ratio. Due to the lack of experimental information about K_0 in the human carotid artery and the variation of this parameter depending on the species and the part of the circulation, the measured hydraulic conductivity ($2.0 \times 10^{-14} cm^2$) of the human aortic wall at $77.5 mmHg$ [101] is assigned as the media permeability, and from this value the nonlinear permeability

of the intima is calculated with the change of volumetric ratio.

6.1.3 2D common carotid artery

Making use of symmetry, the quarter segment of a 2D duct is scaled to dimensions of human common carotid artery in which the inner radius set up as $3mm$ and the outer radius as $3.6mm$, as shown in Fig. 78. Thus, the vessel wall thickness is $0.6mm$, a value in the typical range for human carotid arteries. Vessel structure is separated into two parts in which the intima is assigned near the inner wall and the remaining arterial wall is treated as the media. The media comprises most space of the blood vessel, so it is natural that the media domain supports the external loading. Hence, the mechanical response of the arterial wall is determined by the media structure. In contrast, the mechanical response of intima is negligible even though it is a critical structure to lead the filtration flow pattern change with the volumetric deformation due to being a more flexible structure than the media. The vessel structure is treated as a homogenized isotropic elastic tube with $0.3MPa$ Young's modulus and $1366kg/m^3$ density. The pore fluid is incompressible with $1000kg/m^3$ density and $7.2 \times 10^{-4} Pa{\cdot}s$ viscosity [25]. A typical pressure curve for a commmon carotid artery (Fig. 18) is applied on the inner wall surface of the idealized human carotid artery model as the external force and this pressure also is applied to the pore fluid pressure, on the surface, and on the outer wall surface zero pressure is applied as a boundary condition to the structure and pore fluid to cause the filtration flow to move freely.

The governing equations of hydro-mechanical coupling were implemented by a commercial FEM program, Comsol Multiphysics 4.1. Using Darcy's module and the solid mechanics module the coupling model was set up manually. Mechanics-fluid coupling was done by including the pressure gradient as the initial stress in the general solid mechanics module (Eqn. (17)). The volume ratio from stress and strain

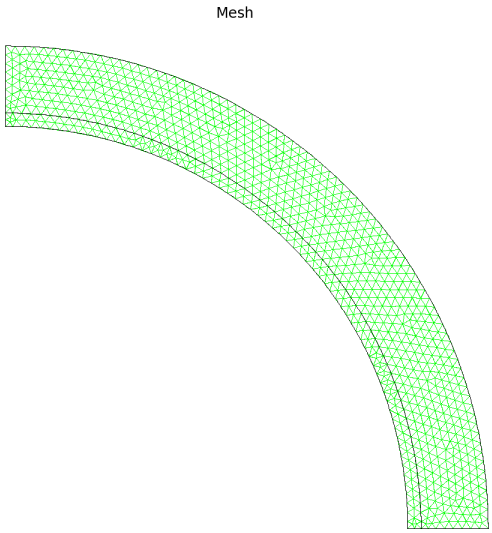

Figure 78: 2D Carotid Artery and Mesh

calculation was assigned to Darcy's module as a source term to implement the fluid-mechanical coupling (Eqn. (19)). For poroelastic multiphysics simulation, a direct method was utilized with 0.001 time step size.

In the direct method, it is critical to assign the proper boundary and initial conditions because the combination of these conditions at the beginning of calculation makes it available as the calculation progresses without extra nonlinear iterations to the next time point, thus saving computational time and giving the stability. For this reason, the pore pressure and structure had no value at the starting point and the intraluminal pressure was also applied with zero pressure and increased to diastole pressure in the first cardiac cycle. After a smooth pressure increase from zero to diastolic pressure in the first cardiac cycle, the pressure alternated from diastole to systole pressure in the remaining cardiac cycles. Due to the zero stress and strain state in the matrix structure and pore fluid at the beginning of the simulation, it is found that unrealistic flow patterns are observed at the initial state. Thus, the time span of calculation was extended from 0 to $45s$ to examine the filtration flow pattern change with time. In Fig. 79, the filtration flow which is measured at luminal surface

reaches unrealistically high values at the beginning of calculation and decreases gradually. Finally, however, it reaches a state in which the filtration flow shows a regular pattern with the blood pressure curve.

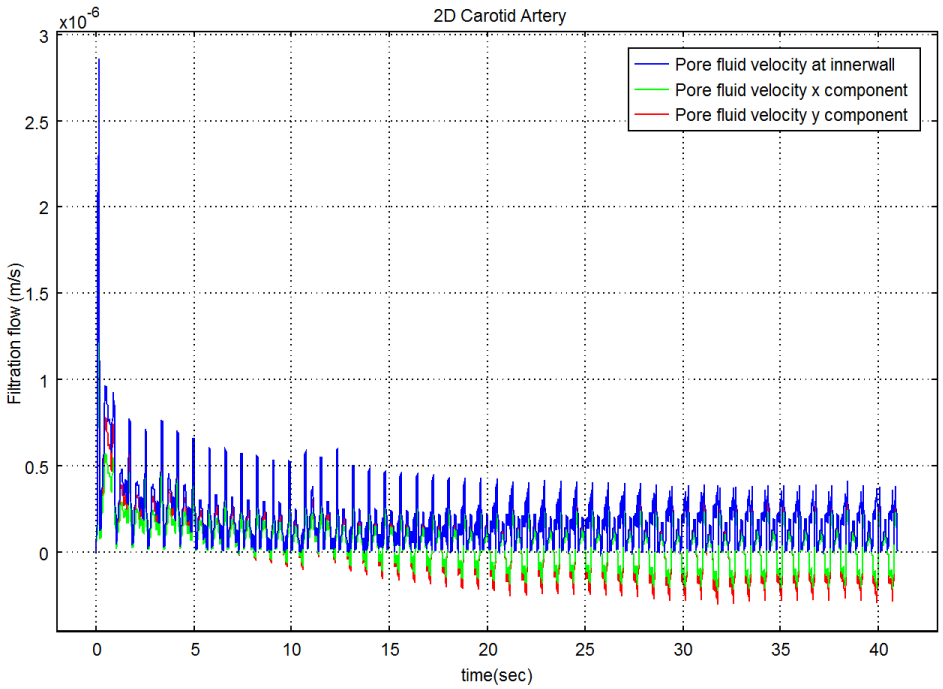

Figure 79: Stabilization of pore fluid flow

6.2 Results and Discussion

In Fig. 80 (a), the deformation of the arterial wall by blood pressure is presented by the curve of the displacement of the inner wall; and this result confirms that the pressure leads the proper deformation of the arterial wall by the fact that the maximum displacement ($0.6mm$) of the inner wall between minimum and maximum pressure state is in the range of normal human carotid artery's radius change.

In Fig. 79, after $15s$ in time span of simulation, the filtration flow shows negative values in x and y components; and subsequently negative values develop further and reach a regular pattern with the pressure curve. A more detailed diagram is shown in Fig. 80 (b). The x and y components of pore fluid change from plus to minus

in a cardiac cycle. In the calculation if the direction of velocity of pore flow is from the lumen to arterial wall, the x and y components of velocity show positive values, however, in the opposite direction, x and y components becomes negative (Fig. 80 (d)). This can be explained by pressure distribution in arterial wall because, in the poroelastic method, the filtration flow is obtained by the pressure gradient and the permebility of matrix structure, therefore, the flow pattern from vessel wall to the lumen means that the luminal surface pressure is less than that in the wall at any time in a cardiac cycle. This is confirmed by the pressure pattern in Fig. 80 (c) in which maximum pressure is presented below the luminal surface and this pressure gradient leads reverse velocity vector (Fig. 80 (d)). This pressure distribution can be seen only in transient case in conjunction with arterial deformation. Without arterial deformation, even with transient simulation, reverse flow in the pore is not observed.

In the steady state situation, the measurement of filtration flow shows the velocity is almost the same across the wall. However, in the transient model, most variation in the direction and magnitude is found at luminal surface and a very thin layer of vessel wall. Going further into the arterial wall, pore flow velocity decreases suddenly because the low permeability of arterial matrix structure hinders the flow movement. This suggests the possibility that biochemical particles, such as LDL, stay longer in a very thin layer with loosing the filtration flow convective force rapidly going deeper into the vessel wall. Therefore, it can support the fact that LDL particles have more chance to interact with macrophages in the intima and transform to oxdized LDL (ox-LDL) by the combination with ROS.

The separation of intima and media in-vivo is difficult due to the lack of image quality of BBMRI. However, it is still necessary to include the structural compaction of the intima by external pressure. For this reason, based on the above physical characteristics of pore fluid flow in the matrix structure of the carotid artery, non linear

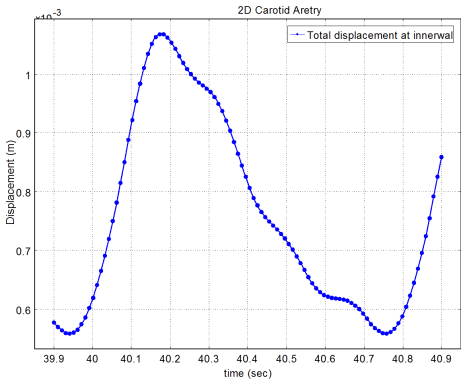

(a) Displacement

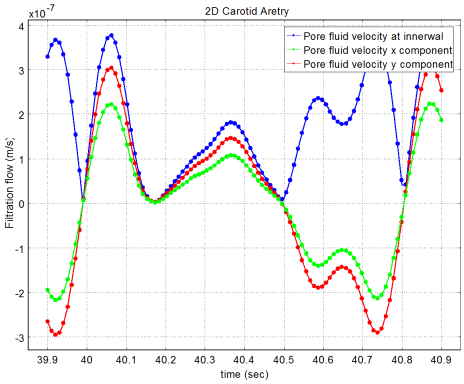

(b) Pore filtration flow at the surface

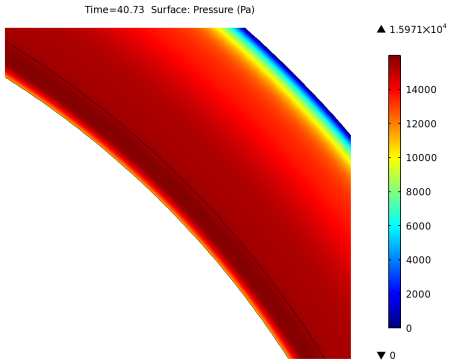

(c) Pressure

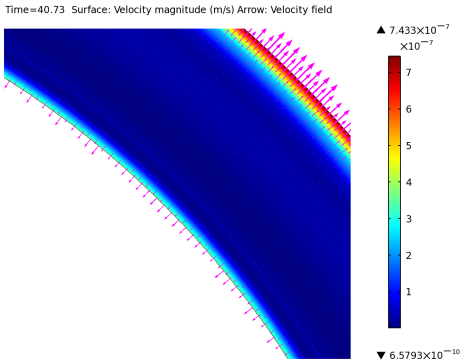

(d) Reverse Pore filtration flow

Figure 80: Nonlinear permeability applied to only the intima. (a) Displacement of the vessel wall in a cardiac cycle. (b) Pore flow pattern at the surface of vessel wall. (c) Pore pressure distribution at maximum reverse pore flow. (d) Pore fluid distribution at maximum reverse pore flow

permeability of the matrix structure is assigned to the entire structure and the filtration flow change is examined through a comparison with non linear permeability only for the intima case. Any differences cannot be detected in the mechanical structure response to intraluminal pressure through the comparison of the displacement (Fig. 80 (a) and Fig. 81 (a)). A similar mechanical response could be expected in both cases because the contribution of pore fluid flow to the overall mechanical response is negligible. At the surface, filtration flow patterns show the same trend in non linear permeability only in the intima case, even though there is a very slight magnitude

decrease in filtration flow. The reduction of velocity comes from the increase of hindrance to pore fluid flow in the media. Except this, the transmural fluid filtration pattern is similar to previous case. As a result, this suggests that in a 3D subject geometry the entire structure can be treated as having nonlinear Darcy's permeability to include the effect of compaction in intima structure without the separation of intima and media.

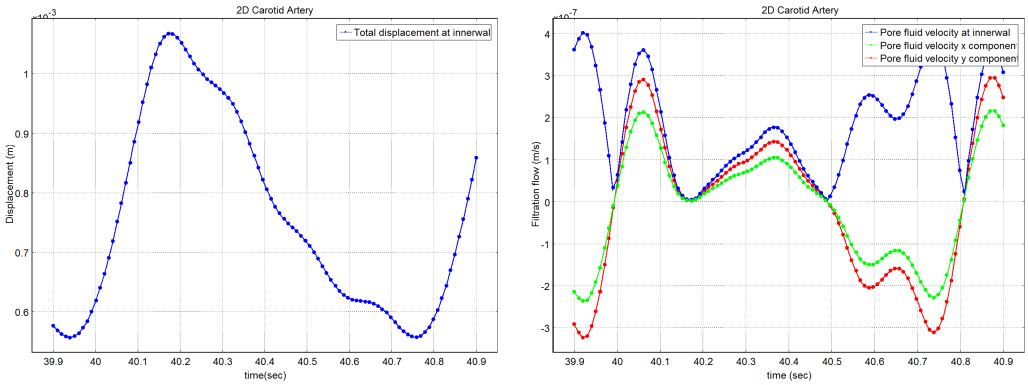

(a) Displacement

(b) Pore filtration flow at the surface

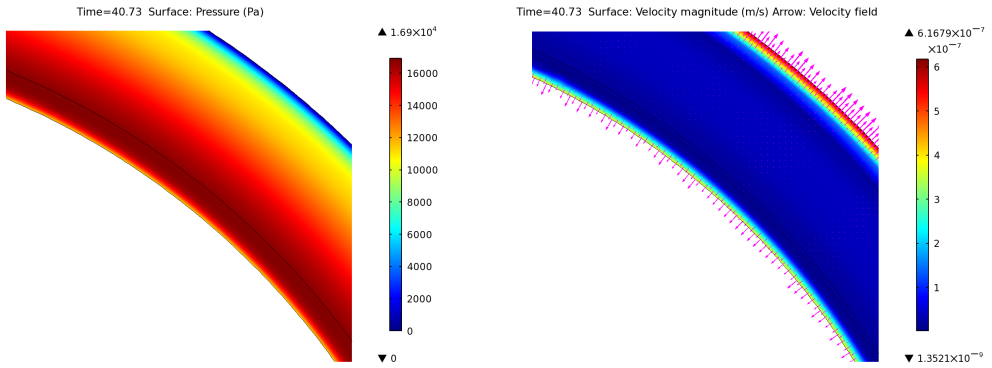

(c) Pressure

(d) Reverse Pore filtration flow

Figure 81: Nonlinear permeability applied to the intima and media. (a) Displacement of the vessel wall in a cardiac cycle. (b) Pore flow pattern at the surface of vessel wall. (c) Pore pressure distribution at maximum reverse pore flow. (d) Pore fluid distribution at maximum reverse pore flow

CHAPTER VII

CONCLUSION

LDL is transported with blood flow in the intraluminal domain and with plasma flow in the arterial wall, and this transport is dominated by convection than diffusion. Further, hemodynamic WSS interacts with the artery wall to elicit a cascade of biological mechanism that leads to enhanced LDL ingress via the formation of leaky junctions that open gaps of sufficient size to allow LDL entry. Thus, there are intimate and complex relationships between hemodynamics, LDL transport and atherosclerosis. While much is understood about these processes, they are of sufficient complexity that comprehensive computational models that incorporate all relevant mechanisms are currently infeasible. In this study, we investigate a series of computational models of increasing complexity that, while remaining incomplete, elucidate interactions between biomechanical variables and atherogenic mechanisms using imaging data obtained in-vivo from the carotid arteries of three human subjects with varying degrees of atherosclerosis.

To compute the patterns of blood flow in the individual carotid arteries, fluid structure interaction (FSI) method is utilized based on the in-vivo arterial geometry constructed by black blood MRI (BBMRI) and on flow rate boundary conditions which are obtained from phase contrast images (PC). This approach highlights differences in the flow field between distensible wall and rigid wall assumptions. Wall shear stress (WSS), which has been recognized as a mechanical factor affecting endothelial function and dysfunction, is computed on the luminal surface from FSI calculation and further processed to extract time averaged WSS (TAWSS). This variable is hypothesized to be meaningful to the relationship between mechanical forces

and physiological responses of endothelium, because the characteristic time of cell response is much longer than the cardiac period. This hypothesis is plausible since the formation of leaky junctions is related to the rate increase of cell death (apoptosis) and proliferation (mitosis), each of which has a long characteristic time by comparison to the cardiac period. We incorporate the concept of "the fraction of leaky junction", established by Olgac et al. [65] and use this to represent the role of leaky junctions and their contribution to LDL entry into the intima. The fraction of leaky junction is obtained from TAWSS based on reported relationships and mass transport parameters, i.e., hydraulic conductivity, and permeability are determined with this value using pore theory.

Our research, which focuses on the idea that LDL concentration in the arterial wall is a marker for development and progression of atherosclerosis, supports the importance of geometrical features in individual subjects. In subject 1 with no dominant stenosis or significant curvature, flow patterns are relatively simple compared to other subjects, and the endothelial surfaces for the most part experience physiological wall shear stress; thus high LDL mass flux into the artery is limited to very small regions. However, in subject 2 which shows severe curvature in the carotid bulb, low wall shear stress is dominant around the bifurcation junction of the CCA and ICA/ECA due to complex flow pattern which arise due to the geometry. Hence, high mass flux regions are evident in these regions, including the carotid sinus. In subject 3, strong curvature in the CCA leads to asymmetrical flow patterns entering the region of interest, and this leads to helical flow patterns in the ICA and ECA partially due to the stenoses in both entrances; thus, large of areas experience low WSS and accordingly high mass flux is present in these same areas including the CCA. This subject demonstrated the greatest development of wall thickness among our subjects.

Maximum mass flux is demonstrated downstream of the stenosis, a region that experiences low WSS in general, and this is consistent with clinical observations of

plaque progression into downstream of the stenosis. The fact that the majority of LDL enters into the intima through leaky junctions is also confirmed by the similarity in distribution between the pattern of the volume flux via leaky junctions and mass flux. It reawakens the role of endothelium to mass transport of macromolecules in the circulation. At the same time, it suggests the possible approach to reduce the formation and progression of the plaque by inhibiting the incidence of apoptosis and mitosis. The quantitative change with wall thickness in the volume flux via normal junctions demonstrates the importance of consideration of wall thickness to obtain total filtration flow distribution and confirms the observation that normal junction is a dominant passageway for plasma fluid.

There are still several limitations in our research. To extract the faction of leaky junction in order to relate leaky junctions to LDL mass transport, only WSS is considered in the mathematical model. However, the endothelium experiences both WSS and cyclic mechanical strain (CS) in the circulation, and both have been shown to leads to the physiological response from endothelial cells (EC). This idea is supported biologically by the research done by Qiu et al. [69] in which they investigated the combined effects of WSS and CS on ECs. They defined the concept of SPA (stress phase angle), the phase angle between WSS and CS, and they applied different SPAs to cultures ECs and observed that the expression of vasodilators (PGI_2, NO) and a vasoconstrictor (ET-1) in ECs are influenced differently by different SPA values. The combined effect of these mechanical factors to ECs is also demonstrated by the response of actin stress fiber under different combinations of WSS and CS. Owatverot et al. [66] found a reinforcing mode, where cyclic stress and oscillatory WSS were additive, and also a counteracting mode, where both pairs of stimuli canceled out each other's effects. This suggests that both mechanical forces influence biological responses of ECs. Therefore, in future studies, biological experiments about the formation of leaky junction under various mechanical environments are essential and

the model for the fraction of leaky junction may need to be modified based on these experimental data to reflect the influence of both mechanical factors.

Another consideration is that the arterial structure responds dynamically to the pulsatility of blood flow by deformation of the intima and media. This dynamic structural deformation leads to change in Darcy′s permeability, which is a critical factor to plasma flow in the porous media. This structural change in an artery was demonstrated by Mahsa et al. [26]. In that study, it was found that the filtration flow was sensitive to arterial wall change with different luminal pressures and, accordingly, induced concentration changes in the arterial wall. In addition to this result, as discussed in Chapter 6, the filtration flow varies dramatically with the arterial wall response to pulsatility in a cardiac cycle. LDL concentration change as the result of filtration variations in a cardiac period is demonstrated more detailed in the research by Koshiba et al. [49]. In that study, using porohyperelasticity, higher LDL concentration near the wall side of the endothelium, which was not illustrated by the approach of Olagac et al. [65], is observed even without the multi-layered model for the arterial wall. However, they excluded the role of leaky junctions in LDL entry and simplified the role of the endothelium based on an idealized curved geometry. Therefore, it may be desirable to consider both the leaky junctions and poroelasticity simultaneously to gain LDL mass flux and a full description of LDL distribution in the arterial wall in future simulations aimed at further elucidation of the LDL role in the initiation and progression of atherotic plaque.

Finally, we emphasize that this investigation is essentially a computational study. It indeed utilized considerable biological findings from the literature in developing the computational models; but other than the in-vivo images of human subjects that provided geometry, wall thickness and velocity boundary conditions, we did not collect direct biological data, such as LDL concentrations in these subjects. Nonetheless, the work demonstrates the potential of computational models to explore connections

between biomechanics and vascular pathophysiology in human subjects.

APPENDIX A

CALCULATION OF THE CENTERLINE

The definition of centerline is more or less intuitive, thus many conceptual approaches have been suggested for the calculation of centerline based on $2D$ medical images or $3D$ geometry. Surface geometries of all subjects were imported to VMTK program developed by Lucas et al. [1]. This program has a function to compute the centerline based on a 3D surface model. The centerline calculation in VMTK starts from the polygonal surface representing the artery surface. A tetrahedrization of the vertices of these polygonal surfaces was performed by delaunay tessellation and delaunay tetrahedra were utilized to get voronoi spheres. From voronoi spheres, voronoi vertex connectivity was constructed by connecting two circumcenters of voronoi spheres. This polygonal connectivity is called an embedded voronoi diagram. In Fig. 82, the radius of each voronoi sphere is visualized by the color. The approaching red means the radius is small and the other way the radius is large. The left diagram represents the geometry and the right diagram shows the radius of voronoi diagram. Finally, the centerline of each carotid artery constructed from voronoi diagram implementation.

To apply the inner circumferential shrinkage ratio to reduce the inner wall of the artery the radius of the inner wall was calculated based on the distance from centerline points and each point on the inner wall. To get the shortest distance between the centerline of the artery and points, called the radius of each point, the closest point needs to be found from each centerline point through the comparison among every distance from one centerline point to all points on the inner wall. The shrinkage process with the centerline consideration prevents arterial distortion between the inner wall and outer wall because based on the centerline each radius of points on

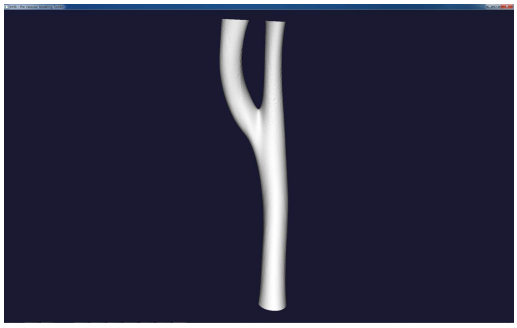

(a) Innerwall of Patient 1

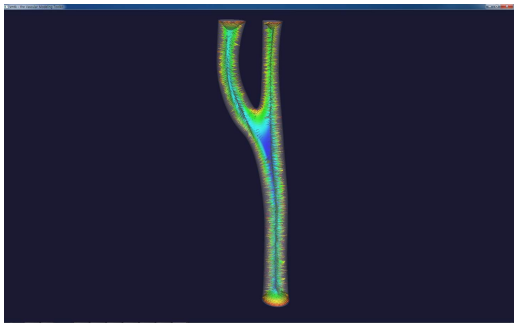

(b) Voronoi Diagram in Patient 1

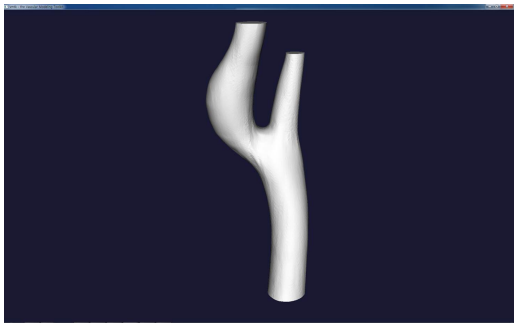

(c) Innerwall of Patient 2

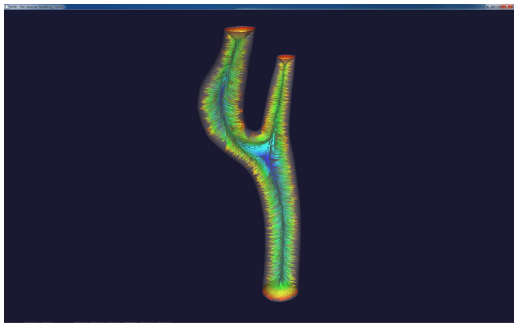

(d) Voronoi Diagram in Patient 2

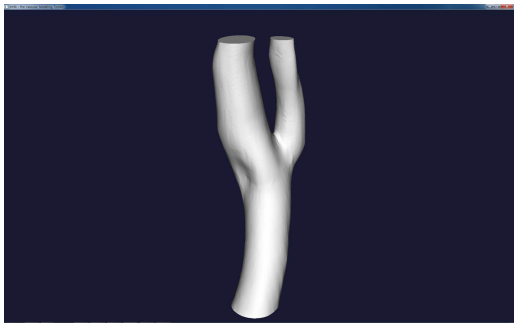

(e) Innerwall of Patient 3

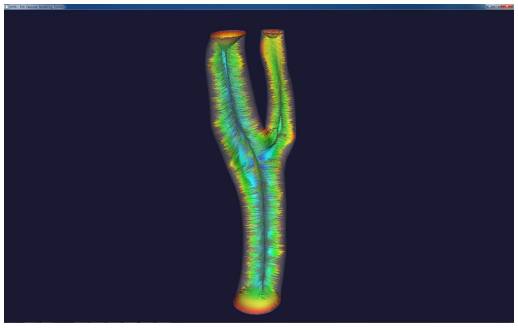

(f) Voronoi Diagram in Patient 3

Figure 82: Subject geometry and Voronoi diagram to calculate the centerline

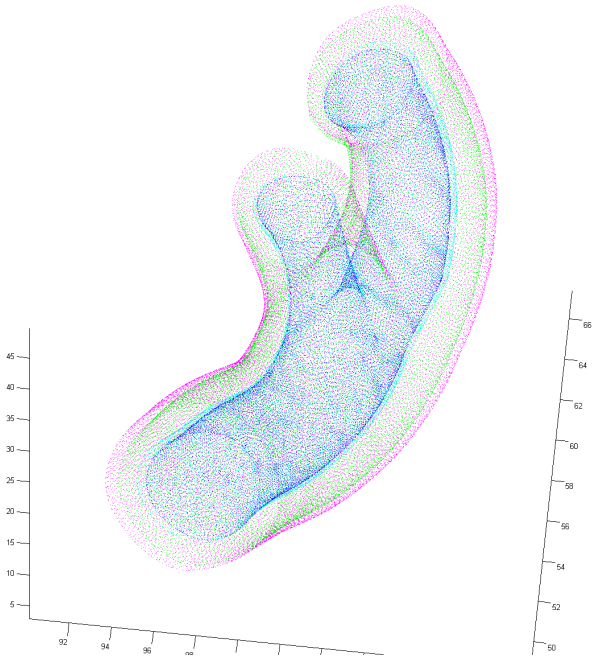

(a) No centerline correction between innerwall and outerwall

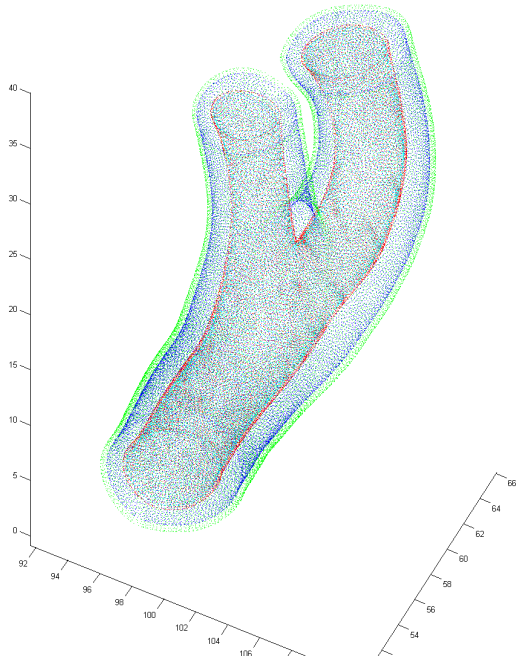

(b) With centerline correction between inner wall and outer wall

Figure 83: Comparison between with and without centerline correction to maintain the relative distance between inner wall and outer wall in subject 1

inner wall was reduced uniformly by inner circumferential ratio. This method was also applied to outer wall expansion after the outer circumferential ratio was decided by mass conservation. The distance to outer wall points from the centerline was calculated by finding the point which had a shortest distance. After then each radius was lengthened uniformly by outer circumferential ratio. This also helps to keep the relative distance from inner wall and outer wall, which represents wall thickness (Fig. 83).

REFERENCES

[1] "The vascular modeling tool kit," *http://www.vmtk.org*, Jan. 2011.

[2] Ai, L. and Vafai, K., "A coupling model for macromolecule transport in a stenosed arterial wall," *International Journal of Heat and Mass Transfer*, vol. 49, no. 9-10, pp. 1568–1591, 2006.

[3] Anayiotos, A. S., Jones, S. A., Giddens, D. P., Glagov, S., and Zarins, C. K., "Shear stress at a compliant model of the human carotid bifurcation," *Journal of Biomechanical Engineering*, vol. 116, no. 1, pp. 98–106, 1994.

[4] Ayyalasomayajula, A., Geest, J. P. V., and Simon, B. R., "Porohyperelastic finite element modeling of abdominal aortic aneurysms," *J Biomech Eng*, vol. 132, no. 10, p. 104502, 2010.

[5] Ballyk, P. D., Steinman, D. A., and Ethier, C. R., "Simulation of non-newtonian blood flow in an end-to-side anastomosis," *Biorheology*, vol. 31, no. 5, pp. 565–86, 1994.

[6] Bao X, Clark CB, F. J., "Temporal gradient in shear-induced signaling pathway: involvement of map kinase, c-fos, and connexin43," *American journal of physiology. Heart and circulatory physiology*, vol. 278, no. 5, pp. H1598–605, 2000.

[7] Bathe, M. and Kamm, R. D., "A fluid–structure interaction finite element analysis of pulsatile blood flow through a compliant stenotic artery," *J Biomech Eng*, vol. 121, no. 4, pp. 361–9, 1999.

[8] Berger, S. A. and Jou, L. D., "Flows in stenotic vessels," *Annual Review of Fluid Mechanics*, vol. 32, no. 1, pp. 347–382, 2000.

[9] Berliner, J. A. and Heinecke, J. W., "The role of oxidized lipoproteins in atherogenesis," *Free Radical Biology and Medicine*, vol. 20, no. 5, pp. 707–727, 1996.

[10] Berthier B, Bouzerar R, L. C., "Blood flow patterns in an anatomically realistic coronary vessel: influence of three different reconstruction methods.," *Journal of Biomechanics*, vol. 35, no. 10, pp. 1347–56, 2002.

[11] Boren, J., Olin, K., Lee, I., Chait, A., Wight, T. N., and Innerarity, T. L., "Identification of the principal proteoglycan-binding site in ldl. a single-point mutation in apo-b100 severely affects proteoglycan interaction without

affecting ldl receptor binding," *J Clin Invest*, vol. 101, no. 12, pp. 2658–64, 1998.

[12] Botnar R, Rappitsch G, S. M. L. D. P. K. B. P., "Hemodynamics in the carotid artery bifurcation: a comparison between numerical simulations and in vitro mri measurements," *Journal of biomechanics*, vol. 33, no. 2, pp. 137–44, 2000.

[13] Calara, F., Dimayuga, P., Niemann, A., Thyberg, J., Diczfalusy, U., Witztum, J. L., Palinski, W., Shah, P. K., Cercek, B., Nilsson, J., and Regnstrom, J., "An animal model to study local oxidation of ldl and its biological effects in the arterial wall," *Arterioscler Thromb Vasc Biol*, vol. 18, no. 6, pp. 884–93, 1998.

[14] Cancel, L. M., Fitting, A., and Tarbell, J. M., "In vitro study of ldl transport under pressurized (convective) conditions," *Am J Physiol Heart Circ Physiol*, vol. 293, no. 1, pp. H126–32, 2007.

[15] Cancel, L. M. and Tarbell, J. M., "The role of apoptosis in ldl transport through cultured endothelial cell monolayers," *Atherosclerosis*, vol. 208, no. 2, pp. 335–41, 2010.

[16] Cancel, L. M. and Tarbell, J. M., "The role of mitosis in ldl transport through cultured endothelial cell monolayers," *Am J Physiol Heart Circ Physiol*, vol. 300, no. 3, pp. H769–76, 2011.

[17] Causin, P., Gerbeau, J. F., and Nobile, F., "Added-mass effect in the design of partitioned algorithms for fluid-structure problems," *Computer Methods in Applied Mechanics and Engineering*, vol. 194, no. 42-44, pp. 4506–4527, 2005.

[18] Cebral, J. R., Yim, P. J., Lohner, R., Soto, O., and Choyke, P. L., "Blood flow modeling in carotid arteries with computational fluid dynamics and mr imaging," *Acad Radiol*, vol. 9, no. 11, pp. 1286–99, 2002.

[19] Chang, M. Y., Potter-Perigo, S., Tsoi, C., Chait, A., and Wight, T. N., "Oxidized low density lipoproteins regulate synthesis of monkey aortic smooth muscle cell proteoglycans that have enhanced native low density lipoprotein binding properties," *J Biol Chem*, vol. 275, no. 7, pp. 4766–73, 2000.

[20] Chappell, D. C., Varner, S. E., Nerem, R. M., Medford, R. M., and Alexander, R. W., "Oscillatory shear stress stimulates adhesion molecule expression in cultured human endothelium," *Circ Res*, vol. 82, no. 5, pp. 532–9, 1998.

[21] Chatzimavroudis GP, Oshinski JN, F. R. W. P. Y. A. P. R., "Evaluation of the precision of magnetic resonance phase velocity mapping for blood

flow measurements," *Journal of Cardiovascular Magnetic Resonance*, vol. 3, no. 1, pp. 11–19, 2001.

[22] Chien, S., "Molecular and mechanical bases of focal lipid accumulation in arterial wall," *Prog Biophys Mol Biol*, vol. 83, no. 2, pp. 131–51, 2003.

[23] Chien, S., "Mechanotransduction and endothelial cell homeostasis: the wisdom of the cell," *Am J Physiol Heart Circ Physiol*, vol. 292, no. 3, pp. H1209–1224, 2007.

[24] Conklin, B. S., Vito, R. P., and Chen, C., "Effect of low shear stress on permeability and occludin expression in porcine artery endothelial cells," *World J Surg*, vol. 31, no. 4, pp. 733–43, 2007.

[25] Dabagh, M., Jalali, P., and Tarbell, J. M., "The transport of ldl across the deformable arterial wall: the effect of endothelial cell turnover and intimal deformation under hypertension," *Am J Physiol Heart Circ Physiol*, vol. 297, no. 3, pp. H983–96, 2009.

[26] Dabagh, M., Jalali, P., and Tarbell, J. M., "The transport of ldl across the deformable arterial wall: the effect of endothelial cell turnover and intimal deformation under hypertension," *American Journal of Physiology - Heart and Circulatory Physiology*, vol. 297, no. 3, pp. H983–H996, 2009.

[27] Deng, X., Marois, Y., How, T., Merhi, Y., King, M., Guidoin, R., and Karino, T., "Luminal surface concentration of lipoprotein (ldl) and its effect on the wall uptake of cholesterol by canine carotid arteries," *J Vasc Surg*, vol. 21, no. 1, pp. 135–45, 1995.

[28] Donea, J., H. A. P. J.-P. and Rodriguez-Ferran, "Arbitrary lagrangian eulerian methods," *Encyclopedia of Computational Mechanics*, vol. 1, no. Wiley,New York, 2004.

[29] Ethier, C. R., "Computational modeling of mass transfer and links to atherosclerosis," *Ann Biomed Eng*, vol. 30, no. 4, pp. 461–71, 2002.

[30] F. P. Glor, Q. Long, A. D. H. A. D. A. B. A. S. A. M. T. P. R. V. and Xu, X. Y., "Reproducibility study of magnetic resonance image based computational fluid dynamics prediction of carotid bifurcation flow," *Annals of Biomedical Engineering*, vol. 31, pp. 142–151, 2003.

[31] Farhat, C., Lesoinne, M., and Le Tallec, P., "Load and motion transfer algorithms for fluid/structure interaction problems with non-matching discrete interfaces: Momentum and energy conservation, optimal discretization and application to aeroelasticity," *Computer Methods in Applied Mechanics and Engineering*, vol. 157, no. 1-2, pp. 95–114, 1998.

[32] Fornwalt, B. K. *Personal Communication*, 2009.

[33] Forster, C., Wall, W. A., and Ramm, E., "Artificial added mass instabilities in sequential staggered coupling of nonlinear structures and incompressible viscous flows," *Computer Methods in Applied Mechanics and Engineering*, vol. 196, no. 7, pp. 1278–1293, 2007.

[34] Gao, H., Long, Q., Graves, M., Gillard, J. H., and Li, Z. Y., "Carotid arterial plaque stress analysis using fluid-structure interactive simulation based on in-vivo magnetic resonance images of four patients," *J Biomech*, vol. 42, no. 10, pp. 1416–23, 2009.

[35] Goldbourt, U. and Neufeld, H. N., "Genetic aspects of arteriosclerosis," *Arterioscler Thromb Vasc Biol*, vol. 6, no. 4, pp. 357–377, 1986.

[36] He, X. and Ku, D. N., "Pulsatile flow in the human left coronary artery bifurcation: average conditions," *J Biomech Eng*, vol. 118, no. 1, pp. 74–82, 1996.

[37] Herrmann, R. A., Malinauskas, R. A., and Truskey, G. A., "Characterization of sites with elevated ldl permeability at intercostal, celiac, and iliac branches of the normal rabbit aorta," *Arterioscler Thromb*, vol. 14, no. 2, pp. 313–23, 1994.

[38] Holme, P. A., Orvim, U., Hamers, M. J. A. G., Solum, N. O., Brosstad, F. R., Barstad, R. M., and Sakariassen, K. S., "Shear-induced platelet activation and platelet microparticle formation at blood flow conditions as in arteries with a severe stenosis," *Arterioscler Thromb Vasc Biol*, vol. 17, no. 4, pp. 646–653, 1997.

[39] Holmes, M. H. and Mow, V. C., "The nonlinear characteristics of soft gels and hydrated connective tissues in ultrafiltration," *J Biomech*, vol. 23, no. 11, pp. 1145–56, 1990.

[40] Howard, A. B., Alexander, R. W., Nerem, R. M., Griendling, K. K., and Taylor, W. R., "Cyclic strain induces an oxidative stress in endothelial cells," *Am J Physiol*, vol. 272, no. 2 Pt 1, pp. C421–7, 1997.

[41] Huang, X., Yang, C., Yuan, C., Liu, F., Canton, G., Zheng, J., Woodard, P. K., Sicard, G. A., and Tang, D., "Patient-specific artery shrinkage and 3d zero-stress state in multi-component 3d fsi models for carotid atherosclerotic plaques based on in vivo mri data," *Mol Cell Biomech*, vol. 6, no. 2, pp. 121–34, 2009.

[42] Huang, Y., Rumschitzki, D., Chien, S., and Weinbaum, S., "A fiber matrix model for the filtration through fenestral pores in a compressible arterial intima," *Am J Physiol*, vol. 272, no. 4 Pt 2, pp. H2023–39, 1997.

[43] Hwang, J., Saha, A., Boo, Y. C., Sorescu, G. P., McNally, J. S., Holland, S. M., Dikalov, S., Giddens, D. P., Griendling, K. K.,

Harrison, D. G., and Jo, H., "Oscillatory shear stress stimulates endothelial production of o2- from p47phox-dependent nad(p)h oxidases, leading to monocyte adhesion," *J Biol Chem*, vol. 278, no. 47, pp. 47291–8, 2003.

[44] Johnston, B. M., Johnston, P. R., Corney, S., and Kilpatrick, D., "Non-newtonian blood flow in human right coronary arteries: steady state simulations," *J Biomech*, vol. 37, no. 5, pp. 709–20, 2004.

[45] Kao, C. H., Chen, J. K., Kuo, J. S., and Yang, V. C., "Visualization of the transport pathways of low density lipoproteins across the endothelial cells in the branched regions of rat arteries," *Atherosclerosis*, vol. 116, no. 1, pp. 27–41, 1995.

[46] Karino, T. A. and T, "Flow patterns and spatial distribution of atherosclerotic lesions in human coronary arteries," *Circulation Research*, vol. 66, pp. 1045–66, 1990.

[47] Kohler U, Marshall I, R. M. L. Q. X. X. H. P., "Mri measurement of wall shear stress vectors in bifurcation models and comparison with cfd predictions," *Journal of Magnetic Resonance Imaging*, vol. 14, no. 5, pp. 563–73, 2001.

[48] Kolandavel, M. K., Fruend, E. T., Ringgaard, S., and Walker, P. G., "The effects of time varying curvature on species transport in coronary arteries," *Ann Biomed Eng*, vol. 34, no. 12, pp. 1820–32, 2006.

[49] Koshiba, N., Ando, J., Chen, X., and Hisada, T., "Multiphysics simulation of blood flow and ldl transport in a porohyperelastic arterial wall model," *J Biomech Eng*, vol. 129, no. 3, pp. 374–85, 2007.

[50] Ku JP, Elkins CJ, T. C., "Comparison of cfd and mri flow and velocities in an in vitro large artery bypass graft model.," *Annals of Biomedical Engineering*, vol. 33, no. 3, pp. 257–69, 2005.

[51] Lee, K. W., Wood, N. B., and Xu, X. Y., "Ultrasound image-based computer model of a common carotid artery with a plaque," *Med Eng Phys*, vol. 26, no. 10, pp. 823–40, 2004.

[52] Leonard, B. P. and Mokhtari, S., "Beyond first-order upwinding: The ultra-sharp alternative for non-oscillatory steady-state simulation of convection," *International Journal for Numerical Methods in Engineering*, vol. 30, no. 4, pp. 729–766, 1990.

[53] Levesque, M. J. and Nerem, R. M., "The elongation and orientation of cultured endothelial cells in response to shear stress," *J Biomech Eng*, vol. 107, no. 4, pp. 341–7, 1985.

[54] Li, D. and Mehta, J. L., "Upregulation of endothelial receptor for oxidized ldl (lox-1) by oxidized ldl and implications in apoptosis of human coronary artery endothelial cells : Evidence from use of antisense lox-1 mrna and chemical inhibitors," *Arterioscler Thromb Vasc Biol*, vol. 20, no. 4, pp. 1116–1122, 2000.

[55] Lusis, A. J., "Atherosclerosis," *Nature*, vol. 407, pp. 233–241, 2000.

[56] Lutostansky, E. M., "The role of convective mass transfer in atherosclerosis," *Georgia Institute of Technology*, 1996.

[57] Malek, A. M., Alper, S. L., and Izumo, S., "Hemodynamic shear stress and its role in atherosclerosis," *JAMA*, vol. 282, no. 21, pp. 2035–2042, 1999.

[58] Meyer, G., Merval, R., and Tedgui, A., "Effects of pressure-induced stretch and convection on low-density lipoprotein and albumin uptake in the rabbit aortic wall," *Circ Res*, vol. 79, no. 3, pp. 532–40, 1996.

[59] Michel, J.-B., "Anoikis in the cardiovascular system: Known and unknown extracellular mediators," *Arterioscler Thromb Vasc Biol*, vol. 23, no. 12, pp. 2146–2154, 2003.

[60] Milner, J. S., Moore, J. A., Rutt, B. K., and Steinman, D. A., "Hemodynamics of human carotid artery bifurcations: computational studies with models reconstructed from magnetic resonance imaging of normal subjects," *J Vasc Surg*, vol. 28, no. 1, pp. 143–56, 1998.

[61] Nagel, T., Resnick, N., Dewey, C. F., J., and Gimbrone, M. A., J., "Vascular endothelial cells respond to spatial gradients in fluid shear stress by enhanced activation of transcription factors," *Arterioscler Thromb Vasc Biol*, vol. 19, no. 8, pp. 1825–34, 1999.

[62] Nielsen, L. B., "Transfer of low density lipoprotein into the arterial wall and risk of atherosclerosis," *Atherosclerosis*, vol. 123, no. 1-2, pp. 1–15, 1996.

[63] Nilsson, B. n. and Heyden, A., "A fast algorithm for level set-like active contours," *Pattern Recognition Letters*, vol. 24, no. 9-10, pp. 1331–1337, 2003.

[64] Ogden, R. W., "Large deformation isotropic elasticity - on the correlation of theory and experiment for incompressible rubberlike solids," *Proceedings of the Royal Society of London. A. Mathematical and Physical Sciences*, vol. 326, no. 1567, pp. 565–584, 1972.

[65] Olgac, U., Kurtcuoglu, V., and Poulikakos, D., "Computational modeling of coupled blood-wall mass transport of ldl: effects of local wall shear stress," *Am J Physiol Heart Circ Physiol*, vol. 294, no. 2, pp. H909–919, 2008.

[66] Owatverot, T. B., Oswald, S. J., Chen, Y., Wille, J. J., and Yin, F. C., "Effect of combined cyclic stretch and fluid shear stress on endothelial cell morphological responses," *J Biomech Eng*, vol. 127, no. 3, pp. 374–82, 2005.

[67] Perktold, K. and Rappitsch, G., "Computer simulation of local blood flow and vessel mechanics in a compliant carotid artery bifurcation model," *Journal of Biomechanics*, vol. 28, no. 7, pp. 845–856, 1995.

[68] Prosi, M., Zunino, P., Perktold, K., and Quarteroni, A., "Mathematical and numerical models for transfer of low-density lipoproteins through the arterial walls: a new methodology for the model set up with applications to the study of disturbed lumenal flow," *Journal of Biomechanics*, vol. 38, no. 4, pp. 903–917, 2005.

[69] Qiu, Y. and Tarbell, J. M., "Interaction between wall shear stress and circumferential strain affects endothelial cell biochemical production," *Journal of Vascular Research*, vol. 37, no. 3, pp. 147–157, 2000.

[70] Ramnarine, K. V., Hartshorne, T., Sensier, Y., Naylor, M., Walker, J., Naylor, A. R., Panerai, R. B., and Evans, D. H., "Tissue doppler imaging of carotid plaque wall motion: a pilot study," *Cardiovasc Ultrasound*, vol. 1, p. 17, 2003.

[71] Reape, T. J. and Groot, P. H. E., "Chemokines and atherosclerosis," *Atherosclerosis*, vol. 147, no. 2, pp. 213–225, 1999.

[72] Rosamond, W., Flegal, K., Furie, K., Go, A., Greenlund, K., Haase, N., Hailpern, S. M., Ho, M., Howard, V., Kissela, B., Kittner, S., Lloyd-Jones, D., McDermott, M., Meigs, J., Moy, C., Nichol, G., O'Donnell, C., Roger, V., Sorlie, P., Steinberger, J., Thom, T., Wilson, M., Hong, Y., for the American Heart Association Statistics Committee, and Stroke Statistics, S., "Heart disease and stroke statistics 2008 update: A report from the american heart association statistics committee and stroke statistics subcommittee," *Circulation*, vol. 117, no. 4, pp. e25–146, 2008.

[73] Ross, R., "Atherosclerosis an inflammatory disease," *The New England Journal of Medicine*, vol. 340, no. 2, pp. 115–126, 1999.

[74] Sang-Wook, L., Luca, A., and David, A. S., "Correlations among indicators of disturbed flow at the normal carotid bifurcation," *Journal of Biomechanical Engineering*, vol. 131, no. 6, p. 061013, 2009.

[75] SCAI, "Mpcci (mesh based parallel code coupling interface) manual 3.0.6," *www.scai.fraunhofer.de/mpcci*.

[76] Schwenke, D. and Carew, T., "Initiation of atherosclerotic lesions in cholesterol-fed rabbits. i. focal increases in arterial ldl concentration precede development of fatty streak lesions," *Arterioscler Thromb Vasc Biol*, vol. 9, no. 6, pp. 895–907, 1989.

[77] Segrest, J. P., Jones, M. K., De Loof, H., and Dashti, N., "Structure of apolipoprotein b-100 in low density lipoproteins," *Journal of Lipid Research*, vol. 42, no. 9, pp. 1346–1367, 2001.

[78] Simon, B. R., Kaufmann, M. V., McAfee, M. A., Baldwin, A. L., and Wilson, L. M., "Identification and determination of material properties for porohyperelastic analysis of large arteries," *J Biomech Eng*, vol. 120, no. 2, pp. 188–94, 1998.

[79] Smedby, O., "Do plaques grow upstream or downstream?: An angiographic study in the femoral artery," *Arterioscler Thromb Vasc Biol*, vol. 17, no. 5, pp. 912–918, 1997.

[80] Snelting-Havinga, I., Mommaas, M., Van Hinsbergh, V. W., Daha, M. R., Daems, W. T., and Vermeer, B. J., "Immunoelectron microscopic visualization of the transcytosis of low density lipoproteins in perfused rat arteries," *Eur J Cell Biol*, vol. 48, no. 1, pp. 27–36, 1989.

[81] Stangeby, D. K. and Ethier, C. R., "Computational analysis of coupled blood-wall arterial ldl transport," *J Biomech Eng*, vol. 124, no. 1, pp. 1–8, 2002.

[82] Stary, H. C., Chandler, A. B., Glagov, S., Guyton, J. R., Insull, W., J., Rosenfeld, M. E., Schaffer, S. A., Schwartz, C. J., Wagner, W. D., and Wissler, R. W., "A definition of initial, fatty streak, and intermediate lesions of atherosclerosis. a report from the committee on vascular lesions of the council on arteriosclerosis, american heart association," *Circulation*, vol. 89, no. 5, pp. 2462–78, 1994.

[83] Stein, P. D., Hamid, M. S., Shivkumar, K., Davis, T. P., Khaja, F., and Henry, J. W., "Effects of cyclic flexion of coronary arteries on progression of atherosclerosis," *Am J Cardiol*, vol. 73, no. 7, pp. 431–7, 1994.

[84] Steinman, D. A., "Image-based computational fluid dynamics: A new paradigm for monitoring hemodynamics and atherosclerosis," *Current Drug Targets - Cardiovascular and Haematological Disorders*, vol. 4, no. 2, pp. 183–97, 2004.

[85] Steinman DA, Thomas JB, L. H. M. J. R. B. S. J., "Reconstruction of carotid bifurcation hemodynamics and wall thickness using computational fluid dynamics and mri," *Magnetic Resonance in Medicine*, vol. 47, no. 1, pp. 149–159, 2002.

[86] Sun, N., Wood, N. B., Hughes, A. D., Thom, S. A., and Xu, X. Y., "Fluid-wall modelling of mass transfer in an axisymmetric stenosis: effects of shear-dependent transport properties," *Ann Biomed Eng*, vol. 34, no. 7, pp. 1119–28, 2006.

[87] Sun, N., Wood, N. B., Hughes, A. D., Thom, S. A. M., and Yun Xu, X., "Effects of transmural pressure and wall shear stress on ldl accumulation in the arterial wall: a numerical study using a multilayered model," *Am J Physiol Heart Circ Physiol*, vol. 292, no. 6, pp. H3148–3157, 2007.

[88] Suo Jin, Yan Yang, J. O. A. T. J. G. and Giddens, D., "Flow patterns and wall shear stress distributions at atherosclerotic-prone sites in a human left coronary artery-an exploration using combined methods of ct and computational fluid dynamics," *Proceedings of the 26th Annual International Conference of the IEEE EMBS*, vol. 2004, 2004.

[89] Tada, S. and Tarbell, J. M., "A computational study of flow in a compliant carotid bifurcation-stress phase angle correlation with shear stress," *Ann Biomed Eng*, vol. 33, no. 9, pp. 1202–12, 2005.

[90] Tang, D., Yang, C., Kobayashi, S., and Ku, D. N., "Steady flow and wall compression in stenotic arteries: a three-dimensional thick-wall model with fluid-wall interactions," *J Biomech Eng*, vol. 123, no. 6, pp. 548–57, 2001.

[91] Tarbell, J. M., "Mass transport in arteries and the localization of atherosclerosis," *Annu Rev Biomed Eng*, vol. 5, pp. 79–118, 2003.

[92] Tedgui, A. and Lever, M. J., "Filtration through damaged and undamaged rabbit thoracic aorta," *American Journal of Physiology - Heart and Circulatory Physiology*, vol. 247, no. 5, pp. H784–H791, 1984.

[93] Tropea, B. I., Schwarzacher, S. P., Chang, A., Asvar, C., Huie, P., Sibley, R. K., and Zarins, C. K., "Reduction of aortic wall motion inhibits hypertension-mediated experimental atherosclerosis," *Arterioscler Thromb Vasc Biol*, vol. 20, no. 9, pp. 2127–2133, 2000.

[94] Valencia, A. and Villanueva, M., "Unsteady flow and mass transfer in models of stenotic arteries considering fluid-structure interaction," *International Communications in Heat and Mass Transfer*, vol. 33, no. 8, pp. 966–975, 2006.

[95] Wada, S. and Karino, T., "Theoretical study on flow-dependent concentration polarization of low density lipoproteins at the luminal surface of a straight artery," *Biorheology*, vol. 36, no. 3, pp. 207–223, 1999.

[96] Wada, S. and Karino, T., "Theoretical prediction of low-density lipoproteins concentration at the luminal surface of an artery with a multiple bend," *Ann Biomed Eng*, vol. 30, no. 6, pp. 778–91, 2002.

[97] Wang, B.-W., Chang, H., Lin, S., Kuan, P., and Shyu, K.-G., "Induction of matrix metalloproteinases-14 and -2 by cyclical mechanical stretch is mediated by tumor necrosis factor-alpha in cultured human umbilical vein endothelial cells," *Cardiovasc Res*, vol. 59, no. 2, pp. 460–469, 2003.

[98] Wasserman, B. A., Wityk, R. J., Trout, Hugh H., I., and Virmani, R., "Low-grade carotid stenosis: Looking beyond the lumen with mri," *Stroke*, vol. 36, no. 11, pp. 2504–2513, 2005.

[99] Weinbaum, S., Tzeghai, G., Ganatos, P., Pfeffer, R., and Chien, S., "Effect of cell turnover and leaky junctions on arterial macromolecular transport," *Am J Physiol*, vol. 248, no. 6 Pt 2, pp. H945–60, 1985.

[100] Wellnhofer E, Goubergrits L, K. U. A. K., "In-vivo coronary flow profiling based on biplane angiograms: influence of geometric simplifications on the three-dimensional reconstruction and wall shear stress calculation," *Biomedical engineering online*, vol. 5, no. 39, 2006.

[101] Whale, M. D., Grodzinsky, A. J., and Johnson, M., "The effect of aging and pressure on the specific hydraulic conductivity of the aortic wall," *Biorheology*, vol. 33, no. 1, pp. 17–44, 1996.

[102] Wu, C. H., Chi, J. C., Jerng, J. S., Lin, S. J., Jan, K. M., Wang, D. L., and Chien, S., "Transendothelial macromolecular transport in the aorta of spontaneously hypertensive rats," *Hypertension*, vol. 16, no. 2, pp. 154–61, 1990.

[103] Wung, B. S., Cheng, J. J., Hsieh, H. J., Shyy, Y. J., and Wang, D. L., "Cyclic strain-induced monocyte chemotactic protein-1 gene expression in endothelial cells involves reactive oxygen species activation of activator protein 1," *Circ Res*, vol. 81, no. 1, pp. 1–7, 1997.

[104] Zarins, C., Giddens, D., Bharadvaj, B., Sottiurai, V., Mabon, R., and Glagov, S., "Carotid bifurcation atherosclerosis. quantitative correlation of plaque localization with flow velocity profiles and wall shear stress," *Circ Res*, vol. 53, no. 4, pp. 502–514, 1983.

[105] Zhang, Q. and Hisada, T., "Analysis of fluid-structure interaction problems with structural buckling and large domain changes by ale finite element method," *Computer Methods in Applied Mechanics and Engineering*, vol. 190, no. 48, pp. 6341–6357, 2001.

[106] Zhao, S. Z., Ariff, B., Long, Q., Hughes, A. D., Thom, S. A., Stanton, A. V., and Xu, X. Y., "Inter-individual variations in wall shear stress and mechanical stress distributions at the carotid artery bifurcation of healthy humans," *Journal of Biomechanics*, vol. 35, no. 10, pp. 1367–1377, 2002.

[107] Zhao, S. Z., Xu, X. Y., Collins, M. W., Stanton, A. V., Hughes, A. D., and Thom, S. A., "Flow in carotid bifurcations: effect of the superior thyroid artery," *Med Eng Phys*, vol. 21, no. 4, pp. 207–14, 1999.

[108] Zhao, S. Z., Xu, X. Y., Hughes, A. D., Thom, S. A., Stanton, A. V., Ariff, B., and Long, Q., "Blood flow and vessel mechanics in a physiologically realistic model of a human carotid arterial bifurcation," *Journal of Biomechanics*, vol. 33, no. 8, pp. 975–984, 2000.